MOTILITY, MULTICELLULARITY AND MULTICILIATES

by

MATTHEW CLOWE
SUPERVISED BY THOMAS MONTENEGRO-JOHNSON, FABIAN SPILL AND DAVID SMITH

A thesis submitted to
The University of Birmingham
for the degree of
DOCTOR OF PHILOSOPHY

School of Mathematics
College of Engineering and Physical Sciences
The University of Birmingham
October 2023

UNIVERSITY OF
BIRMINGHAM

University of Birmingham Research Archive

e-theses repository

This unpublished thesis/dissertation is copyright of the author and/or third parties. The intellectual property rights of the author or third parties in respect of this work are as defined by The Copyright Designs and Patents Act 1988 or as modified by any successor legislation.

Any use made of information contained in this thesis/dissertation must be in accordance with that legislation and must be properly acknowledged. Further distribution or reproduction in any format is prohibited without the permission of the copyright holder.

Abstract

Motility plays a vital role in life for many cells and organisms. However, motility at the microscale is quite different to at the macroscale. Therefore, microscopic cells and organisms have developed multiple methods to navigate this problem, often using long thin appendages known as flagella. These organisms are known as microswimmers, some of which will be the focus of this thesis. Specifically, we study microswimmers that are either multicellular or multiciliate, since little work for these have been done previously using accurate models with full flagella.

We first study this by considering the pumping of cilia over a plane using prescribed beat kinematics. This will allow us to study optimal metachronal waves in terms of the flux they produce. We then go on to study the fluid structure interaction between cilia using a bead and spring type model. Using this we will look to study how the cilia coordinate with each other and form into different types of beat patterns such as metachronal waves.

Following this, we will move on to study the swimming behaviour of complex swimmers using prescribed beat kinematics. We mostly focus these results on the Volvocine green algae. Some of the swimmers that we study have complex shapes. To model the body of these swimmers we will make use of level sets and use a Nearest Neighbour Regularised Stokeslet method to study their swimming behaviour. This model will then be used as part of an app that we will build that will be able to simply create swimmer models. We will then look to combine our previous work and study the fluid structure interaction using a bead and spring model for full swimmers. This will help us to understand how flagella interact and coordinate with each other over complex shaped bodies.

ACKNOWLEDGEMENTS

I would like to thank my supervisors Prof. Tom Montenegro-Johnson, Dr Fabian Spill and Prof. David Smith for their great supervision and guidance throughout this PhD. In particular, I am very grateful to Prof. Tom Montenegro-Johnson, for his great insight to help guide me in my work as well as his his endless support to help get me through this PhD. I would also like to thank Dr Panayiota Katsamba who provided me with a lot of helpful guidance during the first year of my PhD. I would also like to thank the EPSRC and School of Mathematics at the University of Birmingham for the funding and scholarship, without which I would not have been able to do the PhD. I would also like to thank my friends and family who have provided me with constant support and encouragement. In particular I would like to thank my friend (now Dr) Amelia Hall who has been an endless supply of support and encouragement throughout my entire PhD.

CONTENTS

1 Introduction **1**

1.1 Microswimmers 1

1.1.1 Eukaryotic and Prokaryotic Swimmers 3

1.1.2 Swimming techniques 6

1.1.3 Metachronal Waves and Multiciliate Swimmers 9

1.1.4 Multicellular Swimmers 11

1.2 Physics of Microscale Swimming 13

1.3 Mathematical Studies of Microswimmers 16

1.3.1 Taylor's Swimming Sheet 16

1.3.2 Slender Body Theory and Resistive Force Theory 18

1.3.3 Images for Complex Domains 20

1.3.4 Boundary Element Methods and Regularised Stokeslets 21

1.3.5 Squirmers 24

1.3.6 Bead and Spring Models 25

1.3.7 Multiciliate and Multicellular Models 27

2 Mathematical Methods for Modelling Microswimmers **29**

2.1 Low Reynolds Number Flows 29

2.1.1 Regularised Stokeslets 33

2.2 Nearest Neighbour Method 38

2.3 Level Sets for Swimmer Geometries 41

2.4 Flagella Waveforms 46

2.5 Flux Calculation 49

3 Studying the Metachronal Wave **52**

3.1 Models With a Prescribed Cilia Beat 52

3.1.1 Flux from one beating cilium 53

3.1.2 Flux over time vs Phase Difference For Multiple Cilia Using The Full Cilium Model 55

3.1.3 Distance Between Cilia vs Metachronal Flux 56

3.1.4 Angle of Flagella vs metachronal flux 58

3.1.5 Modelling the Cilium As a Single Regularised Force 60

3.2 Synchronisation Model - Bead and Spring Model 68

3.2.1 Bead and Spring Model For Two Cilia 70

3.2.2 Bead and Spring Model For Three Cilia 77

3.2.3 Bead and Spring Model For Twenty Cilia 81

3.2.4 Bead and Spring Model Around a Circle 87

3.3 Summary 97

4 The Algal Colony Suite **99**

4.1 Motile Green Algae 99

4.2 The Algal Colony Suite 101

4.3 Convergence 104

4.4 Volvocine Green Algae Results 108

4.4.1 Chlamydomonas 108

4.4.2 Tetrabaena 110

4.4.3 Gonium 114

4.4.4 Pandorina 116

4.4.5 Eudorina 117

4.4.6 Pleodorina 118

4.4.7 Volvocine Discussion 121

4.5 Didinium nasutum 122
4.5.1 Convergence 124
4.5.2 Swimming Behaviour 126
4.6 Summary 131

5 Bead and Spring Models of Microswimmers 132
5.1 Model Overview 132
5.2 Bead and Spring Model of Chlamydomonas 133
5.3 Bead and Spring Model For a Multiciliate Swimmer 138
5.4 Bead and Spring Models For Complex Shaped Microswimmers 142
5.5 Summary 143

6 Conclusions and Outlook 145
6.1 Summary 145
6.2 Further Work 150

LIST OF FIGURES

1.1 This Figure shows four examples of microswimmers. Panel A shows a *Chlamydomonas reihardtii*, a single celled alga that swims by moving its two flagella in a breaststroke pattern. Panel B shows an *E. coli*, a bacterium cell with multiple rotating helical flagella that bundle together to give the cell a run and tumble motion. Panel C shows two sperm cells that swim by propagating a travelling bending wave along its flagellum. Panel D shows a *Paramecium* cell which has multiple cilia over its surface, beating in a metachronal wave to help it swim. Panels A, B and D are take from Stocker and Durham (2009), and panel C is taken from Gillies et al. (2009) 2

1.2 Diagram showing the 9+2 arrangement of microtubules in the axoneme for Eukaryotic flagella taken from Montenegro-Johnson (2013) 4

1.3 Figure showing examples of different flagella beats. Panel (a) shows a model example of a rotating helical flagella, as seen in bacteria such as *E. coli*. Panel (b) shows the beating of a sperm flagellum. In Panel (c) we show a model example of a beating cilia in a sweeping motion. This beating pattern is used for algal swimmers such as *Chlamydomonas*. In Panel (d) we show a large group of cilia beating with a metachronal wave along the cilia as part of a ciliary carpet. Metachronal waves are seen in swimming for swimmers such as Paramecium. Panels (a)-(c) uses a greyscale colouring to represent the time step of the beat, fading from black as the time, t increases. 7

1.4 Figure displaying the effective stroke in Panel (a) and recovery stroke in Panel (b) for the Effective-Recovery beat that is utilised by the beating of a cilia or Volvocine flagellum. 8

1.5 Figure displaying a metachronal wave in both symplectic (travelling wave moves in the same direction as the effective stroke) and antiplectic (travelling wave moves in the opposite direction to the effective stroke) directions. The metachronal wave is produced by sequential beating of cilia producing a travelling wave along the cilia. We show the direction of the metachronal waves with arrows above the cilia. 10

1.6 Figure showing examples of two types of colony. The left image shows bacterial colonies formed by the swarming of bacteria taken from Velicer and Yu (2003). The right image shows the algal colony *Volvox*, taken from Pedley et al. (2016). 12

1.7 A recreation of Figure 1 from Arakaki et al. (2013), showing the Volvocine green algae from smallest to largest using the model swimmers created in our app the Algal Colony Suite which will be introduced in Chapter 4. . . 12

1.8 Figure showing a schematic demonstrating the effect of drag anisotropy. This figure is taken from Figure 3 in Montenegro-Johnson et al. (2012). . . 14

1.9 Diagram showing the forces from typical microswimmers (in black) and flow field (in red). The left shows a typical puller drawing fluid in along its swimming direction and pushing it out from the sides. The right shows a typical pusher which pushes fluid away along its swimming direction and draws it in to the sides. 15

2.1 Figure displaying the level sets from adding 4 Gaussians to model *Tetrabaena*. Panels (a) and (b) show the level set of Gaussians for a low amount of mucilage. Panel (a) shows this for a 2D Gaussian where as Panel (b) gives the level set surface from a 3D Gaussian. Panels (c) and (d) give the 2D and 3D (respectively) level sets for the model of *Tetrabaena* with a high level of Mucilage. For the 2D cases in Panels (a) and (c) we have the colour map showing the value of the function and the line showing the desired level set. 43

2.2 Figure showing the flagella waveform model for *Chlamydomonas* taken from Gallagher and Smith (2018). 47

2.3 Figure showing the wave fitting model for the data. Panel (a) shows the tangent angle given from the data while Panel (b) shows the tangent angle of the model waveform. In Panel (c) we display the waveform for the fitted model. 48

3.1 Figure showing variables we consider in studying the flux from a metachronal wave. d is the distance between one cilia and the next and is measured in flagella lengths. α is the angle (twisted at the base) of cilia. This angle is the angle between the line that connects the two cilia (represented by the bottom horizontal line) and plane that the flagella beat in and is measured in radians. We calculate the flux in the x direction (to the right in this figure). 53

3.2 Figure showing the flux produced over time by one beating cilium over one beat calculated using the time varying flux equation in (2.43). Panels (a) and (b) represent the cilium as a regularised force with a circular trajectory with radius $r = 0.5$ in Panel (a) and a more accurate trajectory in Panel (b). Panel (c) shows the flux from a full cilium of length 1. 54

3.3 Figure showing the flux over time and Phase difference between the cilia of length 1 as a surface plot. These results were found using the full cilium model. We take the flux measurements with $d = 1.1$ and $\alpha = 0$. Panel (a) shows the data for 2 cilia and Panel (b) shows the data for 3 cilia. This data is normalised over the number of cilia. 55

3.4 Figure showing the total flux after one beat over the phase difference between cilia of length 1 for increasing distance d between the cilia. We keep $\alpha = 0$. We show this for 2 cilia in Panel (a) and 3 cilia in Panel (b). The flux is normalised over the total flux from 1 cilia and the number of cilia. In this figure and throughout the thesis, negative phase difference represents an antiplectic metachronal wave and positive phase difference represents a symplectic metachronal wave. 57

3.5 Figure showing the total flux after one beat over the phase difference between cilia of length 1 for varying angle α between the cilia. We keep $d = 1.1$. The top row shows the results for 2 cilia and the bottom row shows the results for 3 cilia. Panels (a) and (d) show the flux in the x direction, Panels (b) and (e) show the flux in the y direction and Panels (c) and (f) show the flux in the direction of the cilia. The flux is normalised over the total flux from 1 cilia and the number of cilia. The metachronal wave of the cilia is in the x direction. 59

3.6 Figure showing the total flux after one beat over the phase difference between cilia for increasing distance d between the cilia. We keep $\alpha = 0$ and the cilia are modelled using the circular regularised force model with a radius of $r = 0.5$ and normalised over the total flux from one cilium using this model. We show this for 2 cilia in Panel (a), 3 cilia in Panel (b), 100 cilia in Panel (c) and a lattice of ten by ten cilia in Panel (d). 61

3.7 Figure showing the total flux after one beat over the phase difference between cilia for increasing distance d between the cilia. We keep $\alpha = 0$ and the cilia are modelled using the Accurate regularised force model and normalised over the total flux from one cilium using this model. We show this for 2 cilia in Panel (a), 3 cilia in Panel (b). 63

3.8 Figure showing the total flux after one beat over the Phase Difference between cilia for varying angle α between the cilia. We keep $d = 1.1$ and the cilia are modelled using the circular regularised force model with radius $r = 0.5$ and normalised over the total flux from one cilium using this model. We show the flux in the $x-$direction (Panels (a) and (d)), $y-$direction (Panels (b) and (e)) and the direction of the cilia (Panels (c) and (f)) with the results for two cilia in the top row and the results for three cilia on the bottom row. 64

3.9 Figure showing the total flux after one beat over the Phase Difference between cilia for varying angle α between the cilia. We keep $d = 1.1$ and the cilia are modelled using the accurate regularised force model and normalised over the total flux from one cilium using this model. We show the flux in the $x-$direction (Panels (a) and (d)), $y-$direction (Panels (b) and (e)) and the direction of the cilia (Panels (c) and (f)) with the results for two cilia in the top row and the results for three cilia on the bottom row. 65

3.10 Figure showing the total flux after one beat over the Phase Difference between 100 cilia for varying angle α between the cilia. We keep $d = 1.1$ and the cilia are modelled using the circular regularised force model with a radius of $r = 0.5$ and normalised over the total flux from one cilium using this model. We show the flux in the $x-$direction (Panels (a) and (d)), $y-$direction (Panels (b) and (e)) and the direction of the cilia (Panels (c) and (f)) with the results for the cilia in a line in the top row and the results for the cilia arranged in a 10 by 10 lattice on the bottom row. 67

3.11 Schematic showing the setup and variables for our bead and spring model. Panel (a) shows a side on view while Panel (b) shows a topdown view. In Panel (a), we show the phases of the two beads θ_i given by the angle of the spring to a vertical line. The dashed lines represent the circular trajectories of the beads and we also show the forces acting on the beads $\boldsymbol{F}^{\boldsymbol{i}}_{\boldsymbol{Spr}}$ and $\boldsymbol{F}^{\boldsymbol{i}}_{\boldsymbol{Dri}}$. In Panel (b) we show the distance between the origins of the springs attached to each bead as d as well as the orientation angle α. α represents the angle of the trajectory of the bead from the x direction. . 70

3.12 Phase difference over time between two neighbouring beads as part of the bead and spring model for both Stokeslets (Panel (a)) and Blakelets (Panel (b)). The beads are positioned a distance of $d = 1.3$ apart from each other and they have a natural spring length of $l = 0.5$ This is done for different initial phase difference as well as $\alpha = 0$ 71

3.13 Phase difference over time between two neighbouring beads as part of the bead and spring model for Blakelets for different angles of beating α and starting at a Phase difference of 0. The bead and spring system has the spring origins a distance of $d = 1.3$ and natural spring length of $l = 0.5$. . 72

3.14 Phase difference over time between two neighbouring beads as part of the bead and spring model for both Stokeslets (Panel (a)) and Blakelets (Panel (b)). This is done for different initial phase difference as well as $\alpha = \pi/2$. Again we have a spring length of $l = 0.5$ and distance between spring origins of the system of $d = 1.3$ 73

3.15 End Phase Difference of 2 beads in a bead and spring model over the angle α. Again we have a spring length of $l = 0.5$ and distance between spring origins of the system of $d = 1.3$ 74

3.16 End Phase Difference of 2 beads in a bead and spring model over the distance between the origin of the springs. We have a spring length of $l = 0.5$ with angle $\alpha = 0$. 75

3.17 Phase Difference over time between two neighbouring beads as part of the bead and spring model for Blakelets. This is done for different initial phase differences as well as $\alpha = 0$ and a spring length of $l = 0.5$. In these results we test larger distances between beads with Panel (a) showing $d = 20$ and Panel (b) showing $d = 100$. 75

3.18 Phase difference over time between three neighbouring beads as part of the bead and spring model for both Stokeslets and Blakelets. This is done for different initial phase difference as well as both $\alpha = 0$ and $\alpha = \pi/2$. The distance between the spring origins of neighbouring beads are $d = 1.3$ and we have natural spring lengths of $l = 0.5$ The solid lines represent the Phase difference of bead 1 - bead 2, while the dashed line represents the Phase difference of bead 2 - bead 3 78

3.19 End Phase Difference of 3 beads in a bead and spring model over the angle α for both Stokeslets and Blakelets. The solid line represents the Phase difference of bead 1 - bead 2, while the dotted line represents the Phase difference of bead 2 - bead 3. The spring origins between neighbouring beads have a distance between them of $d = 1.3$ and the springs have natural length of $l = 0.5$ 80

3.20 Phase difference over time between twenty neighbouring beads as part of the bead and spring model for beads near a wall modelled by Blakelets. The graphs are coloured using a parula colour map starting at the first pair of beads with the results in blue moving along to the final pair of beads with the results in yellow. This is done for different initial phase differences as well as different orientation angles of $\alpha = 0$, $\alpha = \pi/4$ and $\alpha = \pi/2$ as well as $d = 1.3$. 82

3.21 Figure showing the wave form of the bead and spring model for 20 beads. The colours of the plot represent the time which is increasing as we move through the parula colour map from blue to yellow. This is done in the x-z plane for three orientations of $\alpha = 0$, and the x-y, x-z and y-z planes for $\alpha = \pi/4$ and $\alpha = \pi/2$. 85

3.22 End Phase Difference over twenty beads in a bead spring model as we vary the orientation angle α. The graphs are coloured using a parula colour map starting at the first pair of beads with the results in blue to the final pair of beads with the results in yellow. 86

3.23 Schematic showing the setup and variables for our bead and spring model around a circle with the beads beating out from the centre of the circle. Panel (a) shows a side on view while Panel (b) shows a top down view. In Panel (a), we show the phase difference of the beads denoted by θ_i, as well as the Forces acting on the beads as $\boldsymbol{F}^{\boldsymbol{i}}_{\boldsymbol{Dri}}$ and $\boldsymbol{F}^{\boldsymbol{i}}_{\boldsymbol{Spr}}$. We also show the orientation angle of the trajectory β measured from the z direction. In Panel (b), we show the radius of the circle the beads are arranged in denoted by r. 87

3.24 Phase difference over time between three neighbouring beads arranged equidistantly around a circle of radius $r = 5$ as part of the bead and spring model for both Stokeslets and Blakelets with $\beta = 0$ and $\beta = \pi/4$. The springs here have natural length $l = 0.5$. 88

3.25 End Phase difference over three beads arranged around a circle of radius $r = 5$ of a bead and spring model over the angle β. 89

3.26 Figure showing steady states for 3 Beads in a circle of radius $r = 5$ for $\beta = 0$. We show the phase difference over time for an initial Phase Difference of $\pm 2\pi/3$ for both Stokeslets and Blakelets where we see that these are stable fixed points. 90

3.27 Phase difference over time between twenty (Panels (a) and (b)) and twenty one (Panels (c) and (d)) neighbouring beads arranged in a circle of radius $r = 8$ as part of the bead and spring model for both Stokeslets and Blakelets with $\beta = 0$. The springs have natural length of $l = 0.5$. We note that Panel (a) for twenty beads modelled with Stokeslets is plotted over a much longer time frame than the other panels. 91

3.28 Phase difference over time between twenty (Panels (a) and (b)) and twenty one (Panels (c) and (d)) neighbouring beads arranged in a circle of radius $r = 8$ as part of the bead and spring model for both Stokeslets and Blakelets with $\beta = \pi/4$. 93

3.29 Figure showing steady states for 21 Beads in a circle of radius $r = 8$ for $\beta = 0$. This shows the phase difference over time for Phase Difference of $\pm 2\pi/21$ for both Stokeslets and Blakelets. 94

3.30 Figure showing steady states for 21 Beads in a circle of radius $r = 8$ for $\beta = 0$. This shows the phase difference over time for an initial Phase Difference of $\pm 4\pi/21$ for both Stokeslets and Blakelets. 96

4.1 Screenshot showing the title page for the app titled algal colony suite. The three buttons allow you to build a swimmer model up in the app, load a saved model and run the currently loaded swimmer to find its swimming behaviour. 102

4.2 Screenshot showing the section of the app for creating the body of the swimmer. The sliders allow you to control the size and position of the cells. The buttons in the bottom right allow you to add the reflections of the currently created cells. This includes the reflection in the x axis, reflection in the y axis and a 4 fold reflection. 103

4.3 Screenshot showing the section of the app for positioning the flagella on the body. The sliders position the flagella on the cell using localised polar coordinates. 104

4.4 Figure showing how the displacement by *Chlamydomonas* changes for an increasing number of quadrature points on the flagella with the waveform given in equation (2.35) taken from Gallagher and Smith (2018). This is shown for three set values of the number of Force points. Red - 20 Force points, Blue - 30 Force Points and Black - 40 Force Points. 105

4.5 Figure showing how the displacement by *Chlamydomonas* changes for an increasing number of quadrature points on the flagella with the waveform given in equation (2.36) which was calculated by fitting to an experimental waveform. This is shown for three set values of the number of Force points. Red - 20 Force points, Blue - 30 Force Points and Black - 40 Force Points. 106

4.6 Figure showing how the displacement by *Chlamydomonas* changes for an increasing number of Quadrature points on the body of the swimmer for three set values of the number of Force points. Red - 20 Force points, Blue - 30 Force Points and Black - 40 Force Points. 107

4.7 Figure showing the level set surface of *Chlamydomonas* with a synchronous (a), and asynchronous (b) beat used in the Nearest neighbour method. The scale bar has length $5\mu m$. 109

4.8 Swimming behaviour of *Chlamydomonas* over 1 beat. (a) shows the z displacement over time for a synchronous beating *Chlamydomonas* with Flagella from $10 - 12\mu m$ and (b) shows the trajectory of *Chlamydomonas* over one beat with an asynchronous beat with a length of $11\mu m$. 111

4.9 Figure showing the level set surface of *Tetrabaena* with a (a) low , (b) medium and (c) high amount of mucilage used in the Nearest neighbour method. The scale bar has length $20\mu m$. 111

4.10 Figure showing the displacement and speed of *Tetrabaena* for flagella length of $10 - 40\mu m$. Panel (a) shows the z displacement of *Tetrabaena* for these flagella lengths and Panel (b) shows the speed of *Tetrabaena* with flagella of length $10 - 40\mu m$ and frequency linearly decreasing from 60 to 10 from small to large flagella starting with $60Hz$ for $10\mu m$ flagella to $10Hz$ for $40\mu m$ flagella. 112

4.11 Figure showing a comparison of the swimming behaviour for *Tetrabaena* with different levels of mucilage displaying the z displacement for the swimmers. We can see that there is very minimal difference between these results. 113

4.12 Figure showing the level set surface of *Gonium* with a metachronal wave along the peripheral flagellum used in the Nearest neighbour method. Panel (a) shows a symplectic wave and Panel (b) shows an antiplectic wave. The scale bar has length $20\mu m$. 114

4.13 Figure showing the displacement of *Gonium* over one beat. Our model for *Gonium* has flagella with a length of $40\mu m$ and a frequency of $10Hz$. Panel (a) shows the z displacement from a synchronous beat. Panels (b) and (c) show the 3D trajectory for *Gonium* with a symplectic and antiplectic metachronal wave respectively where the x component of the trajectory is shown by the colour. 115

4.14 Figure showing a comparison of the swimming behaviour for *Gonium* with different levels of mucilage displaying the z displacement for the swimmers. Our model for *Gonium* has flagella with a length of $40\mu m$ and a frequency of $10Hz$. We can see that there is very minimal difference between these results. 116

4.15 Figure showing the displacement of *Pandorina* over one beat. Our model for *Pandorina* is spherical swimmer with radius $\sim 15\mu m$ has flagella with a length of $20\mu m$ and a frequency of $25Hz$. We show the z displacement from a synchronous beat. 117

4.16 Figure showing the displacement of *Eudorina* over one beat. Our model for *Eudorina* is spherical swimmer with radius $\sim 50\mu m$ has flagella with a length of $20\mu m$ and a frequency of $25Hz$. Panel (a) shows the z displacement from a synchronous beat. Panels (b) and (c) show the 3D trajectory for *Eudorina* with a symplectic and antiplectic metachronal wave respectively where the x component of the trajectory is shown by the colour. . . 118

4.17 Figures showing the z displacement for *Pleodorina* over one beat. Panel (a) shows the displacement for a single beat with different colony radii. Panel (b) and (c) show the z displacement for a *Pleodorina* with a colony radius of $75\mu m$, with a Symplectic and antiplectic beat respectively. For all Panels the flagella have length $20\mu m$ and frequency of $25Hz$. 119

4.18 Figure Showing the model straight line speed of *Pleodorina* for different colony radii from $50\mu m - 150\mu m$. 119

4.19 Figure showing the model velocities for Volvocine green algae showing the model results for Synchronous beating as well as for a metachronal wave of a nondimensional wave number of 1 and -1 where applicable. 121

4.20 Figure showing the Discretisation of *Didinium*. Panel (a) shows an experimental image of *Didinium* (Antipa, 1968), Panel (b) shows our model for the discretisation of *Didinium* using level sets and Panel (c) shows the radius r, of the swimmer at the point on the centre line given by arclength s. The values for the arclength and radius are nondimensional with respect to the flagella length. 124

4.21 Figure showing the flux produced by flagella over a line in x direction of the length of the circumference of *Didinium* at the ciliary girdle location. We show the convergence of the y component of the flux for increasing number of flagella beating in the y direction. Panel (a) displays how the flagella are arranged and Panels (b) and (c) shows the convergence results. Panel (b) gives the results for flagella represented as a single point for both synchronous($k = 0$) and metachronal($k = \pm 2$) beating and Panel (c) shows the convergence using full discretised flagella. On Panels (b) and (c) we show the number of flagella for which most of our results are taken with an o symbol. We also show the number of flagella used for our results with a higher number of flagella. 125

4.22 Figure showing the z displacement of our model *Didinium* for different flagella orientations and Metachronal waves over one beat. In all cases the flagella have length of $17\mu m$. The top row displays results for both a synchronous beat shown by $k = 0$ and a metachronal wave moving to the right (dexioplectic) shown for positive k and the bottom row shows results for a metachronal wave moving to the left (laeoplectic) shown for negative k. Panels (a) and (d) show the results for a forward swimming *Didinium* with flagella pointing straight down with a frequency of $15Hz$. Panels (b) and (e) show the results for a forwards swimming *Didinium* with flagella pointed down and tilted 18 degrees to the left with a frequency of $15Hz$. Panels (c) and (e) present the displacement for a backwards swimming *Didinium* with flagella pointed up and tilted 24 degrees to the right with a frequency of $26Hz$. 127

4.23 Figure showing the 3D (left) and $x-y$ (right) trajectories for forward swimming *Didinium* with no tilt. Panels (a) and (c) show the 3D trajectory for a metachronal wave number of ± 1 for a metachronal wave to the right (a) and left (c). Panels (b) and (d) show the $x-y$ trajectories for the odd wave number metachronal waves. $k = \pm 3, \pm 5, \pm 7, \pm 9$ are shown in the axes in the centre of the panel since they are much smaller than the $k = \pm 1$ case and would not show up otherwise. 129

4.24 Figure showing the swimming behaviour of Didinium swimming forwards (top) and backwards (bottom) with tilted flagella. Results are calculated for a Didinium with a total of 600 flagella or 300 flagella per ciliary girdle beating with a Metachronal wave of wavenumber $k = 10$. Panels (a) and (c) show the z displacement and Panels (b) and (d) show the ω_3 component of the angular velocity. 130

5.1 We show our Bead and Spring model for *Chlamydomonas*. We find the positions of the beads on the body using the Level set method with each bead in the body connected to all other beads on the body using springs. . 134

5.2 Phase difference over time between the flagella beads of our *Chlamydomonas* bead and spring model with multiple beads to represent the full body. We show results for an initial phase difference of 0 and $\pm\pi$ using Stokeslets. . . 134

5.3 Figure showing the displacement of our bead and spring model for *Chlamydomonas* with an initial phase difference of π. Panel (a) shows the x displacement and Panel (b) shows the z displacement 135

5.4 Phase difference over time between 2 beads over a boundary beating in opposite directions like *Chlamydomonas* flagella. The spring centres of the beads are placed a distance $d = 1.3$ apart. 136

5.5 We show our Bead and Spring model for our multiciliate swimmer with 12 flagella. We find the positions of the beads on the body using the Level set method with each bead in the body connected to all others beads on the body using springs. 137

5.6 Phase difference over time between the neighbouring flagella beads of our Spherical multiciliate bead and spring model with 12 flagella and multiple beads to represent the full body. We show results for an initial phase difference of 0 and $\pm 2\pi/12$ using Stokeslets. 139

5.7 Phase difference over time between the neighbouring flagella beads of our spherical multiciliate bead and spring model with 12 flagella and multiple beads to represent the full body. We show results for an initial phase difference of $\pm 4\pi/12$ using Stokeslets. 140

5.8 Figure showing the displacement of our bead and spring model for our spherical multiciliate swimmer with an initial phase difference of $4\pi/12$. Panel (a) shows the x displacement and Panel (b) shows the y displacement and Panel (c) shows the z displacement. 141

5.9 We show our Bead and Spring model for *Gonium* in Panel (a) and *Didinium* in Panel (b). For clarity, the beads related to the body are in black and the beads relating to the flagella are in red. We also omit the springs in the figure that are not attached to any of the flagella related (red) beads to make the figure more clear. 143

LIST OF TABLES

4.1 Table collating the model details for the Volvocine green algae. Where Experimental swim speed is written as unknown, it was unable to be found. For the flagella of the spherical swimmers, we assume their beating to be the same as the beating of *Volvox* flagella. We take their length to be $20\mu m$ (Pedley et al., 2016), and their frequency to be $25Hz$ (Solari et al., 2011) . 122

CHAPTER 1

INTRODUCTION

1.1 Microswimmers

A microswimmer is a microscopic organism or cell that is able to move and swim through a fluid. In Figure 1.1, we see four examples of microswimmers that swim using different techniques (Stocker and Durham, 2009; Gillies et al., 2009). These are the green alga *Chlamydomonas*, the bacterium *Escherichia coli*, the cell *Spermatozoa*, and the protozoan *Paramecium*. Typically swimming is achieved through moving long appendages known as flagella or cilia to propel the swimmer forward. Data on many swimming microorganisms has been collected for a large number of unicellular swimmers (Velho Rodrigues et al., 2021). This thesis mostly concerns the modelling of microswimmers with many cells, many cilia, or both.

The ability to swim plays a vital role in many aspects of life and there are many reasons why swimming at the microscale is required and is interesting to study. One reason is to aid in fertility, as with the swimming of *Spermatozoa* cells towards the ovum (Lauga and Powers, 2009). Another reason is to move towards sources of energy. For example, *E. coli* detects and moves to areas of high concentration of nutrients, a process known as chemotaxis (Hansen et al., 2008) and the green algae *Chlamydomonas reinhardtii* detects and moves towards areas of light, in a process known as phototaxis (Goldstein, 2015). Microswimmers also use swimming as a tool to avoid predators. An example of this is

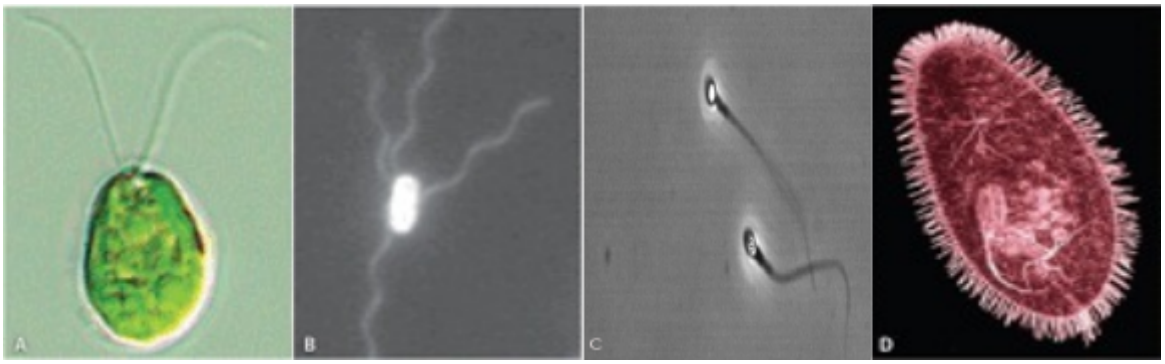


Figure 1.1: This Figure shows four examples of microswimmers. Panel A shows a *Chlamydomonas reihardtii*, a single celled alga that swims by moving its two flagella in a breaststroke pattern. Panel B shows an *E. coli*, a bacterium cell with multiple rotating helical flagella that bundle together to give the cell a run and tumble motion. Panel C shows two sperm cells that swim by propagating a travelling bending wave along its flagellum. Panel D shows a *Paramecium* cell which has multiple cilia over its surface, beating in a metachronal wave to help it swim. Panels A, B and D are take from Stocker and Durham (2009), and panel C is taken from Gillies et al. (2009)

seen in *Chlamydomonas reinhardtii* which uses a tumbling technique to change direction to aid in avoiding predators (Stocker and Durham, 2009). Therefore, swimming plays an integral part to life at the microscale.

Studying how microswimmers swim is useful to consider for many reasons. For example, one area of study related to microswimmers looks at microbots. For microbots to swim, the designs of many models of microbots often take inspiration from real microswimmers in nature to enable them to swim efficiently (Tabak and Yesilyurt, 2010). Developing microbots can be used in many important areas. For example, microbots could be used as part of targeted drug delivery. This would be useful in many areas of medicine to allow the drug to be accurately administered to the target area easily (Nelson et al., 2010). Microswimmers are also useful to study to better understand fertilisation due to the complicated nature of sperm cells swimming through the fallopian tubes.

Microswimmers were first discovered by Leeuwenhoek (1677) and were found in rain water. However, it was not until 1951 that the first mathematical models for the swimming of microswimmers were produced, which considered the swimming of an infinite sheet (Taylor, 1951). Since these, there have been many studies of microswimmers with

mathematical models of their swimming behaviour as well as studying their biology, such as their structure, or studying microswimmers as part of predator prey dynamics. In this thesis, we will focus on studies of their swimming behaviour.

1.1.1 Eukaryotic and Prokaryotic Swimmers

Life on earth is split across two types of organisms, eukaryotes and prokaryotes, both of which contain a wide variety of commonly studied microswimmers. Prokaryotic microswimmers include bacteria such as *E. coli* and archaea. Prokaryotic cells do not contain a nucleus and only form single celled organisms (Vellai and Vida, 1999). Eukaryotic cells are those with a nucleus, such as green algae cells, and they make up all multicellular organisms as well as many single celled organisms. In this thesis, we will focus on eukaryotes.

Cilia or flagella play vital roles in many areas of nature such as for the swimming of both eukaryotic and prokaryotic microswimmers as well as the transport of fluid and particles. One example of this is found in the lungs where the cilia beat to remove foreign particulates to clear the airways (Bustamante-Marin and Ostrowski, 2017). These cilia are found throughout the airways with those in the upper airway acting as the body's first line of defence against airborne pathogens (Jing et al., 2017). We also find cilia in the early development of vertebrate embryos (Dasgupta and Amack, 2016). The cilia produce a directional fluid flow that is critical to the left-right asymmetric organ patterning present in vertebrates. We typically use the term cilia for shorter hair like appendages found on eukaryotic cells, typically for fluid transport and often found in large groups. Flagella are typically longer than cilia and are found on both eukaryotic and prokaryotic cells. They are typically found in fewer numbers on a cell than cilia and are used for swimming, though some swimmers such as Paramecium contain a large number of cilia.

One major difference between eukaryotic and prokaryotic swimmers is the significant difference in their flagella (Lighthill, 1976). Prokaryotic swimmers, such as E. coli, have rigid helical flagella that have two parts. The main part of the flagellum is the rigid

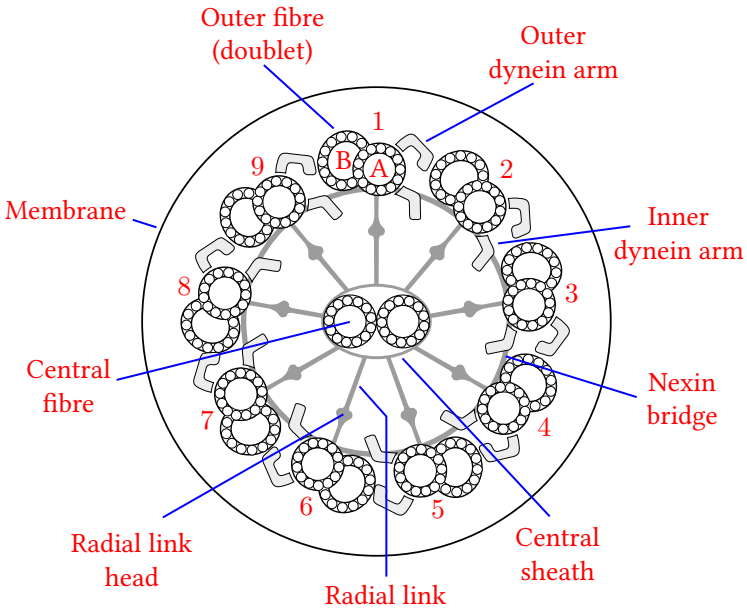


Figure 1.2: Diagram showing the 9+2 arrangement of microtubules in the axoneme for Eukaryotic flagella taken from Montenegro-Johnson (2013)

helical filament. This is then connected to the head of the flagella via a curved flexible hook (Lighthill, 1976). To swim, these flagella are rotated at the base creating a travelling corkscrew wave.

Eukaryotic swimmers have flagella with a 9+2 arrangement of microtubules as part of its internal structure known as the axoneme as seen in Figure 1.2 taken from Montenegro-Johnson (2013). This arrangement consists of 9 doublet tubules in a circle around 2 singlet tubules (Lighthill, 1976). The doublet tubules consist of a circular A tubule with an incomplete circular B tubule attached to it. On the other side of the A tubule, the microtubule doublet contains two dynein arms which are vital to produce the force to move the flagellum.

To swim, these microtubules slide past each other to create a moment to bend the flagellum. Unlike the bacterial flagella which are only driven at the base of the flagellum, the eukaryotic flagellum actively bends along its entire length. This results in a wide variety of ways that eukaryotic flagella are able to beat of which some will be discussed in the next section.

The most commonly studied prokaryotic swimmer is *E. coli*. However, many other

prokaryotic swimmers have also been studied. These bacteria can vary in number and placement of flagella (Schuhmacher et al., 2015). Bacteria cells with just one flagellum are known as monotrichous cells. An example of this type of bacteria is *Pseudomonas fluorescens* (Ping et al., 2013) which lives in soil promoting the growth of plants. Monotrichous bacteria often use different techniques when swimming at the microscale. For example, some monoflagellate bacteria are known to swim backwards when reversing the rotation of the flagella, rather than the rotation caused by unbundling of the flagella (Ping et al., 2013). Flagellated bacteria can also be categorised by the position of their flagella. These tend to be polar bacteria that have flagella located around the poles of a cell with bacteria with a tuft of flagella at one pole referred to as lophotrichous and bacteria with flagella at each pole referred to as amphitrichous (Velho Rodrigues et al., 2021). *E. coli* is an example of a peritrichous bacteria with its flagella placed randomly over the cell.

Rather than relying solely on flagella to swim through fluid, some bacteria swim through deformations of their body (Velho Rodrigues et al., 2021). Examples of this type of bacterial swimmer are cells from the Spirochaetes phylum. These bacteria swim through internal flagella that cause helical waves through the body.

While bacteria are the most prevalent and commonly studied prokaryotic microswimmer, there are also prokaryotic swimmers that are types of archaea rather than bacteria. Very few species of archaea have been studied in relation to that of bacteria or eukaryotic swimmers with data of many of them collated in Velho Rodrigues et al. (2021). The flagella of archaea are very similar to bacterial flagella with rotating flagella. A study on swimming behaviour of an archaea is discussed in Kinosita et al. (2016) using the model organism, *Halobacterium salinarum*.

Eukaryotic swimmers have been very commonly studied for both plant and animal species. These can range from cells with a single flagellum such as sperm cells to large multiciliate swimmers such as *Paramecium*. Eukaryotic swimmers also include and allow us to study multicellular microswimmers such as the Volvocine green algae which we will present models for in this thesis. We now discuss and categorise the different swimming

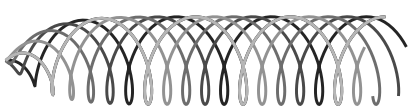
techniques that are utilised by both eukaryotic and prokaryotic microswimmers in more detail.

1.1.2 Swimming techniques

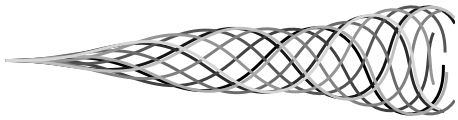
There are a wide variety of techniques that microorganisms can use to beat a flagellum in order to swim. Figure 1.1 shows four examples of microswimmers each with a different swimming technique. We show examples of these different flagella beats in Figure 1.3. We first discuss *Chlamydomonas* (shown in Panel (A) of Figure 1.1) which swims by beating in a breaststroke or sweeping motion as shown in Panel (c) of Figure 1.3. This is also the beating found in most cilia that are not used for swimming, such as those in the airway.

This beat is made up of an effective stroke and a recovery stroke. During the effective stroke the extended flagella move down in a sweeping motion as shown in Panel (a) of Figure 1.4. This then propels the swimmer forward enabling it to swim. However once it has finished the effective stroke part of the beat, the flagella needs to get back up so that it can redo the effective stroke to continue swimming forward. For this it utilises the recovery stroke. During the recovery stroke the flagella stays bent moving up ready for the effective stroke. It does this by propagating the bend along the flagella as shown in Panel (b) of Figure 1.4. This recovery stroke does cause the swimmer to move back slightly. However the recovery stroke exerts less force on the fluid, by moving tangentially through it, than the main stroke to move the swimmer forward. Therefore, the swimmer moves forward overall after each beat allowing the microswimmer to swim. This is a widely used technique and is seen in all members of the Volvocine Green algae. It is also the motion used by individual cilia that form part of a ciliary carpet or on many multiciliate swimmers.

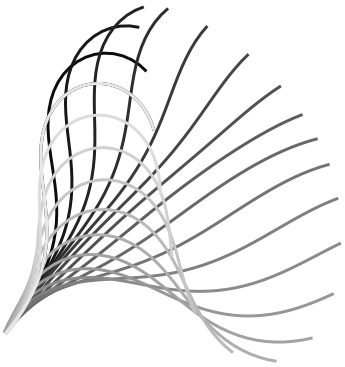
The next swimming technique we will discuss is used by bacterial swimmers such as *E. coli* as shown in Panel (B) of Figure 1.1 for which the helical motion of a single flagellum is shown in Panel (a) of Figure 1.3. *E. coli* and other bacteria such as *Bacillus subtilis* (Mukherjee and Kearns, 2014) have rigid helical flagella which are rotated and bundled



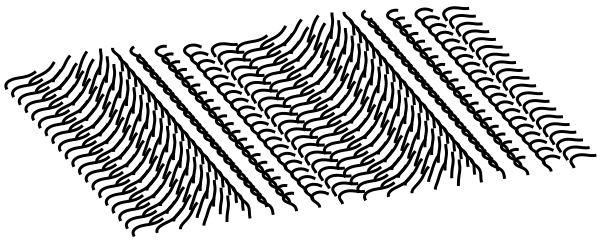
(a) Bacteria Flagellum



(b) Sperm Flagellum

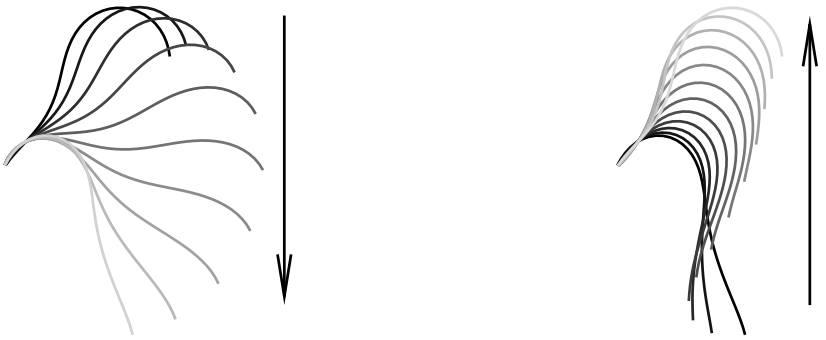


(c) Volvocine Flagellum



(d) Metachronal Wave

Figure 1.3: Figure showing examples of different flagella beats. Panel (a) shows a model example of a rotating helical flagella, as seen in bacteria such as *E. coli*. Panel (b) shows the beating of a sperm flagellum. In Panel (c) we show a model example of a beating cilia in a sweeping motion. This beating pattern is used for algal swimmers such as *Chlamydomonas*. In Panel (d) we show a large group of cilia beating with a metachronal wave along the cilia as part of a ciliary carpet. Metachronal waves are seen in swimming for swimmers such as Paramecium. Panels (a)-(c) uses a greyscale colouring to represent the time step of the beat, fading from black as the time, t increases.



(a) Effective Stroke (b) Recovery Stroke

Figure 1.4: Figure displaying the effective stroke in Panel (a) and recovery stroke in Panel (b) for the Effective-Recovery beat that is utilised by the beating of a cilia or Volvocine flagellum.

together to produce a corkscrew motion of the flagella. These rigid flagella are able to bundle together due to the bending flexibility of the hook structure with the hooks length being important for the stability of the flagella bundle (Nakamura and Minamino, 2019). This propels the swimmer through the fluid in a straight line forming the main bulk of the motion. The flagella then rotate in the opposite direction causing the flagella to unbundle. The swimmer then tumbles rotating before then starting swimming forward in a different direction. This method of steering is known as run and tumble dynamics (Berg and Brown, 1972).

Run and tumble dynamics are most often found in bacterial swimmers swimmers such as *E.coli*. Other swimmers also adopt this technique, such as *Chlamydomonas* (Stocker and Durham, 2009). *Chlamydomonas* uses its normal synchronous effective and recovery stroke beating to form the run part of the dynamics. It then tumbles orienting itself to face a new direction by using an antiphase beat (Stocker and Durham, 2009).

Another swimming technique is used by swimmers such as the sperm cells of multiple different animals as shown in Panel (C) of Figure 1.1. The sperm cells propagate a travelling wave along the flagella propelling it through the fluid. An example of this beating is shown in Panel (b) of Figure 1.3. This beat is highly dependent on the fluid the sperm cell is in with large variations in the beat for different levels of viscosity. The

effects of viscosity on sperm are discussed in Kirkman-Brown and Smith (2011) which discuss how sperm can swim in both viscous and non viscous mediums and how this needs to be taken into account when studying its swimming. Different behaviour is found due to the viscous damping of the active bending of the flagella which changes the beat.

Swimmers such as *Paramecium* (as shown in Figure 1.1) display another swimming technique. These swimmers swim through coordination of many flagella over its surface that form a ciliary carpet. This coordination helps to move and orient the swimmer through the fluid as desired. We show an image of an example of a ciliary carpet in Panel (d) of Figure 1.3. Other examples of microswimmers that use this technique include the multiciliate *Opalina ranarum* (Velho Rodrigues et al., 2021). Ciliary carpets are also typically used for pumping fluid by cilia that are not used for swimming.

1.1.3 Metachronal Waves and Multiciliate Swimmers

We now discuss the coordinated action of multiple beating cilia in more detail. On multiciliate swimmers, the flagella highly coordinate their beating to form what is known as a metachronal wave (Elgeti and Gompper, 2013). This wave is produced by a sequential beating of the cilia, causing a travelling wave to move through the cilia as seen in Panel (d) of Figure 1.3. If this travelling wave is moving in the same direction as the effective stroke of the cilia, then it is a symplectic wave. Otherwise, if the metachronal wave moves in the opposite direction then it is an antiplectic wave. Both of these types of metachronal wave are shown in Figure 1.5. Metachronal waves can sometimes also travel perpendicular to the effective cilia stroke. This is referred to as dexioplectic if the effective stroke is to the right of the metachronal wave and laeoplectic if it is to the left.

Metachronal waves in swimming have been studied in many different multiciliate swimmers. These can be found and have been studied in single celled swimmers such as Paramecium (Machemer, 1972) or Opalina (Tamm and Horridge, 1970) as well as in multicellular swimmers such as Volvox (Brumley et al., 2015). Metachronal waves in microswimmers are also studied more generally. For example Rode et al. (2021) studies the efficiency



(a) Symplectic (b) Antiplectic

Figure 1.5: Figure displaying a metachronal wave in both symplectic (travelling wave moves in the same direction as the effective stroke) and antiplectic (travelling wave moves in the opposite direction to the effective stroke) directions. The metachronal wave is produced by sequential beating of cilia producing a travelling wave along the cilia. We show the direction of the metachronal waves with arrows above the cilia.

of metachronal waves in regards to translational and rotational velocity of swimmers for various factors of a metachronal wave. They also study how a metachronal wave can lead to the emergence of helical swimming

As well as in multiciliate swimmers, metachronal waves are also found in many other areas of nature where large groups of cilia are found. For example, metachronal waves are used in transporting mucus and other particulates out of the airways (Ramirez-San Juan et al., 2020), as well as in embryos of vertebrates causing the left right asymmetry found in them.

Since metachronal waves tend to form naturally over most groups of densely packed cilia, many studies have been done into the hydrodynamic interactions of how these metachronal waves emerge. One method for this considers highly simplified models for beating cilia. For example, Niedermayer et al. (2008) models a beating cilium as a small spherical bead with a mostly circular trajectory. We will use a similar approach in this thesis for studying the synchronisation of flagella. This allows them to study the interactions between two neighbouring flagella and the synchronisation and phase locking between them. This study is then extended to a chain of cilia. An advantage of simpler models such as this is that they allow their models to be studied analytically to describe synchronisation and phase locking between cilia.

Simplified models can provide a good understanding of synchronisation and phase locking between neighbouring flagella. However, due to their simplicity, they are unable to capture the full realistic mechanics of the cilia and metachronal waves. Therefore another method for studying metachronal waves considers more detailed realistic cilia. These typically contain more detailed realistic studies on metachronal waves but are too complicated to be studied analytically. For example, Gueron and Levit-Gurevich (2001) models the internal bending mechanism flagella by taking into account the 9+2 structure of the eukaryotic cilia. These more complicated models, model the cilia as a filament rather than just a point. These are studied for models that try to reproduce the beat of a real cilium as well as for an optimised beat.

Another area of study in metachronal waves considers the optimal metachronal wave in groups of cilia. For example, Osterman and Vilfan (2011) studied the optimal metachronal beating pattern for a lattice array of cilia, finding that the highest efficiency is found for the antiplectic wave. Milana et al. (2020) also finds this to be true for a line of cilia. As well as multiciliate swimmers, we will also model multicellular swimmers in this thesis which we will introduce in the next section.

1.1.4 Multicellular Swimmers

The transition of life from single celled organisms to large multicellular organisms is a fundamental step of evolution (Szathmáry and Maynard Smith, 1995). There are many benefits to multicellularity which makes it a desirable trait to evolve. One benefit is that larger multicellular organisms are typically more adept at being able to either avoid predators or find food (Solari et al., 2007).

Multicellularity is only seen among eukaryotic organisms (Szathmáry and Maynard Smith, 1995). However, the fact that multicellularity is beneficial for organisms can even be seen among prokaryotes, for which multiple single celled organisms can aggregate to form bacterial colonies as seen in Figure 1.6. The cells in these colonies cooperate with each other to aid in various functions as cells would in multicellular organisms (Velicer and Yu,

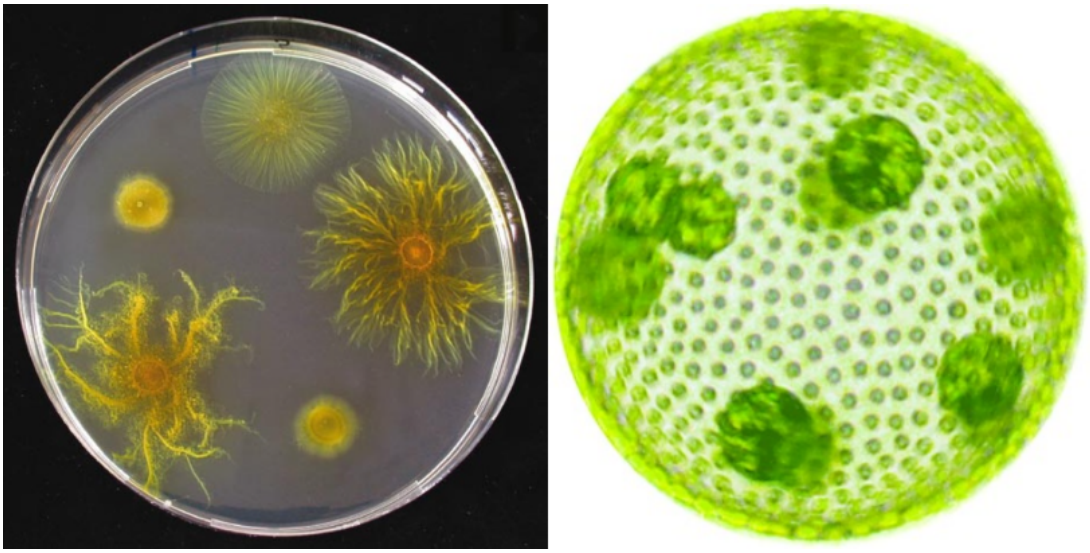


Figure 1.6: Figure showing examples of two types of colony. The left image shows bacterial colonies formed by the swarming of bacteria taken from Velicer and Yu (2003). The right image shows the algal colony *Volvox*, taken from Pedley et al. (2016).

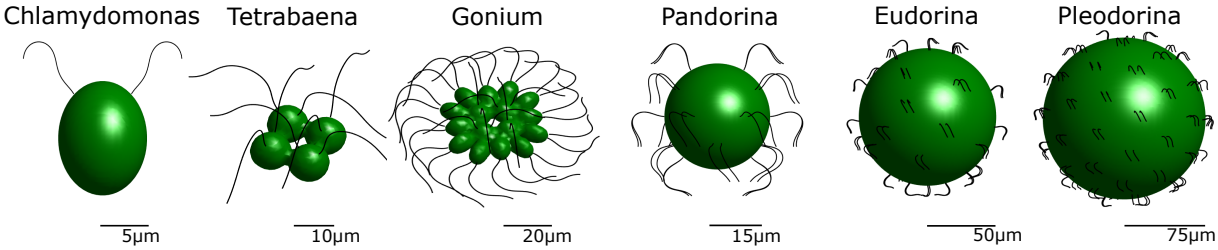


Figure 1.7: A recreation of Figure 1 from Arakaki et al. (2013), showing the Volvocine green algae from smallest to largest using the model swimmers created in our app the Algal Colony Suite which will be introduced in Chapter 4.

2003). Such colonies of undifferentiated bacterial cells potentially provide an insight into how more complex multicellularity (such as that found in many eukaryotic organisms) could have evolved (Velicer and Yu, 2003).

In this thesis we are interested in studying the swimming of both multicellular and multiciliate swimmers. A large amount of the swimmers we will focus on make use of the effective recovery stroke swimming technique as well as metachronal waves which we will consider as part of modelling their swimming behaviour. For example, we will look at modelling the swimming of the Volvocine Green algae for each of the swimmers shown in Figure 1.7 as recreated from Arakaki et al. (2013) as well as multiple other swimmers. The Volvocine Green algae are typically regarded as model organisms for

studying multicellularity. This is because of their wide range of colony sizes ranging from the single celled *Chlamydomonas* to the larger very multicellular *Volvox*. Having introduced different types of swimmers,we will now go into a bit more depth into the underlying physics and mechanisms of propulsion of swimmers at the microscale, before giving a review of key mathematical models of microswimmers.

1.2 Physics of Microscale Swimming

At the microscale, surface forces dominate volume forces. This can be seen since the surface area to volume ratio is $\sim 1/L$ where L is the typical length scale of the problem. Therefore, movement through a fluid is dominated by the surface forces such as the viscous stresses (Lighthill, 1976) and inertia, being a volume force, has a negligible effect. This is expressed mathematically by the Reynolds number given by $Re = \rho UL/\mu$ where U and L are the characteristic velocity and length of the swimmer respectively, ρ is the density of the fluid and μ is the viscosity. This number arises from the nondimensionalisation of the Navier-Stokes equations which describe the motion of water-like fluids.

The Reynolds number can be thought of as the ratio of inertial forces to viscous forces and was initially found as part of an experiment performed by Reynolds (1883). For microscale swimmers, the characteristic length scale L and characteristic velocity U are typically both very small relative to the kinematic viscosity, hence the Reynolds number is also very small. Therefore, we can see that the swimming of microorganisms will be dominated by viscous effects.

Swimming at the microscale has difficulties that are not present with macroscale swimming. For example, a microswimmer with one rigid flagellum moving up and down would not be able to move and make progress in swimming through the fluid (Purcell, 1976). This comes from the fact that at the microscale, an organism will not be able to swim using a time-reversible motion (reciprocal stroke) as shown in films demonstrating low Reynolds number flow (Taylor, 1967). The reason for this is at low Reynolds number,

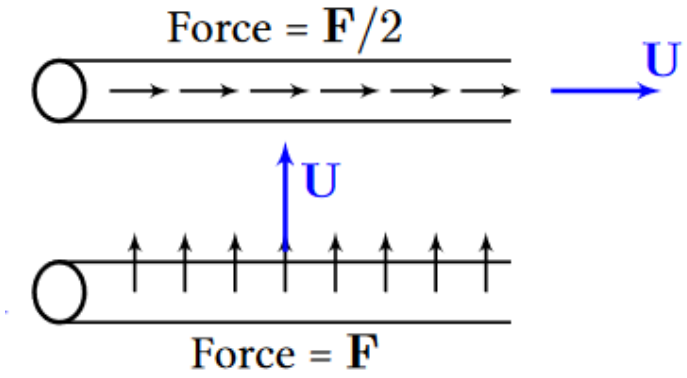


Figure 1.8: Figure showing a schematic demonstrating the effect of drag anisotropy. This figure is taken from Figure 3 in Montenegro-Johnson et al. (2012).

fluid inertia has a negligible effect. Microscale swimmers overcome this difficulty in various ways as discussed in Section 1.1.2 on swimming techniques.

An important component in understanding how microswimmers are able to swim through fluid is the drag anisotropy in the flagella. For a slender rod the normal drag force is found to be approximately double the tangential drag force (Gray and Hancock, 1955). We show a schematic to demonstrate this effect in Figure 1.8 taken from Montenegro-Johnson et al. (2012). This idea can be used to approximate the forces and moments determining the movement of a swimmer in a method known as resistive force theory.

Swimmers are able to utilise this drag anisotropy to allow them to swim at the microscale in different ways as seen in Figure 1.3. For example, this is seen in the cilia (breaststroke) beat, with the difference between its effective stroke and recovery stroke. Using this difference, the flagella are able to utilise the drag anisotropy, allowing swimmers with that type of beat, such as *Chlamydomonas*, to swim.

From a fluid dynamics perspective, there are typically two main types of swimmer that can swim at the microscale. We find this because swimmers at the microscale exert no net force on the fluid. Due to the speed they swim, the drag force balances the propulsive force that they produce. With no net force, the next order singularity is a force dipole, and there are two ways to do that. These are called pushers and pullers (Lauga and Powers, 2009). How these interact with the fluid can be seen in Figure 1.9.

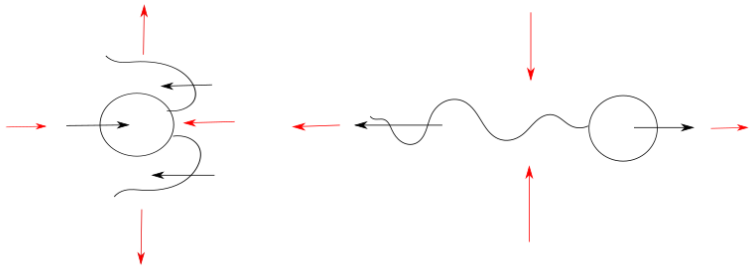


Figure 1.9: Diagram showing the forces from typical microswimmers (in black) and flow field (in red). The left shows a typical puller drawing fluid in along its swimming direction and pushing it out from the sides. The right shows a typical pusher which pushes fluid away along its swimming direction and draws it in to the sides.

Swimmers that are described as pushers use their flagella to push the fluid back to propel themselves forward, which also causes fluid to be drawn in to the side of the pusher through conservation. For this they usually have their flagella behind their body. Examples of microwimmers described as pushers would be *spermatozoa* cells and *E. coli* cells.

Pullers however, use their flagella to pull themselves through the fluid drawing fluid towards them and pushing it out at the sides pulling themselves along to be able to swim, with their flagella typically being in front of their body. *Chlamydomonas* is an example of a microswimmer that swims in this way. However for multicellular or largely multiciliate microswimmers, this description of pusher and puller is less useful in describing their swimming behaviour which is why in this thesis we will consider fully resolved models.

A swimmer being a pusher or puller also helps to determine how two swimmers in close proximity affect each other. Pushers draw fluid in towards their side. Therefore, two pushers are attracted to each other while swimming (Lauga and Powers, 2009). For example, this can be seen to happen with the many sperm cells of various species that typically tend to aggregate together aiding them in being able to swim faster. This is an example of what is known as bacterial turbulence where interactions between cells can create an instability in a suspension of many swimmers (Dunkel et al., 2013). These suspensions have been seen to produce vortices and jets much larger than the individual cells

(Lauga and Goldstein, 2012). In a similar mechanism to bacterial turbulence, swimmers that are described as pushers, such as sperm, are found to accumulate near surfaces. This was initially observed when trying to view bull sperm under the microscope (Rothschild, 1963).

1.3 Mathematical Studies of Microswimmers

1.3.1 Taylor's Swimming Sheet

One of the earliest mathematical studies of how something could swim at the microscale examined the swimming of an infinite sheet (Taylor, 1951). This was the first work to consider, from a mathematical perspective, how a two-dimensional sheet could propel itself through a fluid without the use of inertia. To swim, the sheet propagated a sinusoidal wave form along its surface, propelling itself through the fluid. It was found that a sheet moving in this way moves at $2\pi^2 b^2/\lambda^2$ times the velocity of the wave propagation, where λ is the wave length, and b is the amplitude which is required to be small. This is known as Taylor's swimming sheet.

The effects of two swimming sheets moving using waves of the same amplitude and velocity at positions $y = \pm h$ were also studied by Taylor (1951). The phase of the wave on one sheet was considered to initially lag behind the other by an angle of 2ϕ, where $0 < \phi < \pi/2$. These swimming sheets were then analysed finding the stresses and pressures applied to the sheets. The direct effects of pressure on the two sheets is found to modify their wave frequency in such a way that the waves shift to be in phase with each other (Taylor, 1951).

Taylor's swimming sheet is still widely used and modified to consider various cases and find improvements. Sauzade et al. (2011) extended the pertubation series used for computing the swimming speeds of the sheet to arbitrary order. This extension of the model allowed for them to consider a swimming sheet with large amplitude waves.

Montenegro-Johnson and Lauga (2014) considered how Taylor's swimming sheet can be optimised by considering the swimming efficiency, described as the ratio of the swimming speed squared to the rate of the work done against the fluid of the sheet. This optimised swimming sheet was found by considering waves of both small and large amplitude. For small amplitude, the optimal wave form of the sheet was a single sine wave of period 2π. When extended to large amplitude waves, they found that the optimal sheet has the shape of a regularised cusp wave. This is found to be around 25% more efficient than the sine wave predicted using small amplitude waves.

The optimal shape for a flagellum moving with a planar wave as in the swimming sheet was also considered taking into account the effects of elasticity of the flagella (Lauga and Eloy, 2013). This found the optimal shape of the flagellum as a function of the sperm number. The sperm number is defined as the ratio of the viscous forces on the flagellum to elastic forces. For infinite sperm number, the shape tends to that of a saw-tooth wave, with this smoothing out for the sperm number becoming finite.

The swimming of Taylor's swimming sheet has also been considered in different types of fluids. For example, Hewitt and Balmforth (2017) considered the swimming of a sheet in a yield stress fluid. The velocity of the swimming sheet is found to increase compared to a Newtonian (or water-like) fluid for increasing Bingham number, where the Bingham number describes the ratio of the yield stress to the viscous stress. For the Bingham number much larger than one, the swimming speed is seen to tend to twice that of the swimming sheet in a Newtonian fluid (Hewitt and Balmforth, 2017).

In Du et al. (2012), Taylor's swimming sheet is studied for a viscous two-phase fluid containing two viscous fluids of different viscosities. This analysis finds that the speed in a two-phase fluid depends on the viscosities of both fluids. Although the swimming speed is always seen to be reduced for a two-phase flow compared to within a single fluid.

Taylor's swimming sheet is also studied in viscoelastic fluids by Riley and Lauga (2014). Here they model how a swimming sheet can have enhanced motion in a viscoelastic fluid. They find that the presence of the viscoelastic stresses can lead to an increase in the

waving amplitude of the swimmer. If this increase is large enough, then it is able to compensate for the damping from the non-Newtonian viscoelastic forces. This then leads to faster swimming in some viscoelastic fluids.

1.3.2 Slender Body Theory and Resistive Force Theory

The swimming sheet model by Taylor (1951) required an infinite swimming sheet as well as being unable to model a general waveform. Therefore, an important development in describing the swimming of microswimmers was made by Hancock (1953) which became known as slender body theory. This method is useful for modelling slender filaments such as flagella with the flagellum length much larger than its radius. This restriction is often seen to be true for a large number of flagella. Slender body theory is a way of modelling slender swimmers using a singularity based approach.

Slender body theory uses the Green's function known as the Stokeslet, that is used for solving for the flow due to a point force at low Reynolds number. In this method the singular stokeslets and source dipoles are distributed across the centreline of a headless flagellum swimming through a fluid. Distributing the singularities along the centreline is valid due to the slenderness of the filament but breaks down for non-slender swimmers. This method is able to take into account non-local hydrodynamic forces to obtain an accurate description of the swimming behaviour.

After introducing slender body theory, Gray and Hancock (1955) considered a more simplified model of microswimmers which became known as resistive force theory. This was an algebraic approximation to their previously introduced slender body theory. As with slender body theory, upon which this method is based, resistive force theory requires the length of the filament to be much larger than its radius. Another key assumption for this model is that the tangential and perpendicular hydrodynamic forces are approximately proportional to its tangential and perpendicular local body velocities respectively.

Resistive force theory is used to calculate the forces and moments on a filament. An important part in studying this involves looking at the drag coefficient. The tangential

drag coefficient is given as

$$C_t = \frac{2\pi}{\ln\left(\frac{2\lambda}{a}\right) - \frac{1}{2}}, \tag{1.1}$$

where λ is the wavelength of the flagella beat and a is the cross sectional radius of the flagellum, with

$$C_n/C_t \approx 2,$$

where C_n is the normal drag coefficient. It was shown that the drag coefficient associated with the normal motion is approximately twice that associated with the tangential motion. These drag coefficients were later improved by Lighthill (1976). They were given by

$$C_t = \frac{2\pi}{\ln\left(\frac{2q}{a}\right)}, \quad C_n = \frac{4\pi}{\ln\left(\frac{2q}{a}\right) + \frac{1}{2}}, \tag{1.2}$$

where $q = 0.09\Lambda$. Here Λ is the wavelength measured along the centreline of the flagellum.

In Gray and Hancock (1955), in which resistive force theory is first used, they studied the swimming of sea urchin *Spermatozoa* and how it propels itself. The velocity was found approximated for both large and small amplitude waves. For small amplitude waves, not considering the head, the velocity was found to be the velocity of wave propagation of the flagella multiplied by $\frac{2\pi^2 b^2}{\lambda^2}\left(\frac{C_n - C_t}{C_t}\right)$. This is seen to be equivalent to the velocity of the swimming sheet found by Taylor (1951) multiplied by a combination of the tangential and normal drag coefficients. This becomes identical to the value found for the velocity of the swimming sheet when $C_n/C_t = 2$. This calculation is found in terms of the waveform and frequency of beating flagellum.

Both Resistive Force Theory and slender body theory have both been widely used in the modelling of microswimmers since being introduced. Resistive Force Theory has been effective as a simplified way of finding information on many complicated problems. Examples of this include the modelling of the motion of *C. elegans* to accurately predict the path it takes from its undulations (Keaveny and Brown, 2017) using both the linear and nonlinear Resistive Force Theory model. Resisistive Force Theory has also been extended to the modelling swimming of slender filaments in non-Newtonian fluids (Riley

and Lauga, 2017).

Slender body theory is a more accurate way of modelling the swimming of a flagellum than the Resistive Force Theory (Johnson and J Brokaw, 1979). However, while this method mostly provides an accurate description of the swimming forces, there are inaccuracies at the endpoints of the flagellum. This is because the requirement of the flagellum being slender breaks down at the end points.

Many of the early models of slender body theory were only concerned with slender swimmers with a circular cross section. Therefore, Batchelor (1970) looked at the effect of the cross sectional shape by extending slender body theory to model slender swimmers with an arbitrary cross section, giving an improved integral equation for the motion of a more general slender body with arbitrary as well as slowly varying cross section. These integral equations are also rederived using an alternative method in Clarke (1972). This equation is then used to consider an example of a swimming uniformly twisted particle.

An improved version of slender body theory is derived from a boundary integral representation using asymptotic expansions by Koens and Lauga (2018). They show that the boundary integral formulation of the Stokes flow equations, can reduce to the singularity representation of slender body theory. They find a more algebraically accurate form of slender body theory that is able to handle arbitrary surface velocities.

1.3.3 Images for Complex Domains

Slender body theory and resistive force theory provide a good method for modelling slender swimmers in an infinite fluid and finding their velocity. However an issue with this is that many microswimmers are often found to accumulate at boundaries (Rothschild, 1963). To be able to deal with this Blake (1971a) developed the method of images for Stokes flows to model swimmers near no slip boundaries.

The method of images in Blake (1971a) looks at the Stokeslet solution (solution to the Stokes flow equations with a point force) near a no slip boundary by considering the image of the singularity arising from the solution to the Stokes flow equations on the

opposite side of the wall. This method requires different image singularities depending on whether the Stokeslet is parallel or normal to the wall. In Higdon (1979), the method of images was combined with slender body theory for modelling a swimmer with a spherical head and helical flagellum.

The method of images has been used to model the flow within a large variety of domains. One example of how this method has been extended is to consider the effect of multiple boundaries. For example, Liron and Mochon (1976) used the method of images to model the velocity and pressure fields for flow caused by a single point force between two parallel boundaries. In another example Dauparas and Lauga (2018) studied the leading order flows for a Stokeslet near to a corner for both the near and far field. This is found for all orientations of the force as well as all angles of the corner.

In another example, Liron and Shahar (1978) modelled the flow produced by a force singularity in a pipe. Using the method of images, they find that for all positions and orientations of a point force within the pipe the velocity components exponentially decay to zero away from the Stokeslet. The decay of the pressure fields, however, depends on the orientation of a force. A force parallel to the axis of the pipe increases the pressure difference whereas for a force perpendicular to the pipe, we see the same behaviour for the pressure field as the velocity.

1.3.4 Boundary Element Methods and Regularised Stokeslets

With the previously discussed models of microswimmers, we are unable to accurately model the swimming of non-slender bodies. To deal with more complex body shapes, the boundary element method for Stokes flows was developed. The premise of this method is to consider a distribution of the singularities in the flow across the surface of a swimmer. This is done by discretising boundary integral equations over elements of the surface. Unlike the previously discussed methods of resistive force theory and slender body theory, this has no requirement for the body to be thin and can be used for an arbitrary body shape. Therefore, it is able to capture information about a wider variety of mi-

croswimmers. However, it is more computationally expensive, due to the requirement of the solution to a 2D integral equation.

Youngren and Acrivos (1975) introduced the boundary integral method as a way of modelling a particle of arbitrary shape. This method was later extended to model multiple particles. Zick and Homsy (1982) developed the model for this to enable them to model the drag force on a periodic array of spherical particles in low Reynolds number flow.

The boundary element method was later used for modelling the motion of a flagellated microorganism (Phan-Thien et al., 1987). Phan-Thien et al. (1987) consider a swimmer with an ellipsoidal or spherical cell body and a helical flagellum. They use this to consider an efficient swimming microorganism. They find that the optimal cell body has a flat ellipsoidal shape. These results agreed with previously found experimental results.

However, the boundary element method is computationally expensive for slender bodies such as flagella (Smith et al., 2009). Therefore, an improvement on this was made by Smith et al. (2009), who looked at a hybrid method of Slender body theory and the boundary element method to model sperm cells near a surface. The idea behind this hybrid was to use the boundary element method to model the drag produced by the head of the swimmer, and use slender body theory to model the movement of the flagellum. These are then combined to describe the movement of the swimmer as a whole.

This hybrid method is a very useful tool for modelling the swimming of microswimmers. Omori and Ishikawa (2019) used this technique to model the swimming of sperm in a viscoelastic (linear Maxwell) fluid. They considered the swimming for varying levels of viscoelasticity. Characterising the viscoelastic properties using the non-dimensional Deborah number, they found that the velocity of the sperm decreased for increasing Deborah number however the efficiency was found to be independent of the level of viscoelasticity.

The previously discussed models find the solution by considering a distribution of singularities over the swimmer. However, these solutions give infinite velocity at the singularity's position (Cortez, 2001). To overcome this, the method of Regularised Stokeslets was developed first in two dimensions (Cortez, 2001) and then later in three dimensions

(Cortez et al., 2005). This method looks for solution to the Stokes flow equations with a regularised force (a smoothed force whose spread depends on the regularisation parameter denoted by ϵ) rather than a point force and will be discussed in more detail in Section 2.1.1. This is then solvable at the points of the singularities.

Regularised Stokeslets have since been widely used in the modelling of microswimmers. An important development for Regularised Stokeslets is their use within previously discussed methods of modelling swimmers. For example, Ainley et al. (2008) developed the method of images for use with Regularised Stokeslets. They test the validity of this method using the case of the drag on a sphere moving near a wall.

Regularised Stokeslets are used by Gillies et al. (2009) to model the swimming of sperm in a microscope slide chamber. This is used to consider the effects of the motion of sperm for changes of the head morphology. They find that the sperm has an increased lateral movement for a smaller head length, while increasing the width of head aids in increasing the straight line velocity of the sperm.

Another example of modelling swimmers using Regularised Stokeslets involved investigating the clustering behaviour of sperm (Ishimoto and Gaffney, 2018). This behaviour is studied for both a waterlike and linearly viscoelastic fluid. To model the collective behaviour of the sperm, Ishimoto and Gaffney (2018) used a Regularised Stokeslet distribution to represent the flow produced by each sperm and then considered the interactions between separate sperm. They found that viscoelasticity increased the amount of clustering.

In addition to biological swimmers, the method of Regularised Stokeslets has also been applied to a large array of artificial swimmers. In an example of this, Montenegro-Johnson et al. (2015) uses an extension to Regularised Stokeslets for modelling phoretic problems. Using similar methods to finding the Regularised Stokeslet, Montenegro-Johnson et al. (2015) find a regularised solution to Laplace's equation termed a Regularised Sourcelet. Using Regularised Sourcelets for finding concentration and Regularised Stokeslets for finding the velocity, they developed a method for modelling phoretic particles.

A variation of the method of Regularised Stokeslets is considered by Cortez (2018). This variation places a linear continuous distribution of regularised forces along a line segment. Using this, a flagellum can be represented by a small number of line segments rather than the large required number of Regularised Stokeslets. This was initially considered by Smith (2009).

Using Regularised Stokeslets, Smith (2018) introduced the Nearest Neighbour method for numerical models and this was further discussed in Gallagher and Smith (2018). This method used the fact that the forces vary much slower than the Regularised Stokeslets. Therefore, they proposed to use different discretisations for the forces and the Regularised Stokeslets. This was able to drastically reduce computational time for solutions. This will be discussed in more detail in Section 2.2. A large benefit to this model is that it enables the modelling of swimmers without building a mesh, which will be useful for handling the complex geometry of the swimmers that we will model in this thesis.

1.3.5 Squirmers

Many of the examples discussed have been of uniflagellate swimmers. However another large area of modelling microswimmers involves modelling multicilliates. The main examples of these that we will be looking at are usually single celled swimmers, often moving with a squirming motion. These swimmers are typically reffered to as squirmers. Squirmers are swimmers that are able to move through small deformations of their shape (Lighthill, 1952).

An initial model for the swimming of squirmers was introduced by Lighthill (1952) which looked at how a deformable spherical swimmer could move in the absence of external forces. This deformation of the sphere for a multiflagellate swimmer can represent the metachronal wave of the beating cilia over the swimmers surface (Blake, 1971b). This is done by initially considering the velocity of a point on the surface of the deforming sphere, and considering the modes of deformation that can cause movement. Lighthill (1952) then found the translational velocity of the squirmer and tested the efficiency to

find which modes of deformation produce the most efficient swimming. This model was later improved by Blake (1971b).

Since Lighthill's initial model, squirming models have been widely used to describe swimming behaviour of squirmers. A situation that has been considered is the swimming behaviour of a squirmer near to a boundary (Ishimoto and Gaffney, 2013) or another squirmer (Llopis and Pagonabarraga, 2010). This looks at the hydrodynamic interactions between two squirmers swimming in close proximity to each other. At short times, it was found that the interactions between two swimmers depend on how they are swimming together. For two squirmers swimming parallel to each other, contractile swimmers repel each other while extensile swimmers approach each other. The opposite is seen when they are swimming perpendicular to each other.

Squirming models have also been used to describe the swimming motion of multicellular algae species of *Volvox* (Pedley et al., 2016). Since *Volvox* is a spherical colony with many cells, each with two flagella, the swimming can be described similarly to that of a single celled multiflagellate swimmer using a squirmer model. Using this, they are able to model the swimming of *Volvox* for different radii of the colonies. These results are qualitatively similar to experimental results although consistently underestimates the mean swimming speed (Pedley et al., 2016).

Squirmer models offer a good approximation to the swimming behaviour for multiciliate swimmers. However they are unable to capture the details of the flagella and their interactions with each other. This clearly makes sense as an approach for Volvox due to the large number of flagella. However, for our models of multiciliate swimmers such as *Pleodorina* or *Didinium*, which we model in Chapter 4, we will study them using fully resolved flagella.

1.3.6 Bead and Spring Models

Many of the previous methods for modelling swimming behaviour can sometimes prescribe a specific gait for the flagella. However doing this can mean that the beat of the flagella

are unable to react and change due to outside circumstances. This could be the way that flagella interact with each other or when coming close to a boundary or other swimmer, as well as the effects of a fluid flow on their swimming gait. One way to model this effectively is to use a bead and spring model. Here, instead of specifying the swimming stroke of the swimmer, we instead specify the forces that drive the movement of the flagella.

Many examples of bead and spring models take inspiration from and further the simple three sphere swimmer model (Najafi and Golestanian, 2004). This is a one dimensional swimmer consisting of three spheres that are connected by rigid rods that vary in length. This swimmer is studied and expanded upon in many studies. For example, Montino and DeSimone (2015) takes the model and studies the effect of replacing one of the rods with a passive spring. A variation of the three sphere swimmer is also studied with both rods replaced with springs defining the forces that produce the motion rather than prescribing the motion itself (Pande et al., 2014).

One example of a bead and spring model that uses the three sphere model as a basis takes the three sphere model and replaces the rigid rod with springs while applying sinusoidal driving forces to the beads (Pickl et al., 2017). Here they study the swimming behaviour for this swimmer both individually as well as part of a swarm of multiple swimmers. An optimisation of a swimmer consisting of three ellipsoidal beads connected by springs is studied by Pande and Smith (2013) as well as extending the study to produce a model for a swimmer with an arbitrary bead shape.

As well as variations of simple swimmer models, bead and spring models have also been used to model biological swimmers. An example of this produces a bead and spring based model for the bacterial microswimmer, E. coli (Kong et al., 2015). Here they study their model showing good agreement with experimental observations. They study the run and tumble motion of the swimmer finding relations between the tumble angle and flagella number.

In this thesis, we will also make use of bead and spring models. In Chapter 3, we will make use of bead and spring models to study the synchronisation of flagella when not

part of a swimmer. We also use the bead and spring model in Chapter 5 to model how flagella synchronise on a full model of a swimmer.

1.3.7 Multiciliate and Multicellular Models

In recent years, there have been various studies on the swimming of multicellular and multiciliate swimmers. For example, de Maleprade et al. (2019) models the swimming of the 16 celled Gonium algal colony, studying how it steers for phototaxis. Here they model the swimming of Gonium by modelling the swimmer as a disk with forces placed around the outside of the swimmer to represent the flagella, with each flagella represented by one force. They used this model to display the swimming behaviour of Gonium, including suggesting how an imbalance in the forces can lead to a helical trajectory as seen in naturally or experimentally swimming Gonium. They are also able to relate this imbalance in forces to the pitch angle of helical trajectory.

As well as multicellular swimmers, some work has also been done towards modelling the swimming of multiciliate microswimmers that explicitly model the individual flagella. Rode et al. (2021) models the swimming dynamics of a general spherical multiciliate microswimmer with up to 60 flagella. They model the flagella of the swimmer by using 3 semiflexible polymers, with each polymer modelled as a system of beads and springs. These flagella models contain 26 beads per polymer strand and are quite large with a length of 1.375 times the radius of the body. They also study metachronal waves and show how a metachronal wave can lead to a helical trajectory.

In this thesis, we will be studying the dynamics of a wide array of eukaryotic multicellular and multicilliate organisms mainly focusing on Volvocine Green algae. We will use the Nearest neighbour method to enable us to model the swimming of these swimmers. Using this method will enable us to be able to account for the complex geometries of these swimmers.

Due to these complex geometries, many of these swimmers have either not been modelled before or have required the use of simplified geometry. For example, de Maleprade

et al. (2019) models the colony of Gonium as a disk driven by fixed point forces. The contribution of this thesis will be to analyse the swimming of such swimmers where the individual cells and flagella/cilia are fully resolved.

In this thesis we will be modelling the swimming behaviour for multicellular and multiciliate microswimmers. In Chapter 2 we discuss the underlying mathematics behind modelling the swimming of microswimmers. We also introduce some of the mathematical models that we will use throughout this thesis. In Chapter 3, we take a more in depth study into multiciliate swimmers. We will study the optimal metachronal wave as well as use a bead and spring method to model the synchronisation of flagella. In Chapter 4, we introduce the Algal Colony Suite. This is a simple to use app which can build multicellular swimmers. We then use this to produce models to study the swimming behaviour of the Volvocine green algae. We then go on to study the synchronisation of flagella on full swimmer models using bead and spring models in Chapter 5. We now go on to introduce some of the underlying mathematics and important models for this thesis.

CHAPTER 2

MATHEMATICAL METHODS FOR MODELLING MICROSWIMMERS

2.1 Low Reynolds Number Flows

Throughout this thesis, we will model swimmers in water-like fluids, for which the pressure and flow field can be determined using the Navier-Stokes equations (Batchelor, 2000). These fluids are known as Newtonian fluids. These are fluids for which their viscosity is unaffected by the shear rate when all other factors remain the same. With an added force term $\boldsymbol{f}$, the Navier-Stokes equations are given as

$$\left(\frac{\partial}{\partial t} + \boldsymbol{u}\cdot\nabla\right)\boldsymbol{u} = -\frac{\nabla p}{\rho} + \nu\nabla^2\boldsymbol{u} + \frac{\boldsymbol{f}}{\rho}, \qquad \frac{\partial\rho}{\partial t} + \nabla\cdot(\rho\boldsymbol{u}) = 0, \tag{2.1}$$

where in equations (2.1), $\boldsymbol{u}$ is the flow velocity, p is the pressure, ρ is the fluid density and ν is the kinematic viscosity. For constant density ρ, the mass continuity equation can be written as the incompressibility condition given by $\nabla\cdot\boldsymbol{u} = 0$.

The equations (2.1) can be nondimensionalised by re-scaling the variables. To do this, re-scale the length with respect to a characteristic length scale L, and the velocity with respect to a typical flow velocity, U. The time is then re-scaled with respect to the characteristic time scale given by $\tau = L/U$. The pressure is re-scaled by some P_0 that can be chosen to coincide with either the inertial or viscous scaling. Substituting these

into equation (2.1) and denoting nondimensional variables with a *, gives

$$\frac{\rho U^2}{L}\left(\frac{\partial}{\partial t^*} + \boldsymbol{u^*}.\nabla\right)\boldsymbol{u^*} = -\frac{P_0}{L}\nabla p^* + \frac{\mu U}{L^2}\nabla^2 u^* + \boldsymbol{f}, \tag{2.2}$$

where μ is the dynamic viscosity with $\nu = \mu/\rho$. Choosing the viscous pressure scale $P_0 = \frac{\mu U}{L}$ and rearranging equation (2.2) gives the nondimensional equations. Dropping the *s gives

$$Re\left(\frac{\partial}{\partial t} + \boldsymbol{u}.\nabla\right)\boldsymbol{u} = -\nabla p + \nabla^2\boldsymbol{u} + \boldsymbol{F}, \tag{2.3}$$

where $Re = \frac{\rho UL}{\mu}$ is the Reynolds number and $\boldsymbol{F} = \frac{L^2}{\mu U}\boldsymbol{f}$ is the non-dimensional force.

When the Reynolds number is small, it can be seen from equation (2.3) that the nondimensional equations can be simplified to

$$-\nabla p + \nabla^2\boldsymbol{u} + \boldsymbol{F} = \boldsymbol{0}, \quad \nabla\cdot\boldsymbol{u} = 0. \tag{2.4}$$

These equations are known as the Stokes equations, which are used to describe low Reynolds number flows. It is easy to see that these equations are simpler to work with than the full Navier-Stokes equations. The main reason for this is that the equations are now linear, vastly simplifying the system.

Using the linearity of the system, the Stokes equations for a flow caused by a point force at $\boldsymbol{x'}$, replacing the force term with that of a point force as $\delta(\boldsymbol{x}-\boldsymbol{x'})\boldsymbol{F}$ (where $\delta(\boldsymbol{x}-\boldsymbol{x'})$ is the Dirac delta distribution), are able to be solved. This is done using Greens functions (Lauga and Powers, 2009) which have been given the name of Oseen tensors, or Stokeslets. The flow produced by a point force is given by

$$\boldsymbol{u}(\boldsymbol{x}) = G(\boldsymbol{x}-\boldsymbol{x'})\cdot\boldsymbol{F},$$

where G is the Stokeslet. In component form, this tensor is given by

$$G_{ij}(\boldsymbol{r}) = \frac{1}{8\pi}\left(\frac{\delta_{ij}}{r} + \frac{r_i r_j}{r^3}\right), \tag{2.5}$$

where $r = |\boldsymbol{r}|$ with $\boldsymbol{r} = \boldsymbol{x} - \boldsymbol{x'}$ and δ_{ij} is the Kronecker delta.

To complete the solution to the Stokes equations for a flow produced by a point force, we require an expression for the pressure. The pressure is given by

$$p(\boldsymbol{x}) = \Pi(\boldsymbol{x} - \boldsymbol{x'}) \cdot \boldsymbol{F},$$

where in component form, Π is given by

$$\Pi_i(\boldsymbol{r}) = \frac{r_i}{4\pi r^3}. \tag{2.6}$$

From these expressions for the pressure and velocity we can find an expression for the stress. The stress can be found using a combination of the velocity and pressure and is given by

$$\sigma(\boldsymbol{x}) = -p\boldsymbol{I} + (\nabla \boldsymbol{u} + \nabla \boldsymbol{u}^T) = T \cdot \boldsymbol{F},$$

where T is the associated stress tensor In component form, this is given by

$$T_{ijk}(\boldsymbol{r}) = -\frac{1}{8\pi}\frac{6r_i r_j r_k}{r^5}. \tag{2.7}$$

Another important solution to the Stokes equations is for the Stokes flow produced by a point source located at the origin (Zhao et al., 2019). For a source of strength q, the flow is given by

$$\boldsymbol{u}(\boldsymbol{r}) = \frac{\boldsymbol{r}}{4\pi r^3} q. \tag{2.8}$$

For a negative value of q, equation (2.8) models the flow produce by a point sink.

We can obtain higher order singularity solutions by taking linear combinations of the Stokeslet and point source. One important example of this involves taking an equal strength point source and sink in the same location (Zhao et al., 2019). This produces

the source dipole for which the flow tensor is given by

$$D(\boldsymbol{r}) = \frac{r^2 I - 3\boldsymbol{r}\boldsymbol{r}}{8\pi r^5}. \tag{2.9}$$

The source dipole can also be found through taking two derivatives of the Stokeslet (Lauga and Powers, 2009).

We can also use the Stokeslets solution to solve for fluid flows caused by multiple point forces. This can be simply achieved by using multiple Stokeslets at the positions of the point forces. The solution for the flow is found by simply summing over the Stokeslets for the different forces.

To be able to solve for the swimming of a microswimmer we can use the Boundary Integral Method to find its velocity (Smith, 2018). This involves integrating the Stokeslet solution for a point force over the boundary of the swimmer giving the single layer potential, as well as another term involving the stress as given in equation (2.7) of the fluid giving the double layer potential (Pozrikidis, 1992). This gives the Boundary Integral equation as

$$\lambda u_j(\boldsymbol{x}) = -\iint_{\partial D} G_{ij}(\boldsymbol{x}, \boldsymbol{x'}) f_i(\boldsymbol{x'}) dS(\boldsymbol{x'}) + \iint_{\partial D} u_i(\boldsymbol{x'}) T_{ijk}(\boldsymbol{x}, \boldsymbol{x'}) n_k(\boldsymbol{x'}) dS(\boldsymbol{x'}), \tag{2.10}$$

where G_{ij} is the Stokeslet as given in equation (2.5), f_i are forces from the swimmer acting on the fluid, n_k represents the kth component of the outward pointing normal and $\lambda = 1/2$ if $\boldsymbol{x}$ is located on the boundary of the swimmer or $\lambda = 1$ otherwise.

The double layer potential represented by the integral of the stress for the flow solution can be used to represent flows containing sources and sinks as well as flows created by swimmers expanding and contracting flexible bodies to move (Pozrikidis, 1992). However, if the boundary of the domain is stationary and the swimmers have a rigid body, then the double layer potential integral can be eliminated (Smith, 2018). Therefore, with these sets of conditions, the flow is given by just the integral of the Stokeslets over the boundary of the swimmer.

2.1.1 Regularised Stokeslets

The Stokeslets that are the solutions to the general Stokes flow equations with a point force acting on the fluid are singular. These singularities can cause difficulties in finding numerical solutions. To solve this, the method of Regularised Stokeslets is used, as introduced by (Cortez, 2001) for 2 dimensions which was later extended to 3 dimensions (Cortez et al., 2005).

Introducing this regularised force, the nondimensional Stokes equations become

$$\nabla^2 \boldsymbol{u} - \nabla p = \phi_\epsilon(\boldsymbol{x} - \boldsymbol{x'})\boldsymbol{F}, \tag{2.11}$$

where ϕ_ϵ is a regularisation function and $\boldsymbol{F}$ are the forces acting on the fluid. The regularisation function is a smooth approximation to the Dirac delta distribution. Different versions of this function are considered in Cortez (2001). Here, the choice of regularisation function will be the same as that chosen in Cortez et al. (2005). This is given by

$$\phi_\epsilon(\boldsymbol{x} - \boldsymbol{x'}) = \frac{15\epsilon^4}{8\pi(r^2 + \epsilon^2)^{7/2}}, \tag{2.12}$$

where $r = |\boldsymbol{x} - \boldsymbol{x'}|$ and ϵ is the regularisation parameter. The exponent in the denominator of equation (2.12) controls the decay rate of the function as $|\boldsymbol{x}| \to \infty$. By considering the regularisation error, Cortez et al. (2005) showed that the denominator is required to behave asymptotically as r^m with $m > 5$. This specific form was chosen for convenience and is now the widely used form. This regularisation function is radially symmetric and has the property that

$$\int \phi_\epsilon(\boldsymbol{x}) d\boldsymbol{x} = 1.$$

Also,

$$\int f(\boldsymbol{x})\phi_\epsilon(\boldsymbol{x_0}) d\boldsymbol{x} \to f(\boldsymbol{x_0})$$

for $\epsilon \to 0$. Therefore, for $\epsilon \to 0$, we have that

$$\phi_\epsilon(\boldsymbol{x} - \boldsymbol{x'}) \to \delta(\boldsymbol{x} - \boldsymbol{x'}),$$

where $\delta(\boldsymbol{x} - \boldsymbol{x'})$ is the Dirac delta distribution. The regularisation parameter ϵ determines the spread of the distribution.

This particular choice of regularisation function $\phi(\boldsymbol{x} - \boldsymbol{x'})$, gives the solution to the velocity as

$$u_i = S_{ij}^\epsilon F_j, \tag{2.13}$$

where S_{ij}^ϵ represents the component form of the Regularised Stokeslet given by

$$S_{ij}^\epsilon(\boldsymbol{x}, \boldsymbol{x'}) = \frac{\delta_{ij}(r^2 + 2\epsilon^2) + r_i r_j}{(r^2 + \epsilon^2)^{3/2}}. \tag{2.14}$$

As with the regularisation function, taking $\epsilon \to 0$ recovers the singular form of the Stokeslet described previously in equation (2.5).

A useful extension to the method of Regularised Stokeslets is to use them to model the flow produced by a moving body. This can be done using the Boundary Integral method as described earlier. Using this, we describe the flow using the single layer potential over the body. For the Regularised Stokeslet, the velocity is approximated by

$$u_j(\boldsymbol{x}) \approx \frac{-1}{8\pi} \iint_{\partial D} S_{ij}^\epsilon(\boldsymbol{x}, \boldsymbol{y}) f_i(\boldsymbol{y}) dS(\boldsymbol{y}). \tag{2.15}$$

For solving this numerically, we need to discretise our solution to the velocity. As in Cortez et al. (2005), we can discretise our solution by placing N Stokeslets over the surface of the body allowing us to approximate the velocity at a general position $\boldsymbol{x}_0$ by

$$u_j(\boldsymbol{x_0}) \approx \frac{1}{8\pi} \sum_{n=1}^{N} \sum_{i=1}^{3} S_{ij}^\epsilon(\boldsymbol{x}_n, \boldsymbol{x}_0) g_i(\boldsymbol{x}_n) A(\boldsymbol{x}_n), \tag{2.16}$$

where $g(\boldsymbol{x}_n) = -f(\boldsymbol{x}_n)$ represents the force on the fluid at the position $\boldsymbol{x}_n$ and $A(\boldsymbol{x}_n)$ is

the quadrature weight. For a body moving through fluid, the velocity at the surface of the body is typically known and we need to find the force. Therefore, for N Stokeslets over the body, we have $3N$ scalar unknowns for the components of the forces. We set N collocation points over the surface of the body typically in the same position as the Stokeslet position. Using the known values for the velocity on the surface at these collocation points, we can evaluate equation (2.16) at the collocation points to calculate the unknown forces. Once the forces are known, they can then be used for calculating the velocity at a general location.

For our previous discretisation, there is one unknown force for each Stokeslet. However, we note that the forces vary much slower than the Regularised Stokeslets. To take advantage of this we can split the boundary of the swimmer into $M < N$ elements with a constant force over each element. For a flow produced by a filament, we use line elements and a 3D body is split into surface elements. Using this, the velocity can be found with the equation

$$u_i(\boldsymbol{x}) = \sum_{m=1}^{M} f_j^m \iint_{E(m)} S_{ij}^{\epsilon}(\boldsymbol{x}, \boldsymbol{y^m}) dS, \tag{2.17}$$

for the flow produced by a moving 3D surface, where f_j^m is the jth component of the force per unit area over the mth surface element, $E(m)$. For for the flow produced by a 1D filament, we use a modification of equation (2.17), where we instead take a line integral of the Stokeslets over each line element. For the case of the filament, f_j^m represents the force per unit length. However, splitting the surface into different elements does require building a mesh of the surface. This adds a large amount of complexity to the problem, as we require information about the connectivity of the element and creating these meshes is often computationally difficult.

When considering the motion of a microswimmer, the velocity of the swimmer is not necessarily known and adds to the unknowns of the problem. This is known as the free swimming problem. In this problem, as well as the forces as unknowns, there are also the translational velocity U, and angular velocity Ω. With a discretisation of N vector

degrees of freedom, there are now $3N + 6$ unknowns.

To model the swimming of this swimmer, as well as the usual Boundary Integral Equation (2.15), the equations for force balance and moment balance are also required. Therefore, the free swimming problem can be formulated as

$$u_j(\boldsymbol{x}) = \frac{-1}{8\pi} \iint_{\partial D} S_{ij}^{\epsilon}(\boldsymbol{x}, \boldsymbol{X}) f_i(\boldsymbol{X}) dS_{\boldsymbol{X}}, \tag{2.18a}$$

$$\iint_{\partial D} f_i(\boldsymbol{X}) dS_{\boldsymbol{X}} = 0, \tag{2.18b}$$

$$\iint_{\partial D} \epsilon_{ijk} X_k f_j(\boldsymbol{X}) dS_{\boldsymbol{X}} = 0. \tag{2.18c}$$

However for our problem, we will consider the swimmer to be in the body frame (Gallagher and Smith, 2018). This is the reference frame in which the body of the swimmer is stationary. We denote the coordinates in this body frame by $\boldsymbol{\xi}$ and the basis vectors for the frame are given in a matrix $\boldsymbol{B}$ by $\boldsymbol{B} = (\boldsymbol{b}^{(1)}|\boldsymbol{b}^{(2)}|\boldsymbol{b}^{(3)})$. Denoting the origin of the new coordinate system by $\boldsymbol{x}_0$, we modify the usual coordinates to get them in terms of the new coordinates of the body frame $\boldsymbol{\xi}$. The transformation is then

$$\boldsymbol{x} = \boldsymbol{x}_0 + \boldsymbol{B} \cdot \boldsymbol{\xi}.$$

We can then see by differentiating using the chain rule, we can get the transformation for the velocity given by

$$\dot{\boldsymbol{x}} = \dot{\boldsymbol{x}}_0 + \dot{\boldsymbol{B}} \cdot \boldsymbol{\xi} + \boldsymbol{B} \cdot \dot{\boldsymbol{\xi}}.$$

We can rewrite the above expression in terms of the rigid body velocity $\boldsymbol{U}$ and the body's angular velocity $\boldsymbol{\Omega}$ (Gallagher and Smith, 2018). In doing this we obtain the transformation of the velocity as

$$\dot{\boldsymbol{x}} = \boldsymbol{U} + \boldsymbol{\Omega} \times (\boldsymbol{x} - \boldsymbol{x}_0) + \boldsymbol{B} \cdot \dot{\boldsymbol{\xi}}.$$

Letting $\boldsymbol{u}(\boldsymbol{x}) = \dot{\boldsymbol{x}}$ on the surface of the swimmer ∂D, equation (2.15) can be rewritten in terms of our new reference frame as

$$-U_i - \epsilon_{ijk}\Omega_j(x_k - x_{0k}) - \frac{1}{8\pi}\iint_{\partial D} S_{ij}^{\epsilon}(\boldsymbol{x}, \boldsymbol{X}) f_j(\boldsymbol{X}) dS_{\boldsymbol{X}} = B_{ij}\dot{\xi}_j, \quad \forall \boldsymbol{x} \in \partial D. \tag{2.19}$$

The equations for the force and moment balance stay the same.

In a typical problem when setting up the body frame, the origin, $\boldsymbol{x}_0$, and orientation, $\boldsymbol{B}$ of the swimmer will be known. For the coordinates in the new frame for the surface of the swimmer, $\boldsymbol{\xi}$, giving the swimmer shape and also the motion in the body frame given by $\dot{\boldsymbol{\xi}}$, these will be determined by the mathematical model representing the swimmer. Therefore the unknowns of the equations that we are trying to find are then given by forces on the surface, $f(\boldsymbol{x})$ for $\boldsymbol{x} \in D$, the translational velocity $\boldsymbol{U}$ and the angular velocity $\boldsymbol{\Omega}$.

Another important solution for Stokes flow to study is the Blakelet. This is the tensor that forms the solution to the Stokes flow produced by a point force near a planar boundary found using the method of images (Blake, 1971a). Considering a boundary as an infinite plane at $x_3 = 0$, for a singularity located at $\boldsymbol{\xi} = [\xi_1, \xi_2, h]$, we consider an image outside the flow domain at the point $\boldsymbol{\xi^*} = \boldsymbol{[\xi_1, \xi_2, -h]}$. The form of this image is found by Blake (1971a) using a two dimensional Fourier transform. The solution is then given by

$$\begin{aligned} u_j(x) &= F_k G_{jk}(\boldsymbol{x}, \boldsymbol{\xi}) \\ &= \frac{F_k}{8\pi\mu}\Bigg[\left\{\frac{\delta_{jk}}{r} + \frac{r_j r_k}{r^3}\right\} - \left\{\frac{\delta_{jk}}{R} + \frac{R_j R_k}{R^3}\right\} \\ &\quad + 2h\left(\delta_{k\alpha}\delta_{\alpha l} - \delta_{k3}\delta_{3l}\right)\frac{\partial}{\partial R_l}\left\{\frac{hR_j}{R^3} - \left(\frac{\delta_{j3}}{R} + \frac{R_j R_3}{R^3}\right)\right\}\Bigg], \end{aligned} \tag{2.20}$$

where $\alpha = 1$ or 2, F_k is a point force in the $k-$direction and r and R are given by

$$\begin{aligned} r &= \left[(x_1 - \xi_1)^2 + (x_2 - \xi_2)^2 + (x_3 - h)^2\right]^{1/2} \\ \text{and} \quad R &= \left[(x_1 - \xi_1)^2 + (x_2 - \xi_2)^2 + (x_3 + h)^2\right]^{1/2}. \end{aligned} \tag{2.21}$$

To use the Blakelets in numerical methods as we will during this thesis, we need

to account for singularities that are present by using a regularised force as with the Regularised Stokeslets. The Regularised Blakelet, originally introduced in Ainley et al. (2008) and further developed in Smith (2009) is given by

$$\begin{aligned} B_{ij}^{\epsilon}(\boldsymbol{x},\boldsymbol{\xi}) = & \frac{\delta_{ij}\left(r^2+2\epsilon^2\right)+r_i r_j}{r_\epsilon^3} - \frac{\delta_{ij}\left(R^2+2\epsilon^2\right)+R_i R_j}{R_\epsilon^3} \\ & + 2h\Delta_{jk}\left[\frac{\partial}{\partial R_k}\left(\frac{hR_i}{R_\epsilon^3} - \frac{\delta_{i3}\left(R^2+2\epsilon^2\right)+R_i R_3}{R_{\epsilon^3}}\right) - 4\pi h\delta_{ik}\phi_\epsilon(R)\right] \\ & - \frac{6h\epsilon^2}{R_\epsilon^5}\left(\delta_{i3}R_j - \delta_{ij}R_3\right), \end{aligned} \tag{2.22}$$

where Δ_{jk} has the value of $+1$ for $j=k=1,2$,has value -1 for $j=k=3$ and 0 otherwise.

2.2 Nearest Neighbour Method

As with an element based approach the Nearest Neighbour Method decouples the force from the quadrature, taking advantage of the fact that the forces vary much more slowly than the Regularised Stokeslets in the the kernel of the integral in equation (2.15). However unlike the Boundary Element Method, the Nearest Neighbour method has the added benefit of not being required to produce a mesh, further improving the computational efficiency and ease of use.

To take advantage of the slower varying forces, the Nearest Neighbour method uses two discretisations. One that is coarse to describe the slowly varying forces, which we will call the force discretisation which we will denote by $\{\boldsymbol{x}[1],\ldots,\boldsymbol{x}[N]\}$. The other will be fine to describe the rapidly varying Regularised Stokeslets, which we will call the quadrature discretisation, which will be denoted by $\{\boldsymbol{X}[1],\ldots,\boldsymbol{X}[Q]\}$.

With these two dicretisations, we can create the nearest neighbour matrix to compare the two. For each quadrature point, we wish to find the closest force point to it. This information is then put into the nearest neighbour matrix ν. This is given by

$$\nu[q,n] = \begin{cases} 1 & \text{if } n = \underset{\hat{n}=1\ldots N}{\operatorname{argmin}} |\boldsymbol{x}[\hat{n}] - \boldsymbol{X}[q]| \\ 0 & \text{otherwise.} \end{cases} \tag{2.23}$$

As expected, we can see that if we were to use the same discretisation for the force and quadrature points, the nearest neighbour matrix ν would be the identity matrix and would therefore not change anything reducing the system to the standard Nyström method of Regularised Stokeslets.

We can then use the nearest neighbour matrix to discretise the forces such that

$$-F_i(\boldsymbol{X}[q])dS(X[q]) = \sum_{n=1}^{N} \nu[q,n] g_i[n] dS(x[n]). \tag{2.24}$$

This representation of the forces can now be used in solving the swimming problem with the boundary integral equations. We discretise the integrals using a quadrature method using Q quadrature points. Using the quadrature discretisation for the integrals with the Nearest dicretisation for the forces, gives our discretised equations as

$$\frac{1}{8\pi} \sum_{n=1}^{N} g_j[n] dS(x[n]) \sum_{q=1}^{Q} S_{ij}^{\epsilon}(\boldsymbol{x}[m], \boldsymbol{X}[q]) \nu[q,n] - U_i - \epsilon_{ijk}\Omega_j(x_k[m] - x_{0k}) = B_{ij}\dot{\xi}_j[m], \quad \text{for } m = 1, \ldots, N, \tag{2.25a}$$

$$\sum_{n=1}^{N} g_j[n] dS(\boldsymbol{x}[n]) \sum_{q=1}^{Q} \delta_{ij} \nu[q,n] = 0, \tag{2.25b}$$

$$\sum_{n=1}^{N} g_j[n] dS(\boldsymbol{x}[n]) \sum_{q=1}^{Q} \epsilon_{ijk} X_k[q] \nu[q,n] = 0. \tag{2.25c}$$

We now have $3N+6$ linear equations for $3N+6$ unknowns, which we can solve numerically to get U, Ω and $g_i[n]$. Defining $F_j[n] = g_j[n]dS(x[n])$, these equations can be expressed as a matrix in block form as

$$\begin{pmatrix} A_{11}^S & A_{12}^S & A_{13}^S & A_1^U & A_1^\Omega \\ A_{21}^S & A_{22}^S & A_{23}^S & A_2^U & A_2^\Omega \\ A_{31}^S & A_{32}^S & A_{33}^S & A_3^U & A_3^\Omega \\ A_1^F & A_2^F & A_3^F & 0 & 0 \\ A_1^M & A_2^M & A_3^M & 0 & 0 \end{pmatrix} \begin{pmatrix} F_1[1] \\ \vdots \\ F_1[N] \\ F_2[1] \\ \vdots \\ F_2[N] \\ F_3[1] \\ \vdots \\ F_3[N] \\ \boldsymbol{U} \\ \boldsymbol{\Omega} \end{pmatrix} = \begin{pmatrix} B_{1,j}\dot{\xi}_j[1] \\ \vdots \\ B_{1,j}\dot{\xi}_j[N] \\ B_{2,j}\dot{\xi}_j[1] \\ \vdots \\ B_{2,j}\dot{\xi}_j[N] \\ B_{3,j}\dot{\xi}_j[1] \\ \vdots \\ B_{3,j}\dot{\xi}_j[N] \\ \boldsymbol{0} \\ \boldsymbol{0} \end{pmatrix}. \tag{2.26}$$

In the matrix equation above, the blocks of the matrix are expressed by

$$A_{ij}^S\{m,n\} = \frac{1}{8\pi}\sum_{q=1}^{Q} S_{ij}^\epsilon(\boldsymbol{x}[m], \boldsymbol{X}[q])\nu[q,n] \quad \text{for } m,n = 1,\ldots,N, \tag{2.27a}$$

$$A_i^U\{m,j\} = -\delta_{i,j} \quad \text{for } m = 1,\ldots,N, \tag{2.27b}$$

$$A_i^\Omega\{m,j\} = -\epsilon_{ijk}(x_k[m] - x_{0k}) \quad \text{for } m = 1,\ldots,N, \tag{2.27c}$$

$$A_j^F\{i,n\} = \delta_{ij}\sum_{q=1}^{Q}\nu[q,n] \quad \text{for } n = 1,\ldots,N, \tag{2.27d}$$

$$A_j^M\{i,n\} = \epsilon_{ijk}X_k\sum_{q=1}^{Q}\nu[q,n] \quad \text{for } n = 1,\ldots,N. \tag{2.27e}$$

A challenge when using this method comes from creating the nearest neighbour matrix for a swimmer with flagella. When creating the matrix ν, it is possible that the closest force point to a quadrature point in the flagellum could be placed in the body of the swimmer. This can cause errors in solving for the swimming. To deal with this, we need to create the nearest neighbour matrices for the body and flagella of the swimmer separately. This is also required for a boundary in case the swimmer gets too close to

the boundary. The Nearest Neighbour Method is the method that we will be using to calculate the swimming behaviour of our modelled swimmers throughout Chapter 4 for our models of the swimming behaviour of the Volvocine green algae as well as the single celled swimmer *Didinium*.

2.3 Level Sets for Swimmer Geometries

To be able to use the Nearest Neighbour Regularised Stokeslet method, we require a way of discretising the swimmers. For the body of the swimmers we will use a level set approach. For a function $f(x_1, \ldots, x_n)$ its level set is a set for which $f(x_1, \ldots x_n) = c$ for some constant c. If we have f as a function of 3 variables (n=3), the level sets are known as isosurfaces. Therefore the level set for a 3-D function gives a set of points that discretise a surface for which the above statement is satisfied.

Level sets can be used to form a set of points to discretise a surface. Since the Nearest Neighbour method only requires a set of points rather than a full mesh describing connectivity, this level set discretisation can be used for the Nearest Neighbour method with less computational complexity than producing a full mesh. Therefore, to discretise our swimmers, we will use level sets.

One example of the type of swimmers we will model in this thesis are Volvocine green algal colonies. These range from the single celled Chlamydomonas to the largely multicellular Volvox. Each member of the Volvocine green algae is made up of ellipsoidal cells. Therefore, to model the surface of an algal colony, we consider them as a group of individual ellipsoidal cells. To model this using level sets, we can take the level set representing each ellipsoidal cell and sum the functions used to produce the level sets of the individual cells together. We then take the level set of this function to produce our discretisation of the full body of the swimmer. This will give the discretisation for the surface of a colony of algal cells.

For a single ellipsoidal cell, we can model this using the level set of a modified Gaus-

sian function. An unmodified Gaussian would produce a spherical cell. Therefore, an ellipsoidal cell is given by a level set of the function

$$f_{LS} = \exp\left(\frac{-r'^2}{B}\right) \tag{2.28}$$

where B controls the decay rate of the Gaussian function giving a larger decay for smaller values of B. The variable r' represents the semiaxes of the cell given by $r'^2 = y_1'^2 + y_2'^2 + y_3'^2$. Here, y_1', y_2' and y_3' are the modified coordinates to account for the rotation and semiaxes lengths of the cell. These are given by

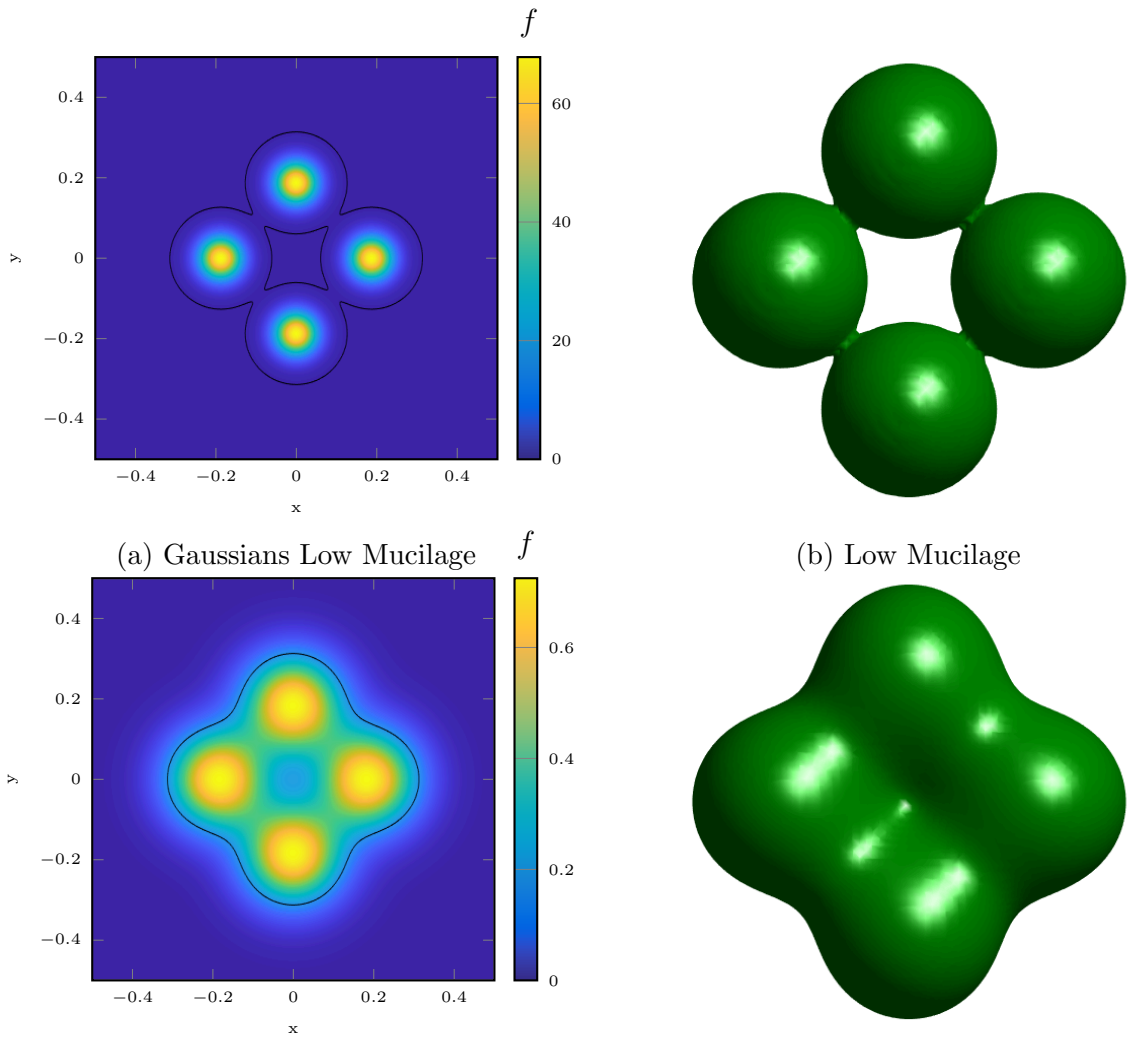
$$y_1' = \frac{(y_1 - cc(1))\cos\theta + (y_2 - cc(2))\sin\theta}{y_{1_r}}, \tag{2.29a}$$

$$y_2' = \frac{(y_1 - cc(1))\sin\theta + (y_2 - cc(2))\cos\theta}{y_{2_r}}, \tag{2.29b}$$

$$y_3' = \frac{y_3 - cc(3)}{y_{3_r}}. \tag{2.29c}$$

where cc is the centre of the cell, θ is the azimuthal angle of rotation of the cell and y_{1_r}, y_{2_r} and y_{3_r} are the y_1, y_2 and y_3 semiaxes respectively. To build the level set of a non spherical algal colony we sum together the level sets for the individual cells.

The multicellular Volvocine green algae have varying levels of mucilage between the cells. To account for this, we wish to find level sets to model the swimmer that have different decay rates but equal radius. In Panels (a) and (c) of Figure 2.1 we show a 2-D example of two sums of Gaussian functions with different decay rates. It is clear from this that we can produce cells with the same radius but different amounts of mucilage between the cells. We also note that for the radius to be equal at the given level, we require the amplitude of the Gaussian to vary, with in this instance the low mucilage case requiring a much higher amplitude than the high mucilage case. We use a similar method in 3-D to find a level set that gives ellipsoids with the same radius but different decay rates. Since we do not change the level of level set, we modify the amplitude of the Gaussian so the level set has the correct radius and the required decay rate.



(a) Gaussians Low Mucilage

(b) Low Mucilage

(c) Gaussians High Mucilage

(d) High Mucilage.

Figure 2.1: Figure displaying the level sets from adding 4 Gaussians to model *Tetrabaena*. Panels (a) and (b) show the level set of Gaussians for a low amount of mucilage. Panel (a) shows this for a 2D Gaussian where as Panel (b) gives the level set surface from a 3D Gaussian. Panels (c) and (d) give the 2D and 3D (respectively) level sets for the model of *Tetrabaena* with a high level of Mucilage. For the 2D cases in Panels (a) and (c) we have the colour map showing the value of the function and the line showing the desired level set.

To calculate the required amplitude, we consider two level sets given by

$$\exp\left(\frac{-r^2}{B_1}\right) = A_2 \exp\left(\frac{-r^2}{B_2}\right) = c, \tag{2.30}$$

where c is the constant level of the level set and $B_1 = \frac{1}{8\log(2)}$. Here, $8\log(2)$ is chosen somewhat arbitrarily as the square of the full width at half maximum of a Gaussian function representing the probability density function of the normal distribution with a standard deviation of 1. B_2 is given as an input as the desired decay rate of the level set and A_2 is the amplitude to be found. To ensure that the radius remains constant, we denote $r = r'_c$ where r'_c is a constant value that represents the desired radius of the level set for a given value of c. To find A_2 we can rearrange the above equation to give

$$A_2 = \exp\left(-r'^2_c\left(\frac{1}{B_1} - \frac{1}{B_2}\right)\right).$$

The above expression for A_2 still required us to find the value of r'_c. This can be found by considering

$$\exp\left(\frac{-r'^2_c}{B_1}\right) = c \tag{2.31}$$

Solving for r'_c, gives

$$r'_c = \sqrt{-B_1 \log(c)}.$$

Therefore, the Gaussian to model a single cell is given by

$$f_{LS} = A_2 \exp\left(\frac{-(r'^2)}{B_2}\right), \tag{2.32}$$

In Figure 2.1 we show a level set discretisation for *Tetrabaena* with different decay rates for the Gaussians functions for their cells. Here we see that this leads to a difference in the amount that is discretised between the cells. As desired, this allows us to model different amount of mucilage between cells in Algal Colonies.

To model the full multicellular swimmer, we can take a sum of the Gaussians used

to represent a single cell in equation (2.32) with different centre positions and rotation angles and choosing the desired decay rate B_2. This will give a full surface of connected ellipsoidal cells. Crucially, these cell bodies will be the same radius irrespective of the decay function, but the amount of mucilage, will vary as shown in Figure 2.1. The equation to model a full multicellular swimmer is given by

$$f_{MC} = \sum_{i=1}^{N_{cell}} \exp\left(\frac{-r_i'^2}{B_2}\right), \tag{2.33}$$

where N_{cell} is the number of cells in the multicellular swimmer.

We can then use this as part of the Nearest Neighbour method to solve for their swimming behaviour. We make use of this form of the level set method as part of building our app, the Algal Colony Suite in Section 4.2 as well as for modelling the Volvocine green algae for which we present results in Section 4.4

Another type of body that we can create using the level set method is a body created via extruding from a centreline. This can be done with a varying radius along the centreline of swimmer. To use the level set method in this way, we first need to model the centreline of the swimmer. We parameterise this centreline in terms of the arclength s, giving the cartesian coordinates of the centreline as functions of s given by $y_1(s)$, $y_2(s)$ and $y_3(s)$. The exact form of these equations will vary depending on the shape of the swimmer that is being modelled.

To account for a potential varying radius along the swimmer, the radius also needs to be parametrised. Therefore the radius is expressed as a function of the arclength given as $y_{1r}(s)$, $y_{2r}(s)$ and $y_{3r}(s)$. We then discretise the centreline for a large number of points. Whereas for the multicellular level set model we took the Gaussians and summed them over the centre points of the cells, for the centre line we instead take the line integral of the Gaussian over the centre line

$$f_{CL} = \int_0^L \exp\left(\frac{-r'(s)^2}{B_1}\right) ds, \tag{2.34}$$

where c is the curve that represents the centreline. Here $r'(s)^2 = y_1'(s)^2 + y_2'(s)^2 + y_3'(s)^2$ with $y_1'(s)$, $y_2'(s)$ and $y_3'(s)$ are similar to before but are centred at arclength s and the semiaxes are functions of s. In this thesis, we will use the centre line method of Level Sets shown in equation (2.34) to discretise the body of the swimmer Didinium in Section 4.5. Using both of the ellipsoidal cell and centreline level set methods, we are able to discretise a large number of swimmer bodies with complex geometrical shapes.

2.4 Flagella Waveforms

As well as the discretisation of the body, to model the swimming behaviour of the Volvocine green algae, we need to be able to model their flagella and describe their waveform. Volvocine Green Algae each have two flagella per cell all with similar wave forms moving using a sweeping motion. Therefore, we have used two similar models to describe the flagella beat.

The first of these is taken from Gallagher and Smith (2018), where it was used as a basic model to test the Nearest Neighbour method for *Chlamydomonas*. We model the flagella with respect to the arc length s. Then the tangent angle representing the flagellum (Gallagher and Smith, 2018) is then given by

$$\psi(s,t) = \psi_0(s) - \psi_1(s)\cos(t + \phi(s)), \tag{2.35}$$

with

$$\psi_0(s) = -2.5s, \quad \psi_1(s) = 0.7 + 0.15\sin(2\pi s), \quad \phi(s) = -2\pi s.$$

This waveform can be seen in Figure 2.2. The waveform in Equation (2.35) will be used in this thesis to model the flagella of *Chlamydomonas* in Section 4.4.1.

The second model for the flagella we will use is found from fitting a model of a waveform to experimental data which was collected by Kirsty Wan. This experimental data was given to me as an array of points for a beating *Volvox* flagellum over a period of time.

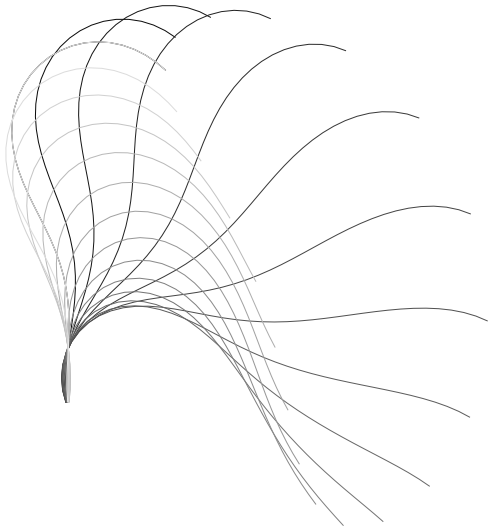
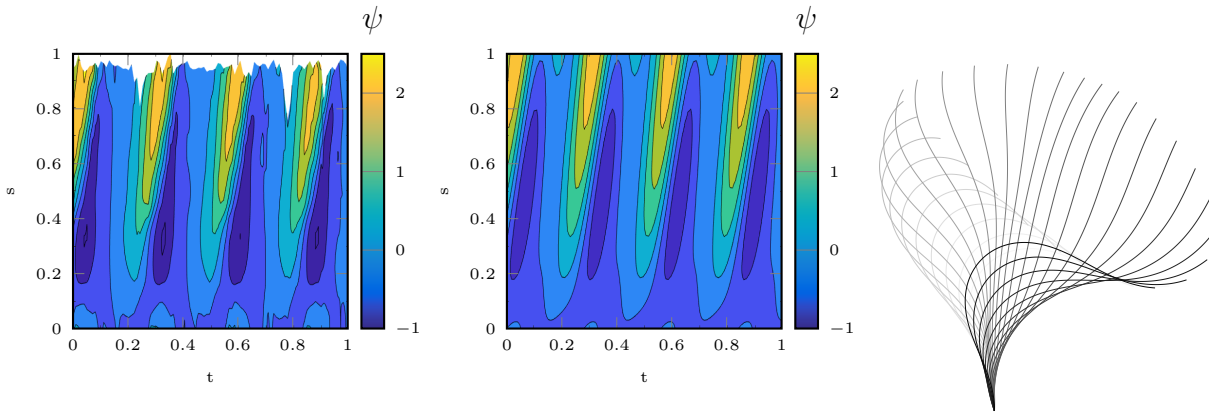


Figure 2.2: Figure showing the flagella waveform model for *Chlamydomonas* taken from Gallagher and Smith (2018).

We need to find a model to represent the beating of this flagellum as represented in this data.

As with the previous waveform, we wish to model the flagellum by its tangent angle ψ. To do this we first need to find how the tangent angle of the experimental flagellum varies. This tangent angle will be described in terms of the arclength s. Therefore we need to use the experimental data to calculate the arclength for the experimental waveform. To find the arc length at each point, we calculate the distance between the first two points of the flagella for each time step of the data. We then do this consecutively for the rest of the data points and take the cumulative sum of these values giving us the arclength s for the flagella given by the experimental data. We can then calculate the tangent angle by numerically differentiating the x and y values of the points on the flagella given by the data in terms of the arc length s. The tangent angle that we calculate for our data is presented in Panel (a) of Figure 2.3.

We then wish to find a function for a waveform to model this data. This can be found by considering a Fourier-like series with polynomial Fourier coefficients as inspired by Fulford and Blake (1983). They model the ciliary beat by modelling the position of a point on the cilia as a Fourier series. However, while this model describes the shape of



(a) Data Surf Plot (b) Fitted Surf Plot (c) Fitted Waveform

Figure 2.3: Figure showing the wave fitting model for the data. Panel (a) shows the tangent angle given from the data while Panel (b) shows the tangent angle of the model waveform. In Panel (c) we display the waveform for the fitted model.

ciliary beat well, it does not conserve arclength. Therefore, we modify the method slightly to fit the beat in terms of the tangent angle. This helps to conserve the arc length of the beat. The tangent angle for the beat is therefore modelled by

$$\psi(s,t) = \sum_{n=1}^{N}\sum_{i=0}^{N}\left[A_{i,n}s^i + B_{i,n}s^i\cos\left(2\pi n\left(ks-\omega t+\alpha\right)\right) + C_{i,n}s^i\sin\left(2\pi n\left(ks-\omega t+\alpha\right)\right)\right]. \tag{2.36}$$

The constants in equation (2.36) can be chosen by fitting the function to the data using the least squares method. A comparison of how this matches to the experimental data is seen in Figure 2.3 as well as a depiction of the fitted waveform for $N = 2$. We use the waveform in Equation (2.36) to model the remaining flagella and cilia beats in this thesis.

We then wish to find the representation of our flagellar waveforms in Cartesian coordinates. This will enable us to use the points on the flagella in the Nearest Neighbour Method. Since the waves are planar, we can first describe them in the x, y plane setting the z component equal to 0. This gives

$$x(t) = \int_0^L \cos(\psi(s,t))ds, \quad \text{and} \quad y(t) = \int_0^L \sin(\psi(s,t))ds, \tag{2.37}$$

where L is the length of the flagellum. This integral can be calculated numerically. We then translate and rotate these points to place the flagella in the desired place on the body of the swimmer.

For modelling the swimming of the algal colonies we also need to know the velocity of the beating flagellum. This can be achieved by differentiating ψ with respect to t. For the first waveform model presented with the tangent angle described in (2.35), this is given by

$$\frac{\partial \psi(s,t)}{\partial t} = \psi_1(s)\sin(t+\phi(s)). \tag{2.38}$$

The velocity for the second waveform model, for which the tangent angle is defined in equation (2.36), is given by

$$\frac{\partial \psi(s,t)}{\partial t} = \sum_{n=1}^{N}\sum_{i=0}^{N}\left[2\pi n\omega B_{i,n}s^i \sin\left(2\pi n\left(ks-\omega t+\alpha\right)\right) - 2\pi n\omega C_{i,n}s^i\cos\left(2\pi n\left(ks-\omega t+\alpha\right)\right)\right]. \tag{2.39}$$

As with the position, for use within our method we wish to find the velocity in polar coordinates. Again, we initially set this to be in the x and y direction setting the z component equal to 0. The Cartesian velocities are given by

$$\dot{x}(t) = -\int_0^L \frac{\partial \psi(s,t)}{\partial t}\sin(\psi(s,t))ds \quad \text{and} \quad \dot{y}(t) = \int_0^L \frac{\partial \psi(s,t)}{\partial t}\cos(\psi(s,t))ds. \tag{2.40}$$

2.5 Flux Calculation

In parts of this thesis we will sometimes consider the flux produced by the flagella as an analogue to swimming. This flux represents the amount of fluid that is moved by the cilia over its beat. One example of where this will be used is as part of convergence analysis for swimmers with many flagella. Using the flux calculation here will allow us to consider the effects of increasing flagella but with lower computational complexity than for modelling

a full swimmer. We will also use the flux calculations throughout section 3.1 in which we will do an in depth study of the metachronal wave. If we consider all the flagella beating in the x direction then we calculate the $x-$component of the flux produced by the flagella by integrating the force of the flagella pushing the fluid in the x direction multiplied by the height of the points on the flagella producing that force over the length of the flagella and time for one beat. Mathematically, this is given by

$$Q_x = \sum_1^N \int_0^{2\pi} \int_0^1 F_x(s,t) z(s) ds dt, \tag{2.41}$$

where $z(s,t)$ is the height of the flagella above the boundary at arclength s and time t and $F_x(s,t)$ is the x component of the force at that point. This represents the amount of fluid that is pushed along by the flagella. We have the dependence on $z(s)$ because the flagella will be able to push less fluid the closer it gets to a boundary at $z = 0$.

For flagella beating in other directions in the $x - y$ plane, we can calculate the flux in the direction of the flagella beat using the force in the flagella direction. This flux is given by

$$Q = \sum_1^N \int_0^{2\pi} \int_0^1 \sqrt{\left(F_x^2(s,t) + F_y^2(s,t)\right)} z(s) ds dt, \tag{2.42}$$

where $F_y(s,t)$ is the y component of the force at that point.

As well as the total flux over a flagella beat we will also study how the flux changes over a single beat which we will call the time varying flux denoted by Q_t. The $x-$ component for the time varying flux is given by

$$Q_t = \sum_1^N \int_0^1 F_x(s,t) z(s) ds. \tag{2.43}$$

We will use our equations to calculate the flux in studying the metachronal wave in Section 3.1.

In this chapter we have introduced the methods that we will be using to model algal

colonies and their swimming behaviour. We will use the level set method for modelling the body of the swimmer, with our models of the flagella waveforms for the flagella. In this thesis, we will be using the ellipsoid level set method to create the cells for multicellular algal colonies. The Nearest Neighbour method will then be used to calculate the swimming behaviour of the algal colonies. We will also study the swimming of the multiciliate protozoan, *Didinium* using our centre-line level set method. In the next chapter we will look at studying the metachronal wave.

CHAPTER 3

STUDYING THE METACHRONAL WAVE

3.1 Models With a Prescribed Cilia Beat

Large arrays of cilia, such as those in the airways or on a multiciliate swimmer, often coordinate themselves to beat with a metachronal wave (Elgeti and Gompper, 2013). In this chapter, we look to study the mechanics of this metachronal wave, and the interactions between neighbouring cilia in more detail.

We start by considering models for the cilia in which we prescribe the swimming gait of the cilia. We then find the flux produced by these cilia formed into different metachronal waves. We can then use this to study the optimal metachronal wave to produce the largest flux. However, since for these models we prescribe the beat of the cilia, this beat is unable to be changed due to the influence of neighbouring cilia. Therefore, in the second half of this chapter we will use a bead and spring model to study the interactions between cilia. These models prescribe a force on to a bead attached to a spring to simulate the motion of a cilium. Since we do not prescribe the full beat, it is able to be influenced by neighbouring cilia. We will later apply these approaches using prescribed beat kinematics and bead and spring models to free swimming microorganisms.

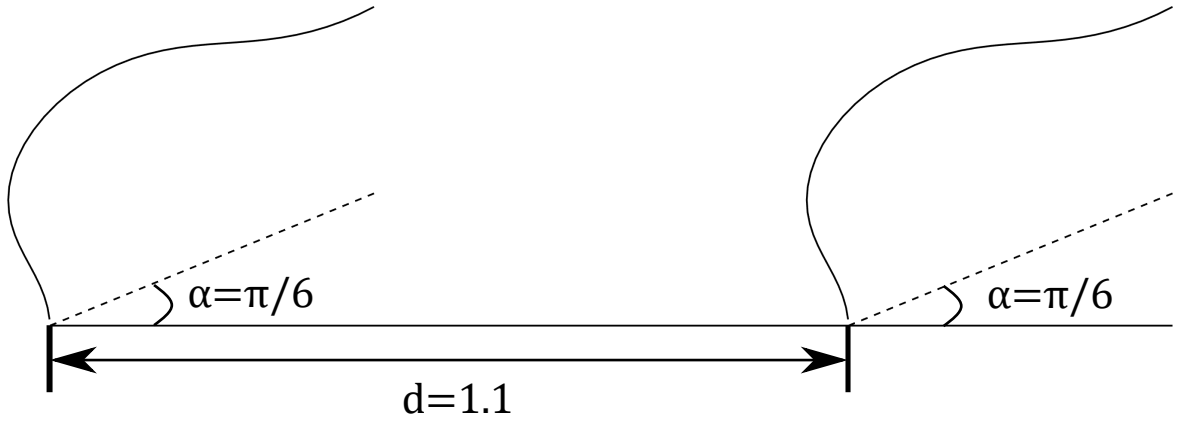
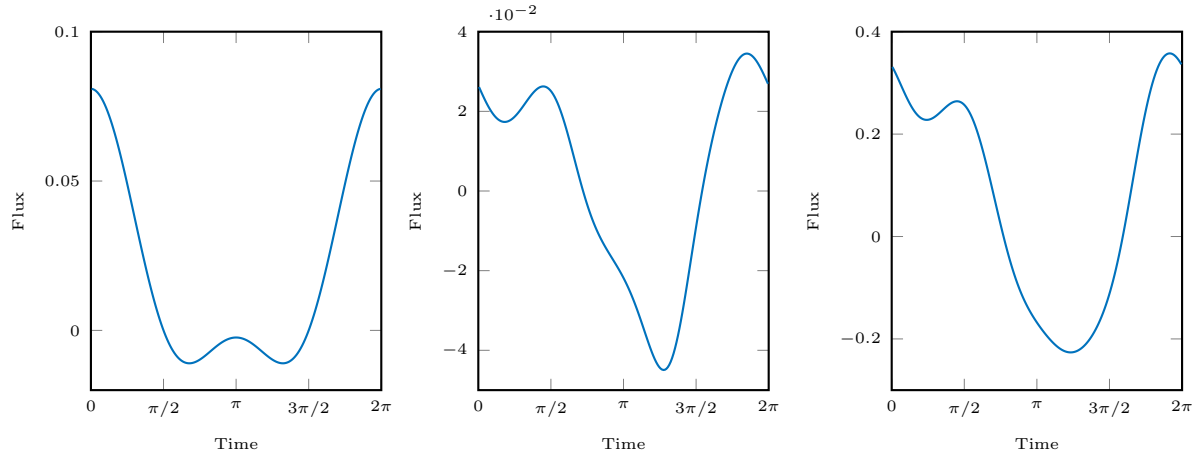


Figure 3.1: Figure showing variables we consider in studying the flux from a metachronal wave. d is the distance between one cilia and the next and is measured in flagella lengths. α is the angle (twisted at the base) of cilia. This angle is the angle between the line that connects the two cilia (represented by the bottom horizontal line) and plane that the flagella beat in and is measured in radians. We calculate the flux in the x direction (to the right in this figure).

3.1.1 Flux from one beating cilium

We model the metachronal wave by considering the flux produced by flagella over a boundary. Using this we test the effect of multiple factors on the flux from a metachronal wave. The main parameters that we will test are the distance between the cilia (d), as well as their angle of orientation (α) as shown in Figure 3.1.

We first model the flux produced by one cilium beating on a boundary. We use this result as a baseline to compare to the results for the metachronal waves. We do this for three separate models. We consider two regularised force models in which the cilia is modelled with a singular regularised force, one with a circular trajectory and the other with a more accurate trajectory resembling our fitted waveform in equation (2.36). The third model will consider the flux from a full cilium discretised by multiple regularised Stokeslets over a line representing the cilium. To calculate the flux for one cilium, we use the time varying flux model in equation (2.43). The forces used to calculate the flux are found using the method of regularised Stokelslets by rearranging equation (2.13). We find the z value required to calculate the flux from the prescribed trajectory of the flagella that is either circular or from our fitted flagella model in equation (2.36).



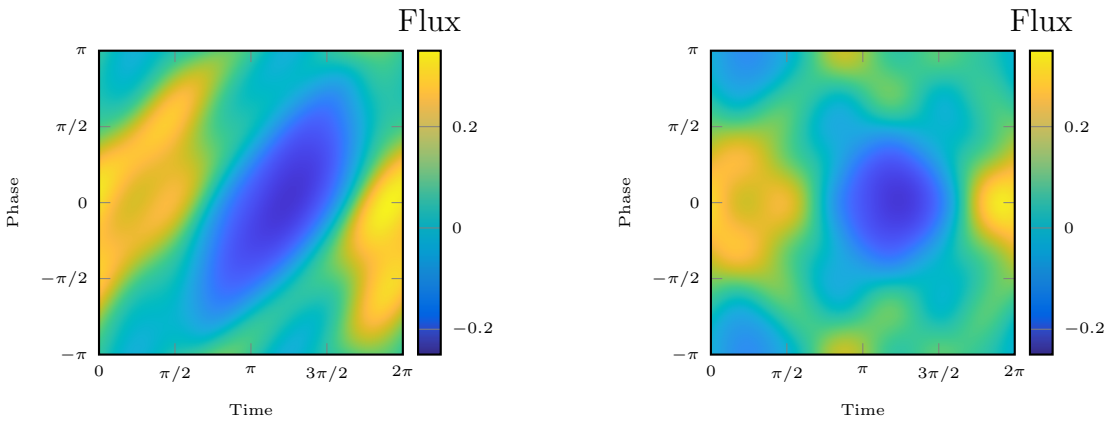
(a) Regularised Force Circular

(b) Regularised Force Accurate

(c) Full Cilium

Figure 3.2: Figure showing the flux produced over time by one beating cilium over one beat calculated using the time varying flux equation in (2.43). Panels (a) and (b) represent the cilium as a regularised force with a circular trajectory with radius $r = 0.5$ in Panel (a) and a more accurate trajectory in Panel (b). Panel (c) shows the flux from a full cilium of length 1.

The flux over time produced by one beating cilium over one beat for each of the three models is shown in Figure 3.2. The positive values for the flux come from the effective stroke of the cilia with the flux becoming negative during the recovery stroke of the cilia as would be expected. Comparing the three models we see that qualitatively they are reasonably similar. The flux over time for the regularised force model with the accurate trajectory is qualitatively very similar to the flux over time calculated using the full cilium model, although quantitatively it is much lower as would be expected. This shows that the regularised force model with the accurate trajectory provides a good qualitative understanding of the flux. Looking at the circular trajectory regularised force model, we see that overall it is able to show some similar trends to the other two models showing it can also provide some valid insight in to the flux. However, we see that the plot is symmetric around $t = \pi$ which is not present in the other two. This is to be expected since the circular trajectory is symmetric while this would not be the case for a full cilium. However, we are still able to find reasonable trends from the circular regularised force model. We now look at the full cilia model for multiple cilia to study the metachronal



(a) 2 Cilia (b) 3 Cilia

Figure 3.3: Figure showing the flux over time and Phase difference between the cilia of length 1 as a surface plot. These results were found using the full cilium model. We take the flux measurements with $d = 1.1$ and $\alpha = 0$. Panel (a) shows the data for 2 cilia and Panel (b) shows the data for 3 cilia. This data is normalised over the number of cilia.

wave and flux produced in more detail.

3.1.2 Flux over time vs Phase Difference For Multiple Cilia Using The Full Cilium Model

We now study the flux from multiple beating cilia with a metachronal wave for full cilia of length 1 as introduced above in Section 3.1.1. For finding the flux of multiple cilia, we set up our model with the cilia arranged equidistant from each other in a line with equal phase difference between neighbouring cilia to represent metachronal waves. We note that for multiple cilia we expect flow field they produce will not just simply be additive. This is since the cilia have interactions with each other modifying the flow that they collectively produce.

For the waveform of the cilia, we use the fitted waveform from equation (2.36). We first consider the flux produced by the cilia over time for different phase differences between the cilia again making use of the time varying flux given in equation (2.43). For each of these results, we normalise the flux with respect to the number of cilia. This allows us compare more directly to each other using the flux over time for one cilium and study more clearly the effects of the metachronal waves and hydrodynamic interactions between

the cilia.

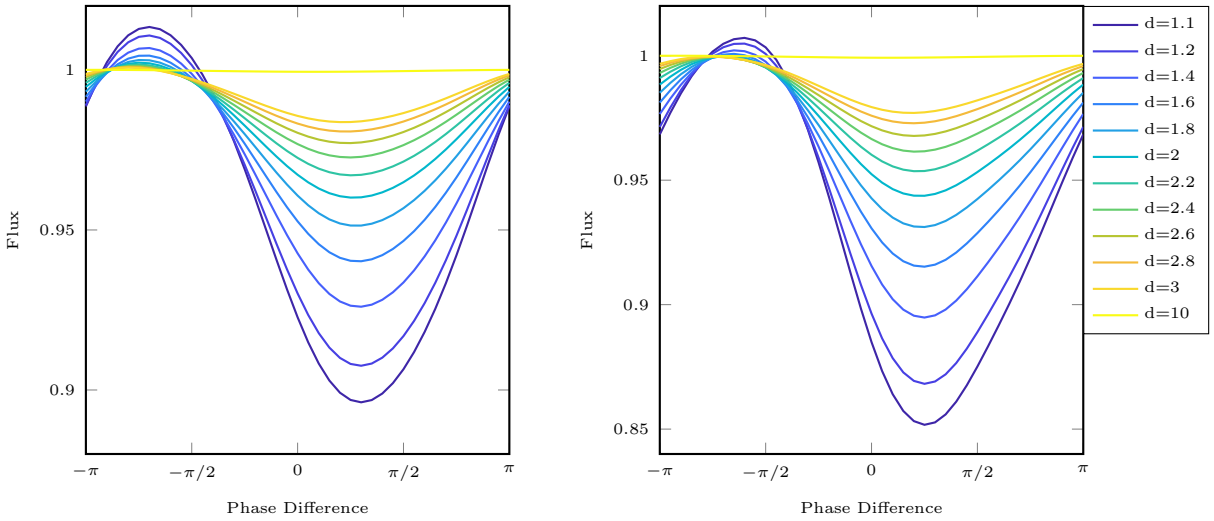
The results for the flux over time for one beat in the x direction for two and three cilia with varying phase difference between the neighbouring cilia are shown in Figure 3.3 as a surface plot. These results are found for cilia a distance of $d = 1.1$ apart (where d is measured in cilia lengths) and beating in the x direction.

For a synchronous wave with a phase difference of 0, we see that the flux over time normalised over the number of cilia are very similar to each other for two and three cilia as shown in Figure 3.3 as well as to one cilium as shown in Panel (c) of Figure 3.2. This is true both qualitatively and quantitatively. However, we do notice some differences between two and three cilia for non-synchronous beating. For two cilia, we see that the minimum of the flux over time occurs at a later time in the beat as the phase difference between the cilia increases from $-\pi$ to π. However, for three flagella, we find that this minimum stays mostly at the same value of t as shown by the darker blue circular part of Panel (b) of Figure 3.3. However for larger phase differences for both symplectic and antiplectic waves, this minimum for the cilia case no longer appears.

3.1.3 Distance Between Cilia vs Metachronal Flux

Next, we consider the effect of changing the distance between cilia. Here the distance is given by d in terms of the cilia length. For the results, this time we show the total flux in the x direction after one beat as given in equation (2.41) rather than the flux over time. As before we normalise the results though now with respect to both the number of cilia and the total flux after one beat produced by one cilium as calculated using our full cilium model. We calculate our results for differing phase difference between neighbouring cilia to test metachronal waves with varied metachronal wave numbers. Here and throughout the thesis we represent the symplectic wave with positive phase difference and the antiplectic wave with negative phase difference.

In Figure 3.4, we show the results of the total flux over one beat for varying phase difference between the cilia for two and three cilia. We show this for increasing distance,



(a) 2 Cilia

(b) 3 Cilia

Figure 3.4: Figure showing the total flux after one beat over the phase difference between cilia of length 1 for increasing distance d between the cilia. We keep $\alpha = 0$. We show this for 2 cilia in Panel (a) and 3 cilia in Panel (b). The flux is normalised over the total flux from 1 cilia and the number of cilia. In this figure and throughout the thesis, negative phase difference represents an antiplectic metachronal wave and positive phase difference represents a symplectic metachronal wave.

d, between the cilia. Here we see, that as we increase the distance between the cilia the metachronal wave has reduced effect. This is also shown by Gueron et al. (1997) who find that for their model, the influence of flagella on neighbouring flagella was negligible if the distance between them exceeded two flagella lengths. In both cases, for the largest distance between the cilia of $d = 10$ cilia lengths, we see the normalised flux is constant at 1 for all phase differences. This shows that cilia far enough away from each other have no effect on each other as would be expected.

For smaller distances the effect of the metachronal wave on the flux is qualitatively similar for all of the distances between the cilia for both two and three cilia, though the effects are greater the closer the cilia are. The greatest flux is found for an antiplectic metachronal wave with a negative phase difference between cilia of less than $-\pi/2$. The symplectic beat however is seen to produce a much lower flux, suggesting that swimmers with a symplectic beat may swim slower than swimmers with flagella that beat with an antiplectic metachronal wave.

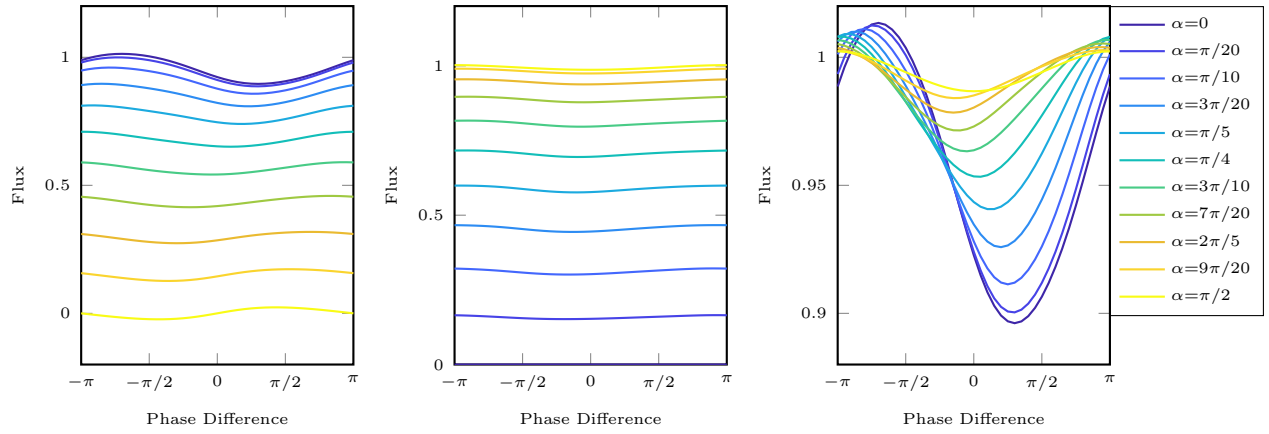
3.1.4 Angle of Flagella vs metachronal flux

We now consider the effect of varying the angle of cilia to the x-axis denoted by α. We keep the distance between flagella at $d = 1.1$ and the metachronal wave moves in the x direction. We again find the total flux after one beat as presented in equation (2.41) which we have normalised with respect to the number of cilia and the total flux from one cilium. We find the flux in both the x and y direction as well as the direction of the beating cilia. We present this the results of these flux calculations in each direction for two and three cilia in Figure 3.5 with results for two cilia in the top row and three cilia in the bottom row.

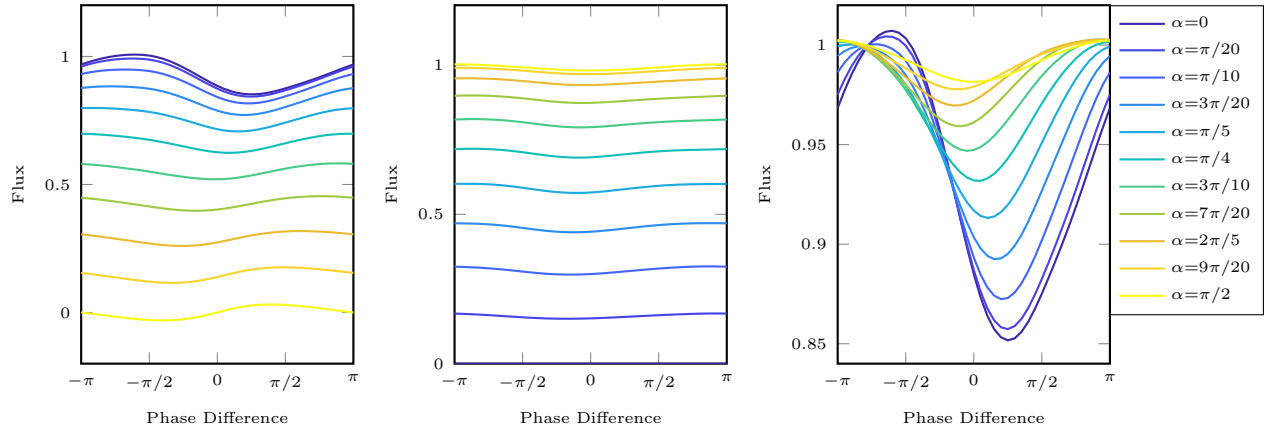
Studying the flux in the x direction (shown in Panels (a) and (d)) and y direction (shown in Panels (b) and (e)), we see that the x component decreases as the angle increases towards $\alpha = \pi/2$ while the y component does the same in reverse. This is to be expected as the cilia start beating solely in the x direction at $\alpha = 0$ and rotate to be in the y direction at $\alpha = \pi/2$. We also note that the change in phase difference has a smaller effect on the flux in the y direction than in the x direction. This is found since the metachronal wave is also beating in the x direction.

When the direction of the cilia is perpendicular to the component of the flux we notice some interesting behaviour. The y component of the flux for $\alpha = 0$ is at 0 for all phase differences as would be expected. However, this is not the case for the x component of the flux at $\alpha = \pi/2$ when the cilia beat in the y direction. This is found purely as a result of the effect of hydrodynamic interactions seen since the metachronal wave is in the x direction. Therefore, the metachronal wave is found to produce its own pumping effect adding to the flux in its direction even when the cilia are beating perpendicularly

We now study the flux in the direction of the beating cilia in Panels (c) and (f) of Figure 3.5. This is calculated using equation (2.42). As with the distance, we find that the effect of the phase difference becomes less prominent as the angle increases towards $\alpha = \pi/2$ where the cilia beat perpendicularly to the direction of the metachronal wave. However, the phase difference of the cilia always has some effect, even when the the beat



(a) 2 Cilia Flux in x Direction (b) 2 Cilia Flux in y Direction (c) 2 Cilia Flux in Cilia Direction



(d) 3 Cilia Flux in x Direction (e) 3 Cilia Flux in y Direction (f) 3 Cilia Flux in cilia Direction

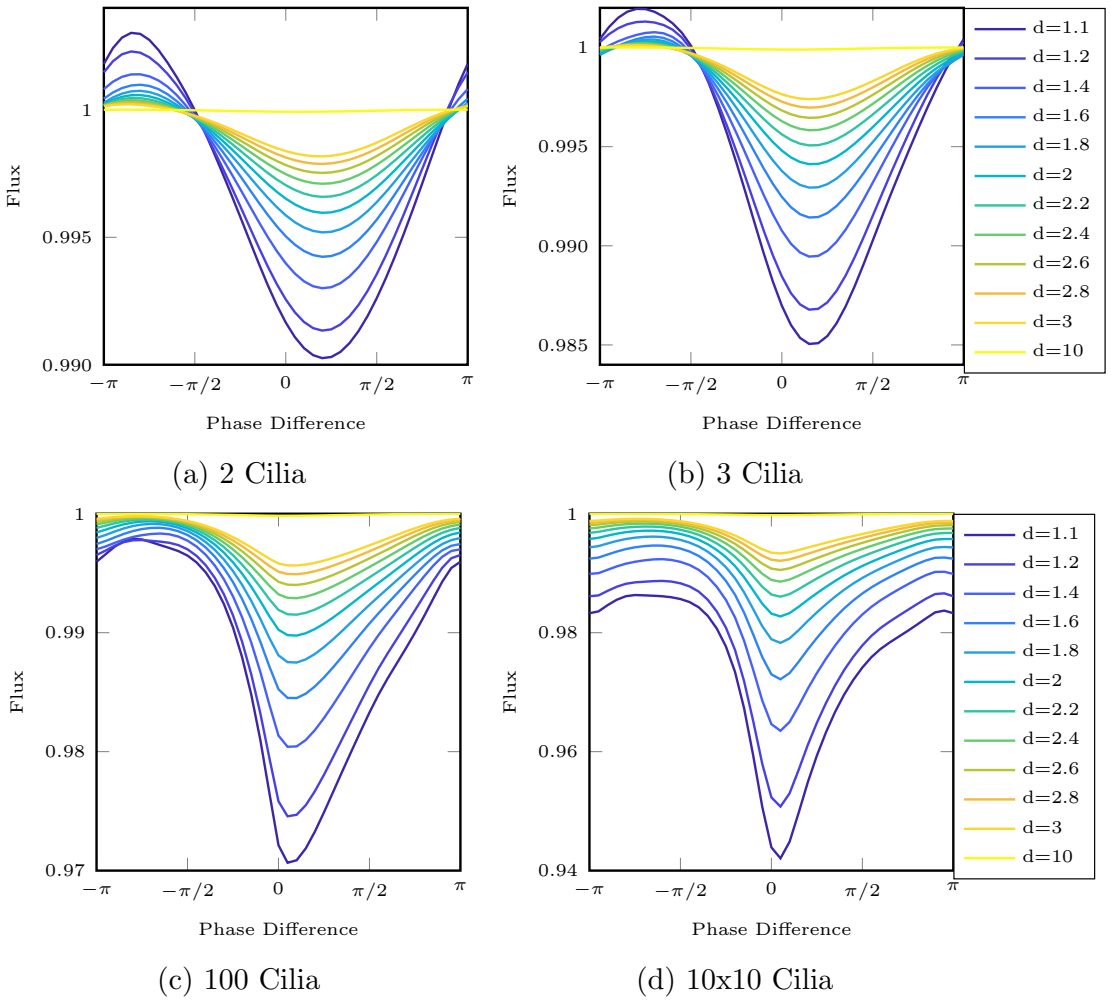
Figure 3.5: Figure showing the total flux after one beat over the phase difference between cilia of length 1 for varying angle α between the cilia. We keep $d = 1.1$. The top row shows the results for 2 cilia and the bottom row shows the results for 3 cilia. Panels (a) and (d) show the flux in the x direction, Panels (b) and (e) show the flux in the y direction and Panels (c) and (f) show the flux in the direction of the cilia. The flux is normalised over the total flux from 1 cilia and the number of cilia. The metachronal wave of the cilia is in the x direction.

and metachronal wave are perpendicular. We also note that as the angle increases the minimum of the flux moves closer to a phase difference of 0 reaching it when $\alpha = \pi/2$. Therefore, when the direction of the cilia beat and metachronal wave are perpendicular to each other, whether the metachronal wave is to the left or to the right makes no difference on the flux produced in the direction of the cilia.

3.1.5 Modelling the Cilium As a Single Regularised Force

We now simplify our model by studying the flux from multiple cilia using the two regularised force models as introduced in Section 3.1.1 with both a circular trajectory and a more accurate trajectory. For both of these models, we will study results for two and three cilia. We can then compare these results to those of the full cilium model. This will allow us to see if we are still able to find accurate results using a simplified model with the cilium represented by one regularised force. We again calculate the flux for these models using equation (2.41). For the simplest model of the circular regularised force model, we will also be able to consider a much larger number of cilia. Therefore, we also study the flux for one hundred cilia both arranged in a line with equidistant cilia and equal phase difference between neighbouring cilia as well as a ten by ten lattice. For the ten by ten lattice, we arrange the cilia such that the cilia with equal x value in a row have the same phase as each other with equal phase difference between neighbouring rows. The cilia are placed equidistant from each other, with the distance d representing the distance between neighbouring cilia in both the x and y directions. For the circular regularised force model, we model the cilia as a regularised force moving in a circle with radius $r = 0.5$. For the accurate regularised force model we use a cilium of length 1 using the fitted waveform from equation (2.36). We then follow a single point three quarters along the cilium to obtain our trajectory.

First, we study the effect of increasing the distance between the cilia. We show the results for the case of the circular regularised force model in Figure 3.6. In this figure, we present the total flux after one beat for increasing distance between the cilia and different



(a) 2 Cilia

(b) 3 Cilia

(c) 100 Cilia

(d) 10x10 Cilia

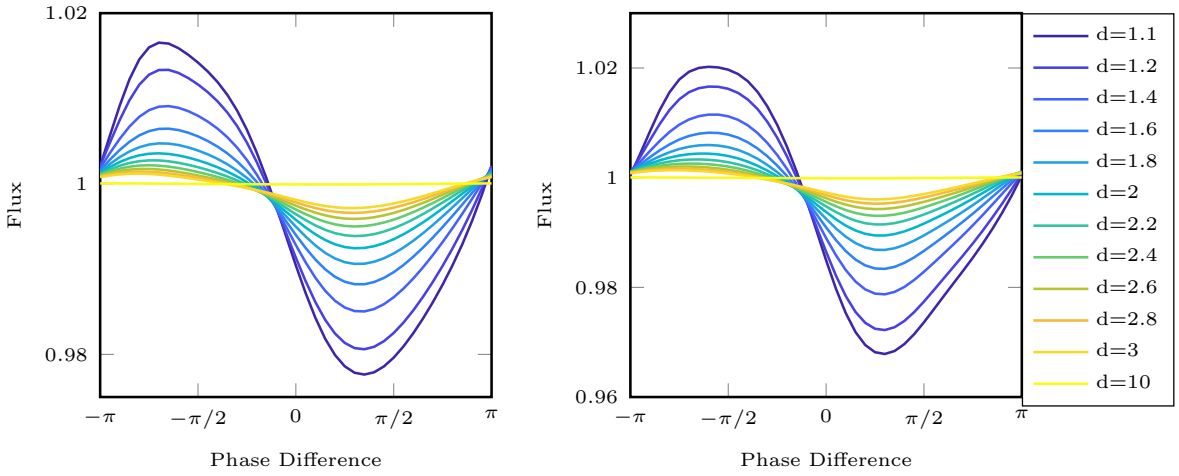
Figure 3.6: Figure showing the total flux after one beat over the phase difference between cilia for increasing distance d between the cilia. We keep $\alpha = 0$ and the cilia are modelled using the circular regularised force model with a radius of $r = 0.5$ and normalised over the total flux from one cilium using this model. We show this for 2 cilia in Panel (a), 3 cilia in Panel (b), 100 cilia in Panel (c) and a lattice of ten by ten cilia in Panel (d).

phase differences between neighbouring cilia. These results are for two and three cilia as well as a hundred cilia in both a line and in a ten by ten lattice. We also normalise these results over the total flux from one cilium as calculated using the circular regularised force model as well as the number of cilia.

For the largest distance between cilia of $d = 10$, we note that the normalised flux remains at 1 for all phase differences in each case. This would be expected since as we increase the distance between the cilia, they have less of an influence on each other. Specifically, the far-field flow from a force parallel to a boundary decays like $1/d^2$ (this is seen from the form of the stress tensor T_{ijk} as introduced in Equation (2.7)), therefore hydrodynamic interactions are very weak at this distance. We also see that for each distance between the flagella, the results are qualitatively very similar but with change in the phase differences having a larger effect for smaller distances between cilia. For two and three cilia, this is qualitatively very similar to our results for the full cilium model.

In all numbers of cilia we note that there is a minimum flux found for a slightly symplectic metachronal wave as also seen in the results for the full cilium model. This is somewhat unexpected since many swimmers with a large number of cilia typically swim with a symplectic metachronal wave. We also notice that there is a peak for an antiplectic metachronal wave. However, this agrees with Milana et al. (2020) and Osterman and Vilfan (2011) who find that the optimal metachronal wave for both a line and lattice array of cilia is an antiplectic wave. The reason for this is possibly because this is a prescribed kinematics model, and does not include internal force generation. For prescribed kinematics, more force is required to keep the bead going on a fixed trajectory when neighbouring beads are dragging it the opposite way, this leads to higher flux.

For two and three cilia in Panels (a) and (b) respectively, the maximum of the plots is greater than one meaning that the cilia together are able to produce more flux than the same number of cilia working individually. However, as the number of cilia increases, this maximum decreases. This is seen in the case of one hundred cilia, in both a line in Panel (c) and a lattice in Panel (d), where the flux no longer becomes greater than 1.



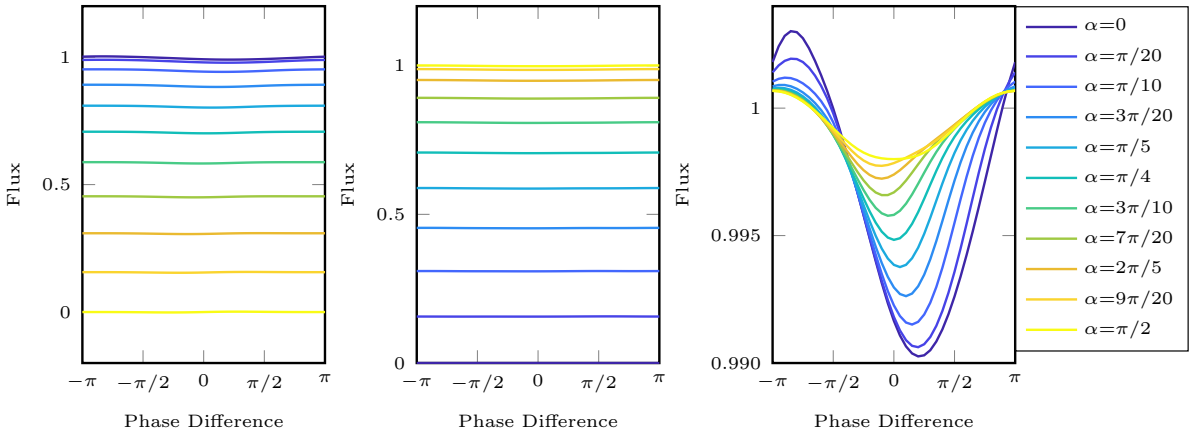
(a) 2 Cilia (b) 3 Cilia

Figure 3.7: Figure showing the total flux after one beat over the phase difference between cilia for increasing distance d between the cilia. We keep $\alpha = 0$ and the cilia are modelled using the Accurate regularised force model and normalised over the total flux from one cilium using this model. We show this for 2 cilia in Panel (a), 3 cilia in Panel (b).

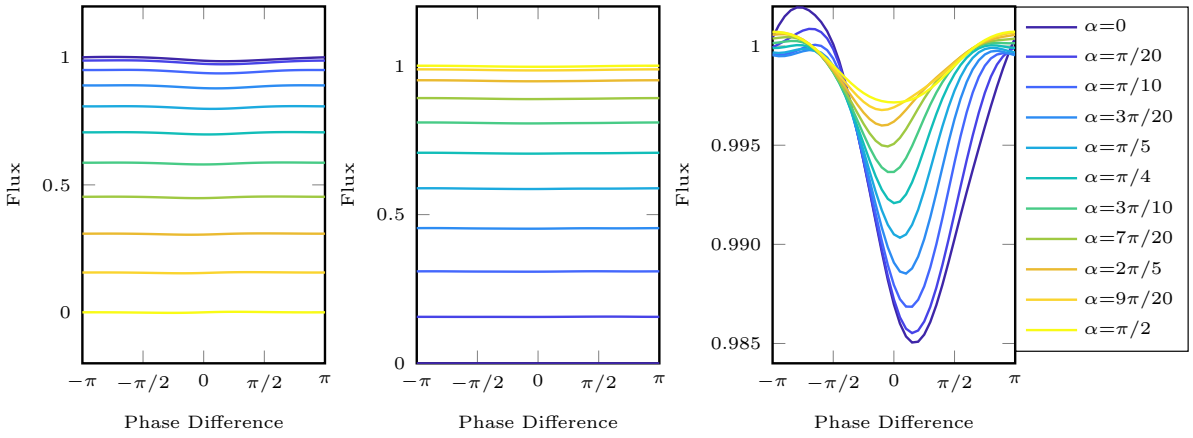
We now look at improving this study of the effect of the distance between cilia on the flux produced by using the regularised force model with a more accurate trajectory. These results are displayed in Figure 3.7. We find many similarities with the Circular regularised force model such as the existence of a maximum for the antiplectic metachronal wave and a minimum for the symplectic metachronal wave. However we note that the normalised flux is found to be greater than 1 for a much larger array of antiplectic metachronal waves.

We now move on to study the effect of the angle of the cilia for our regularised force models. For two and three cilia, we show the results produced by the Circular regularised force model in Figure 3.8. In this figure we show the total flux produced in the x direction in Panels (a) and (d), y direction in Panels (b) and (e) and in the direction of the cilia in Panels (c) and (f) for varying angle α of the cilia. Here we find that the flux decreases as it is rotated away from the direction of the calculated flux until it is at 0 when the cilia are perpendicular to the direction of the calculated flux as would be expected.

We can study the more interesting behaviour when considering the flux in the direction of the cilia. The behaviour for varying angle is very similar for both two and three cilia. The minimum flux of the system is found to decrease as the angle increases. We also note

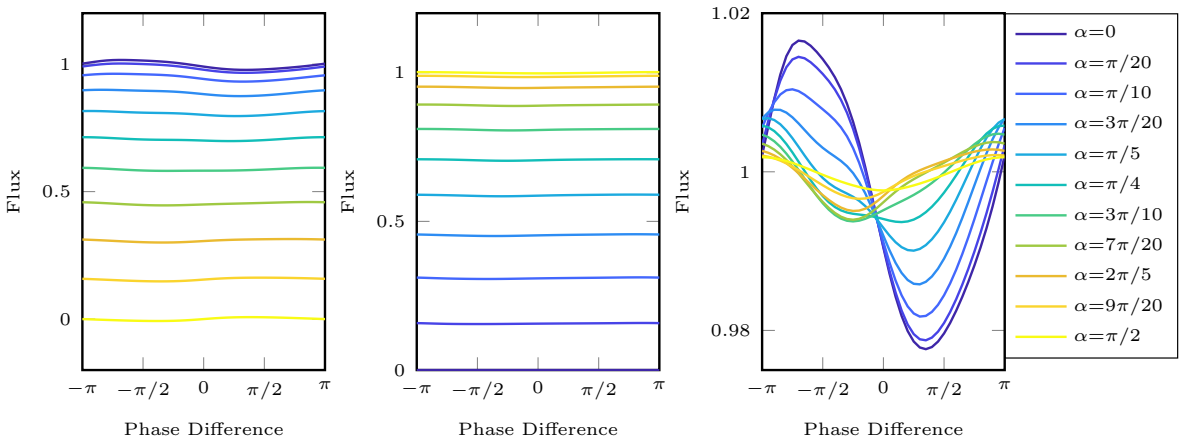


(a) 2 Cilia, x Direction (b) 2 Cilia, y Direction (c) 2 Cilia, Cilia Direction

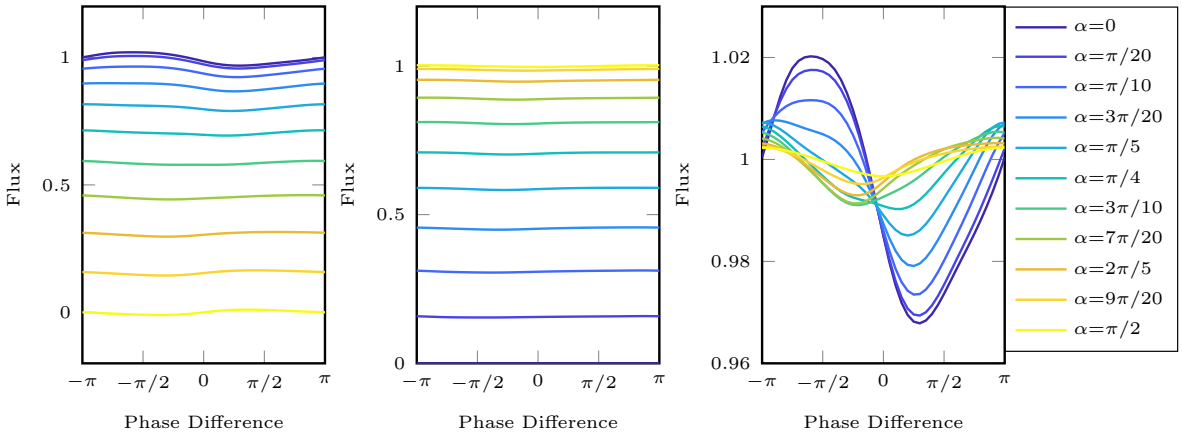


(d) 3 Cilia, x Direction (e) 3 Cilia, y Direction (f) 3 Cilia, Cilia Direction

Figure 3.8: Figure showing the total flux after one beat over the Phase Difference between cilia for varying angle α between the cilia. We keep $d = 1.1$ and the cilia are modelled using the circular regularised force model with radius $r = 0.5$ and normalised over the total flux from one cilium using this model. We show the flux in the $x-$direction (Panels (a) and (d)), $y-$direction (Panels (b) and (e)) and the direction of the cilia (Panels (c) and (f)) with the results for two cilia in the top row and the results for three cilia on the bottom row.



(a) 2 Cilia, x Direction (b) 2 Cilia, y Direction (c) 2 Cilia, Cilia Direction



(d) 3 Cilia, x Direction (e) 3 Cilia, y Direction (f) 3 Cilia, Cilia Direction

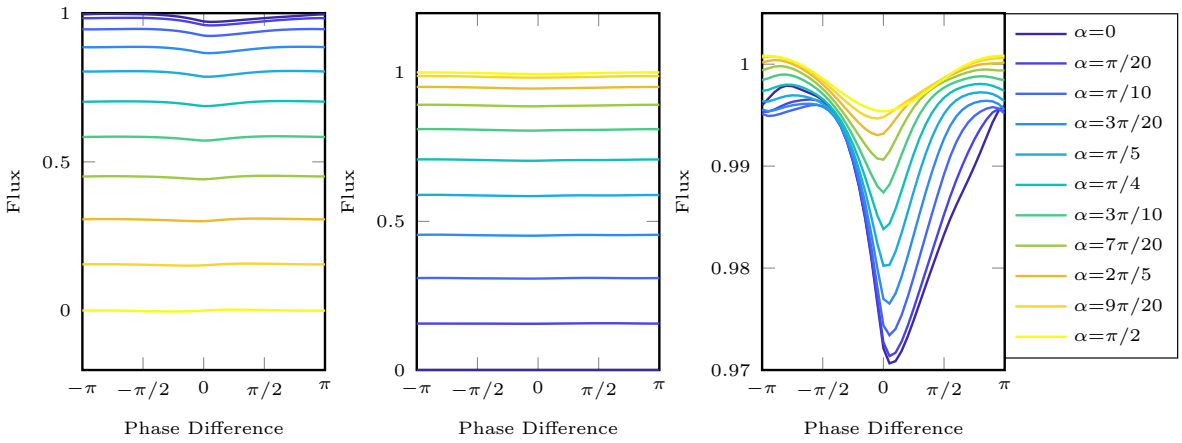
Figure 3.9: Figure showing the total flux after one beat over the Phase Difference between cilia for varying angle α between the cilia. We keep $d = 1.1$ and the cilia are modelled using the accurate regularised force model and normalised over the total flux from one cilium using this model. We show the flux in the $x-$direction (Panels (a) and (d)), $y-$direction (Panels (b) and (e)) and the direction of the cilia (Panels (c) and (f)) with the results for two cilia in the top row and the results for three cilia on the bottom row.

that this minimum occurs for a phase difference becoming increasingly closer to 0 as the angle increases. This then shows that for $\alpha = \pi/2$ the direction of the metachronal wave makes no difference. This is expected since for $\alpha = \pi/2$, the direction of the metachronal wave is perpendicular to the direction of the beating.

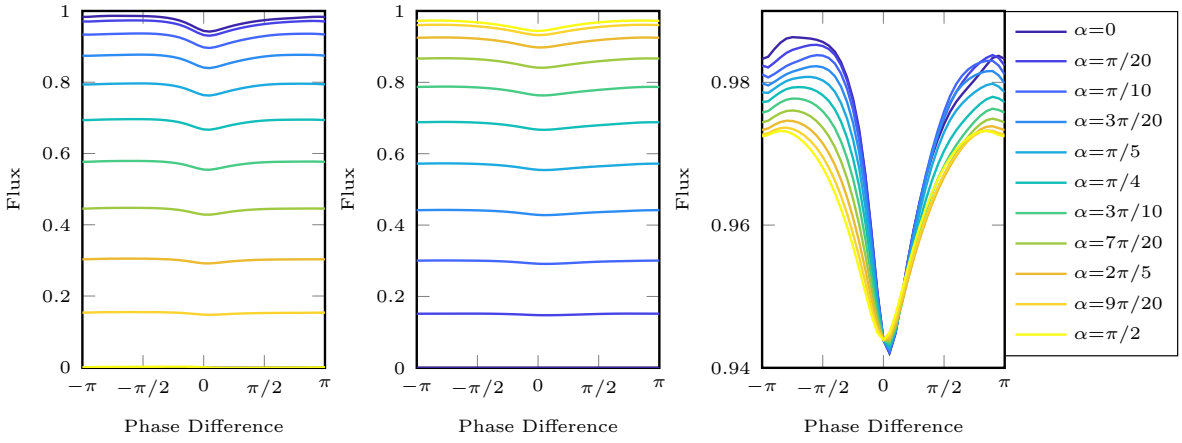
Next, we wish to test how these results differ for our more accurate regularised force model. Our results for the total flux after one beat for varying angle α of the cilia using our more accurate regularised force model are shown in Figure 3.9. For the regularised force model with an accurate trajectory, we find very similar behaviour to that of the circular model with the main difference again being that the flux is greater than one for a much wider array of antiplectic waves. We also note that the range of the flux over phase difference appears slightly greater for the regularised force model with an accurate trajectory.

We next study the effect of changing angle for a larger number of cilia using the Circular regularised force model. We show the results for the total flux produced over one beat for varying angle α of hundred cilia arranged in both a line in Panels (a)-(c) and a ten by ten grid in Panels (d)-(f) in Figure 3.10. The minimum for one hundred cilia in a line, behaves very similarly to that of two or three flagella. This is also similar for ten by ten grid with the minimum moving up and closer to a phase difference of 0. However, the difference between these minimums is very small.

In this section, we found that the results for the flux produced by cilia modelled with a single regularised force are qualitatively very similar to results from our full cilium model. This means that we can have confidence that we can find qualitatively accurate results for models using a single regularised force to represent a cilium. Therefore, we now move on to study a fluid-structure interaction model using bead and spring method where we model the flagella with a single bead attached to a spring. This will allow us to study the interaction between cilia and how they coordinate with each other. Qualitatively accurate results will be useful in studying these models to understand the behaviour of the cilia in how they coordinate with each other and types of metachronal waves that they may



(a) 100 Cilia, x Direction (b) 100 Cilia, y Direction (c) 100 Cilia, Cilia Direction



(d) 10x10 Cilia, x Direction (e) 10x10 Cilia, y Direction (f) 10x10 Cilia, Cilia Direction

Figure 3.10: Figure showing the total flux after one beat over the Phase Difference between 100 cilia for varying angle α between the cilia. We keep $d = 1.1$ and the cilia are modelled using the circular regularised force model with a radius of $r = 0.5$ and normalised over the total flux from one cilium using this model. We show the flux in the $x-$direction (Panels (a) and (d)), $y-$direction (Panels (b) and (e)) and the direction of the cilia (Panels (c) and (f)) with the results for the cilia in a line in the top row and the results for the cilia arranged in a 10 by 10 lattice on the bottom row.

form. Quantitatively accurate results would be required for studying swimming speeds of swimmers with these models.

3.2 Synchronisation Model - Bead and Spring Model

We now consider the synchronisation behind how the cilia form metachronal waves and how cilia coordinate with each other. To do this, we model beating cilia over a boundary using a bead and spring model. We have modelled the prescribed beat flux for both our full cilia and single regularised force models, and found them to be in good qualitative agreement for singular and arrays of cilia. Therefore, we can have some confidence that we can find accurate results for the coordination of cilia using a bead and spring model with a single bead to model a cilium. We model a cilium as a single bead attached to a spring with a fixed origin of the spring which we will call the spring origin. We then apply a driving force to the particle, perpendicular to the spring direction. This gives us a bead with a circular trajectory to represent the beating cilium. Throughout the rest of this chapter, the beads will be represented in two different ways. That is by Regularised Stokeslets as presented in equation (2.14) or Regularised Blakelets as presented in equation (2.22) for the bead and spring model beating next to a boundary.

To study this model, we first consider the case with one bead and study the forces acting on our bead. We have the spring force, which we will denote by $\boldsymbol{F_{spr}}$, the normal driving force, which we will denote by $\boldsymbol{F_{Dri}}$ and the drag force denoted by $\boldsymbol{F_{Drag}}$. Since we are in the case of Low Reynolds number, we have force balance meaning

$$\boldsymbol{F_{Spr}} + \boldsymbol{F_{Dri}} + \boldsymbol{F_{Drag}} = \mathbf{0}. \tag{3.1}$$

The bead is modelled by a regularised force, $\phi_\epsilon F_{Dri}$ located at $\mathbf{x}$ driving the flow. Here ϕ_ϵ is a regularisation function as given in equation (2.12). For this, we note that a regularisation parameter of $\epsilon = 3a/2$ produces a regularised force that exerts the same

force on the fluid as a sphere of radius a when travelling at the same speed in free space. The force the fluid exerts on the bead (the drag force) is then related to the speed of the bead via $\boldsymbol{u} = \dot{\mathbf{x}} = -B^{\epsilon}(\mathbf{x}, \mathbf{x}) \cdot \boldsymbol{F_{Drag}}$, where $B^{\epsilon}(\mathbf{x}, \mathbf{x})$ is the regularised Blakelet as given in equation (2.22). Rearranging Equation (3.1) then gives the velocity of the bead as

$$\boldsymbol{u} = B^{\epsilon}(\boldsymbol{x}, \boldsymbol{x}) \cdot (\boldsymbol{F_{Spr}} + \boldsymbol{F_{Dri}}). \tag{3.2}$$

Here the force from the spring is pointing along the direction of the spring with it either pointing towards or away from the spring origin depending on whether the current length is greater than or less than the natural length of the spring respectively. Using Hooke's law, the spring force is given by

$$\boldsymbol{F_{Spr}} = K\left(|\boldsymbol{x} - \boldsymbol{y}| - l\right) \cdot \frac{(\boldsymbol{x} - \boldsymbol{y})}{|\boldsymbol{x} - \boldsymbol{y}|}, \tag{3.3}$$

where $\boldsymbol{x}$ is the current position of the bead, $\boldsymbol{y}$ is origin of the spring, l is the spring's natural length and K gives the stiffness of the spring.

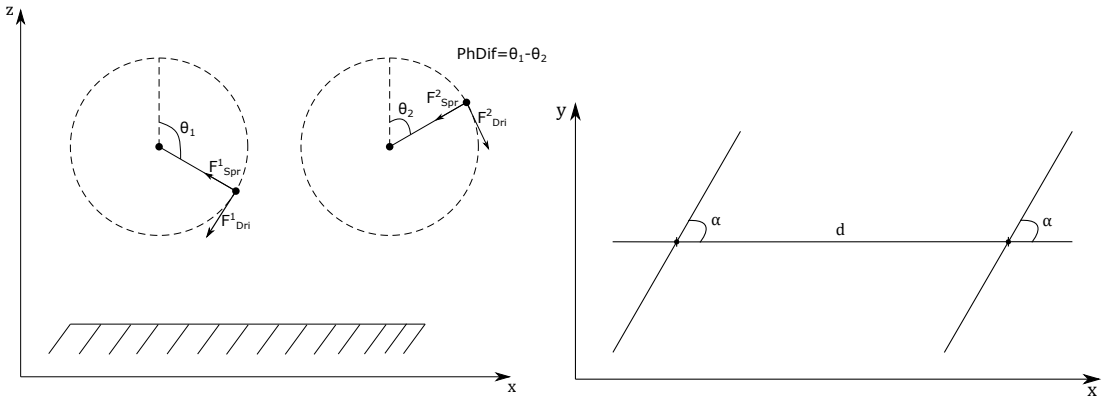
To demonstrate how this model is extended to multiple beads we look at the model for two beads. We again have force balance on each of the two beads. This force balance on bead i is given by $\boldsymbol{F^i_{Spr}} + \boldsymbol{F^i_{Dri}} + \boldsymbol{F^i_{Drag}} = \mathbf{0}$. Here we note that $\boldsymbol{F^i_{Drag}}$ has both local and non-local components showing the force on it from both beads as well as the wall if we are using Blakelets. We then find the velocity of the bead 1 given by

$$\boldsymbol{u}(\boldsymbol{x_1}) = -B(\boldsymbol{x_1}, \boldsymbol{x_1}) \cdot \boldsymbol{F^1_{Drag}} - B(\boldsymbol{x_1}, \boldsymbol{x_2}) \cdot \boldsymbol{F^2_{Drag}} \tag{3.4}$$

similarly, the velocity of bead 2 is given by

$$\boldsymbol{u}(\boldsymbol{x_2}) = -B(\boldsymbol{x_2}, \boldsymbol{x_1}) \cdot \boldsymbol{F^1_{Drag}} - B(\boldsymbol{x_2}, \boldsymbol{x_2}) \cdot \boldsymbol{F^2_{Drag}} \tag{3.5}$$

This can be written as a matrix system given by



(a) Side View (b) Top Down View

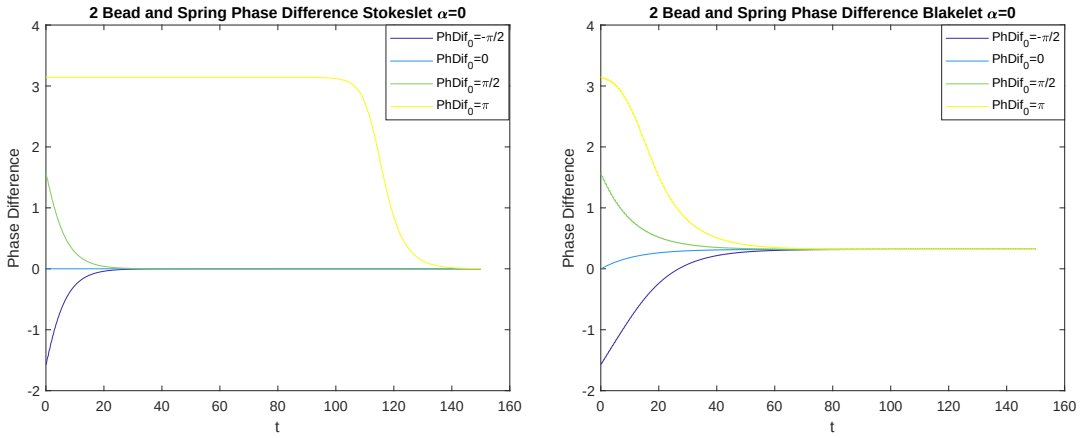
Figure 3.11: Schematic showing the setup and variables for our bead and spring model. Panel (a) shows a side on view while Panel (b) shows a topdown view. In Panel (a), we show the phases of the two beads θ_i given by the angle of the spring to a vertical line. The dashed lines represent the circular trajectories of the beads and we also show the forces acting on the beads $\boldsymbol{F^i_{Spr}}$ and $\boldsymbol{F^i_{Dri}}$. In Panel (b) we show the distance between the origins of the springs attached to each bead as d as well as the orientation angle α. α represents the angle of the trajectory of the bead from the x direction.

$$\begin{pmatrix} \boldsymbol{u(x_1)} \\ \boldsymbol{u(x_2)} \end{pmatrix} = - \begin{pmatrix} B(\boldsymbol{x_1}, \boldsymbol{x_2}) & B(\boldsymbol{x_1}, \boldsymbol{x_2}) \\ B(\boldsymbol{x_2}, \boldsymbol{x_2}) & B(\boldsymbol{x_2}, \boldsymbol{x_2}) \end{pmatrix} \begin{pmatrix} \boldsymbol{F^1_{Drag}} \\ \boldsymbol{F^2_{Drag}} \end{pmatrix} \tag{3.6}$$

We now study the synchronisation of these beads to analyse how cilia interact and coordinate with each other starting with a system studying two beads.

3.2.1 Bead and Spring Model For Two Cilia

We first consider the synchronisation of two beads with our bead and spring model. We will test our results for the beads represented as Stokeslets as well as Blakelets. This will allow us to test the impact that a boundary has on the synchronisation of cilia as modelled by our simple bead and spring model. We present how the beads will be set up and the parameters that we use in Figure 3.11. In Panel (a), we show a side view of the set up, where we show the forces acting on the beads as well as the phases, θ_i of the beads. In Panel (b) we show the top down view of the set up. We show the distance between the spring origins for the beads denoted by d. We also show the orientation angle α which



(a) Stokeslet, $\alpha = 0$ (b) Blakelet, $\alpha = 0$

Figure 3.12: Phase difference over time between two neighbouring beads as part of the bead and spring model for both Stokeslets (Panel (a)) and Blakelets (Panel (b)). The beads are positioned a distance of $d = 1.3$ apart from each other and they have a natural spring length of $l = 0.5$ This is done for different initial phase difference as well as $\alpha = 0$

represents the angle of the trajectory of the bead from the x direction.

In Figure 3.12 we study the effect of the initial phase difference between the two beads and show how the phase difference between the beads develops over time for $\alpha = 0$. We present this for beads represented as both Stokeslets and Blakelets. Here the spring origins of the beads are a distance of $d = 1.3$ from each other and the springs have a natural length of $l = 0.5$. From this figure, we notice that the initial phase difference has no effect on the phase difference that the two beads tend towards after a long time. The main difference we see here is the length of time taken for the two beads to reach a steady state. For example, we see that the beads that start asynchronous with a phase difference of $\pm\pi$ takes much longer to reach the final phase difference particularly in the case of the beads represented as Stokeslets in Panels (a). We also note in studying Panel (a) of Figure 3.12 that for Stokeslets the system appears to be metastable for an initial phase difference of $\pm\pi$. We predict that it moves away from this metastable steady state due to numerical noise. Here, the metastable fixed point differs from an unstable steady state in that more effort is required to move it away from this state or it moves away from the point too slowly to notice making it appear to be fully stable for period of time.

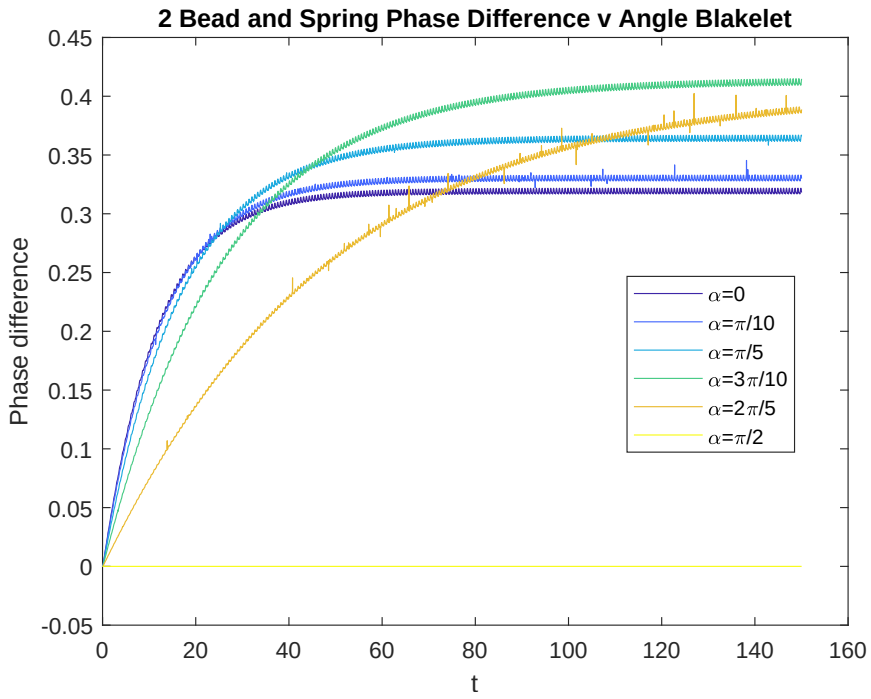
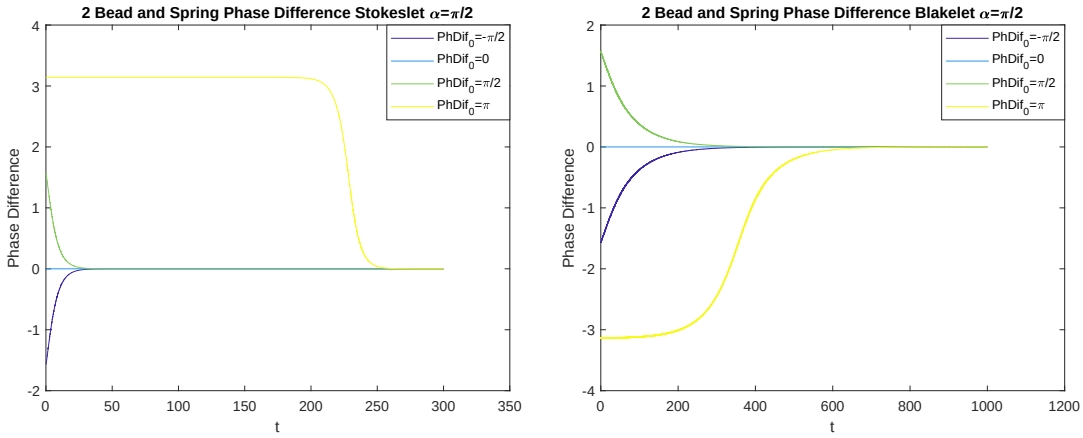


Figure 3.13: Phase difference over time between two neighbouring beads as part of the bead and spring model for Blakelets for different angles of beating α and starting at a Phase difference of 0. The bead and spring system has the spring origins a distance of $d = 1.3$ and natural spring length of $l = 0.5$.

When comparing the case of Stokeslets in Panel (a) to Blakelets in Panel (b), we also notice that they settle at different phase differences. In the case of Blakelets, the beads settle to be slightly symplectic, while the Stokeslets synchronise to have a phase difference between them of 0. This suggests that the boundary is necessary for cilia to form into metachronal wave when arranged in a line.

We next consider how the angle of the beating affects the synchronisation of the beads. Since we previously determined that the initial phase difference appears to have no effect for $d = 1.3$ in Figure 3.12, for these results we keep the initial phase difference at 0. The first of these results are shown in Figure 3.13 for the beads modelled as Blakelets using the same natural spring length and distance between spring origins as previously. In this figure we present the phase difference over time between two beads for different angles α.

For beads without the effects of a wall we find that the Stokeslets remain at a Phase difference of 0 for all values of α showing that the angle has no effect on where the beads



(a) Stokeslet, $\alpha = \pi/2$ (b) Blakelet, $\alpha = \pi/2$

Figure 3.14: Phase difference over time between two neighbouring beads as part of the bead and spring model for both Stokeslets (Panel (a)) and Blakelets (Panel (b)). This is done for different initial phase difference as well as $\alpha = \pi/2$. Again we have a spring length of $l = 0.5$ and distance between spring origins of the system of $d = 1.3$

synchronise and adding further evidence that a boundary is needed to form a metachronal wave in this model. We do not show a figure for this as it would just show a straight line for each angle α.

Considering the beads as Blakelets in Figure 3.13 we notice that the angle α of the beads trajectory now has an effect on how they settle at a steady state. The first thing to notice is that as the angle increases, the time taken for the beads to fully settle at a steady state increases. This would be expected as the beads are unable to get as close to each other when increasing the angle reducing the hydrodynamic interactions between the two. Another reason that we expect this is that the direction of the beat is moving away from the direction of the interactions between flagella. When looking at the final settled phase difference, we notice that as we increase the angle, the phase difference initially increases. However we note that for $\alpha = 2\pi/5$ that the final settled phase difference has decreased slightly from the previous value of $\alpha = 3\pi/10$. We also note that for the beads beating with a perpendicular angle of $\alpha = \pi/2$ that the phase difference remains at 0 with no change.

For the case of $\alpha = \pi/2$, we found in Figure 3.13 that the beads remain synchronous

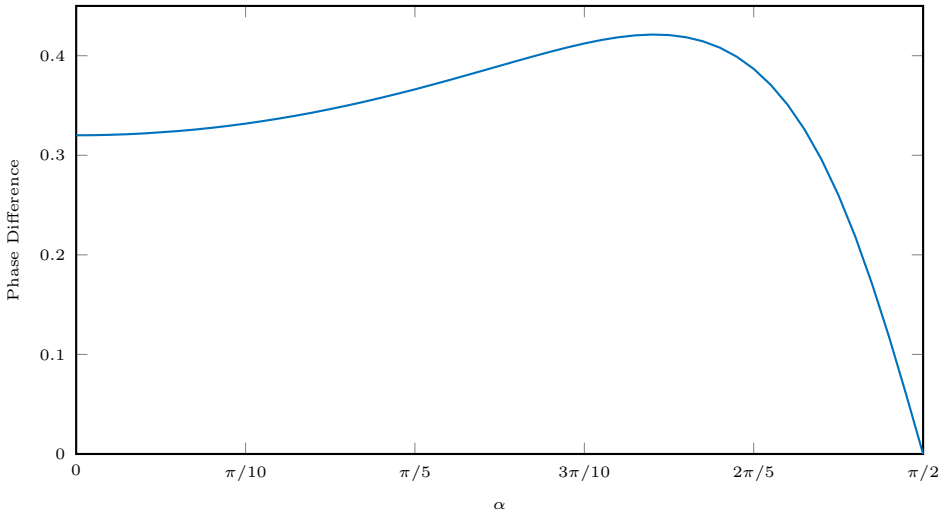


Figure 3.15: End Phase Difference of 2 beads in a bead and spring model over the angle α. Again we have a spring length of $l = 0.5$ and distance between spring origins of the system of $d = 1.3$

with each other. This suggests that either the beads tend towards a synchronous state, or are unaffected by each other and the end phase difference remains the same as the initial phase difference. We study this in Figure 3.14 using the same set up of the system in which we show the phase difference over time for different initial phase difference for $\alpha = \pi/2$. Here we see that the beads do eventually tend towards synchrony for all initial phase differences. Therefore, we find that the beads do interact with each other for $\alpha = \pi/2$. However, the beads do take a long time to synchronise suggesting that the interaction between the beads is very weak as would be expected.

To take a more in depth look at how the angle α affects the final settled phase difference we look at this final phase difference after a long time over the angle α for a higher resolution of α. These results are plotted in Figure 3.15. Here we see that the final settled phase difference increases slowly up to a peak shortly before $\alpha = 2\pi/5$. It then rapidly decreases reaching 0 at $\alpha = \pi/2$. We also note that for all angles α that the beads settle into a symplectic metachronal wave with a positive phase difference.

As well as the orientation of the beads trajectory we also study the effect of distance between the beads. We introduce the variable d to represent the distance between the origin of the springs of neighbouring beads. We show how increasing distance affects

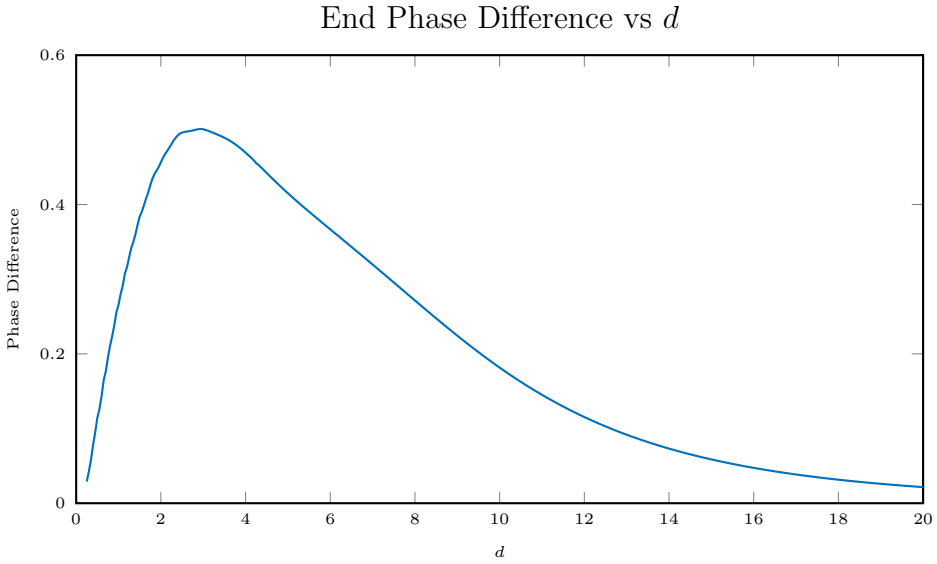
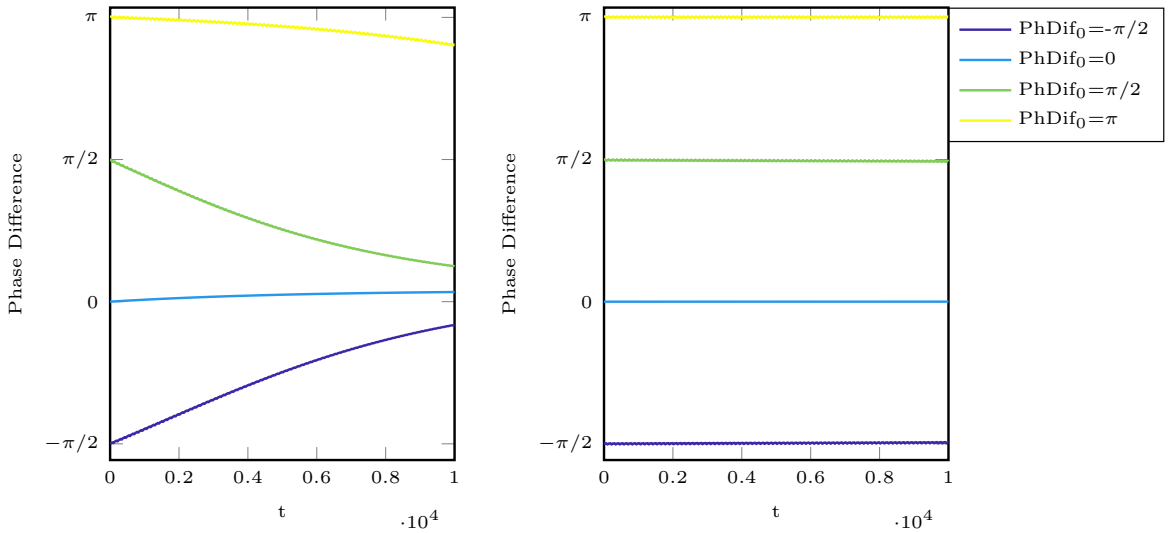


Figure 3.16: End Phase Difference of 2 beads in a bead and spring model over the distance between the origin of the springs. We have a spring length of $l = 0.5$ with angle $\alpha = 0$.



(a) $d = 20$ (b) $d = 100$

Figure 3.17: Phase Difference over time between two neighbouring beads as part of the bead and spring model for Blakelets. This is done for different initial phase differences as well as $\alpha = 0$ and a spring length of $l = 0.5$. In these results we test larger distances between beads with Panel (a) showing $d = 20$ and Panel (b) showing $d = 100$.

the final phase difference the system converges to in Figure 3.16 where we plot the end phase difference after a long time against the distance between neighbouring beads. These results are for the beads modelled as Blakelets using a spring length of $l = 0.5$ and angle $\alpha = 0$. Studying the figure, we see that the beads appear to have an optimum distance between them of approximately 3 in which the phase difference that the system settles to is at its maximum. After this point, the stable phase difference then decreases, getting close to zero, as the distance between beads increases. This decrease towards zero would be expected as the beads have less impact on each other as the beads get further away. Therefore the beads become less influenced away from their starting position with a phase difference of 0.

We further present this in Figure 3.17 where we show the phase difference over time for different initial phase differences with both $d = 20$ in Panel (a) and $d = 100$ in Panel (b). In Panel (a), we see that there is still some weak effect from the neighbouring beads on each other drawing it towards a potentially stable fixed point. However, once we reach very high distance between the beads as shown for $d = 100$ in Panel (b) of Figure 3.17, the neighbouring beads have no effect on each other and remain at their initial phase difference. For small d, the initial increase in phase difference towards the peak at approximately $d = 3$ as shown in Figure 3.16 is unexpected.

We can potentially try to explain this mathematically. For beads that are very close together with d approaching 0, we would expect them to be synchronous to each other as they stay close together. We then expect some phase difference between them as they move apart and able to feel the hydrodynamic effects of the other bead without being stuck next to it. We then expect it to go back down to a phase difference of 0 for very large d since as they get further away they become no longer able to feel the effect of the other flagella.

We can also potentially try to describe this behaviour using a more physical explanation. The system could have a preferred wave envelope with preferred wavelength that these two beads are attracted to. Since we have a travelling wave, as the beads get further

apart, the phase difference has to shift to remain part of the preferred wave envelope if it is still attracted to this. However, once you get passed a certain distance, the hydrodynamic interactions become too weak and the coupling decreases.

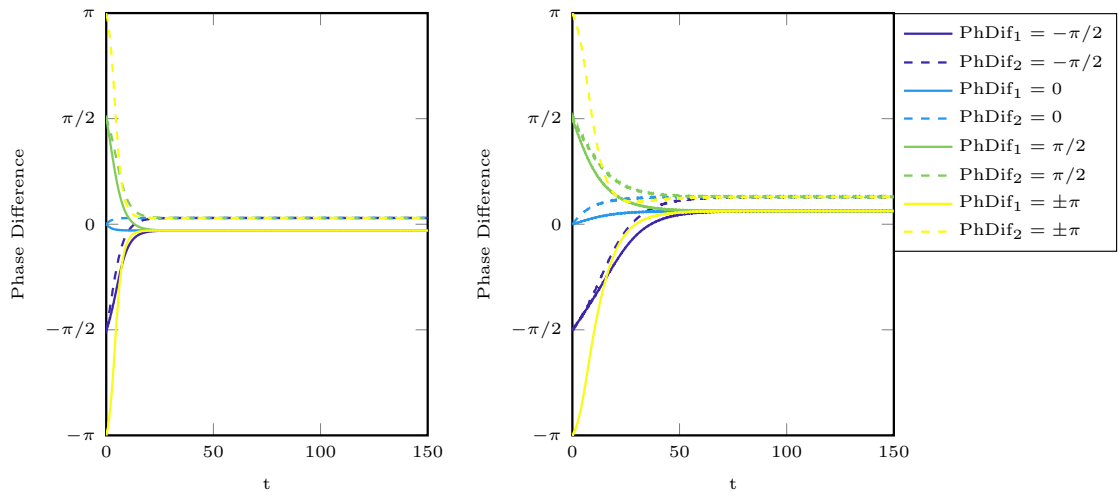
This can also potentially help to explain the peak in our results for varying the angle α. As we increase the angle flagella become further apart. This is somewhat similar to the case of increasing the distance between flagella therefore like moving along our graph for increasing distance. Since we start at a point that would be before the peak. Therefore we also potentially expect a peak for the change in angle.

3.2.2 Bead and Spring Model For Three Cilia

We now move on to a bead and spring model consisting of three beads. We arrange these beads spaced equidistantly along a line with a distance denoted by d between each bead. As with the case of two beads, we will test our model with three beads using both Stokeslets and Blakelets. This allows us to study the effect of a boundary on the synchronisation as well as studying the effects of a number of other factors. In each of the figures for three beads, we plot the phase difference between the first two beads with a solid line and the phase difference between the last two beads with a dashed line.

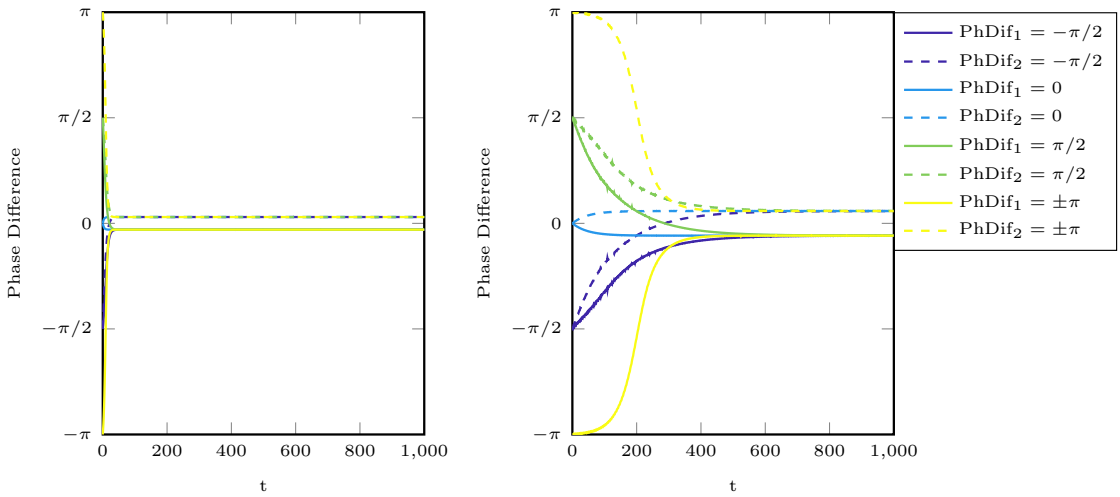
We initially consider the effect of the starting phase difference between neighbouring pairs of beads. We plot the change in phase difference over time for different initial phase differences for both $\alpha = 0$ and $\alpha = \pi/2$ with both Stokeslets and Blakelets in Figure 3.18. For our models with 3 beads in a line, the distance between spring origins is given by $d = 1.3$ and the springs have a natural length of $l = 0.5$. For these results we keep the initial phase difference between the first two beads equal to the initial phase difference between the last two beads for each case. In all four cases shown in this figure, we note the starting phase difference does not have an effect on the final phase difference that the beads settle at.

For all cases shown in Figure 3.18, we note that the phase difference of each neighbouring pair differs from each other meaning that the first two beads settle at a different



(a) Stokeslet,$\alpha = 0$

(b) Blakelet,$\alpha = 0$



(c) Stokeslet,$\alpha = \pi/2$

(d) Blakelet,$\alpha = \pi/2$

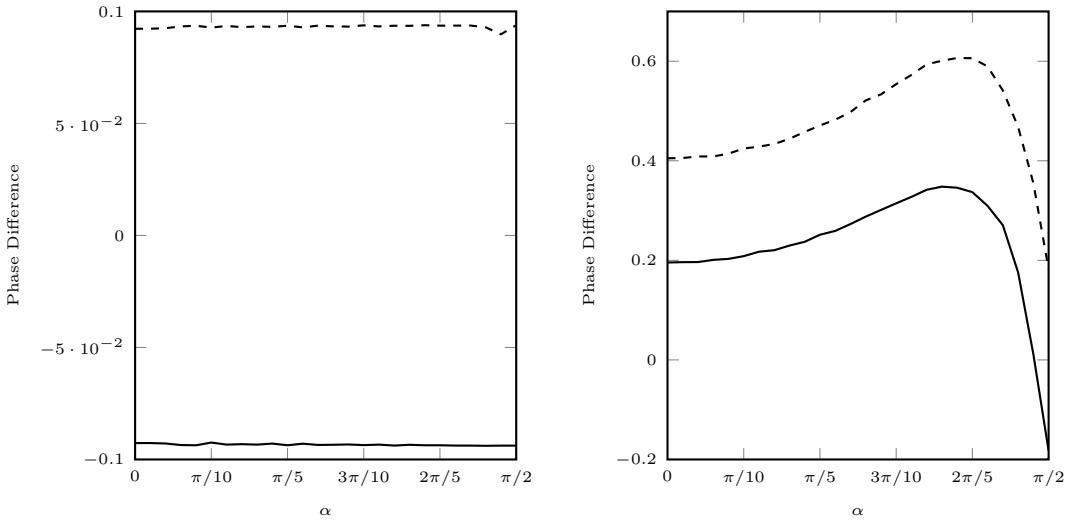
Figure 3.18: Phase difference over time between three neighbouring beads as part of the bead and spring model for both Stokeslets and Blakelets. This is done for different initial phase difference as well as both $\alpha = 0$ and $\alpha = \pi/2$. The distance between the spring origins of neighbouring beads are $d = 1.3$ and we have natural spring lengths of $l = 0.5$ The solid lines represent the Phase difference of bead 1 - bead 2, while the dashed line represents the Phase difference of bead 2 - bead 3

phase difference than the second two beads in all cases for this model. We now consider the case of $\alpha = 0$ in Panels (a) and (b). For the Stokeslets as shown in Panel (a) we see that the first pair of beads have a negative phase difference while the second pair of beads have a positive phase difference. This is an unexpected result as this is not a waveform that is typically seen amongst groups of cilia in nature. We would instead have potentially expected a metachronal wave or a different type of travelling wave which we do not see here. These two phase differences that the pairs of beads settle at have an average of 0 which is equivalent to the similar case for the bead and spring model with two beads.

Moving on to the model with Blakelets for $\alpha = 0$ in Panel (b), this time we note that both phase differences between the two neighbouring pairs of flagella beads tend towards a slightly positive phase difference. As with the case of Stokeslets we note that the last neighbouring pair of beads settles at a higher phase difference than the first pair. We again see that if we take the average of two phase differences that the pairs tend towards we reach a similar value to that found in the two bead case.

Considering the results for $\alpha = \pi/2$ in Panels (c) and (d) we notice similar trends. The last pair of beads again settles at a phase difference that is greater than the first pair of beads for both Stokeslets and Blakelets. The average phase difference that the pairs of beads tend to is around 0 in both cases with $\alpha = \pi/2$. As before this average is equivalent to the results found for two beads.

We predict that this spread of the phase difference of the neighbouring flagella around the result for the 2 bead case could be related to the number of flagella either side of the pair. For a neighbouring pair with equal number of flagella either side of the pair we expect that it would be equivalent to the two bead case. We then expect it to spread out from the two bead case depending on how imbalanced the number of flagella are. Therefore, we expect that to find a metachronal wave or synchronous beat as a stable fixed point, we would need to find a way to remove this imbalance. One way for which we would expect a metachronal wave to potentially occur would be for an infinite line of flagella. However we are unable to numerically study an infinite number of flagella.



(a) Stokeslet (b) Blakelet

Figure 3.19: End Phase Difference of 3 beads in a bead and spring model over the angle α for both Stokeslets and Blakelets. The solid line represents the Phase difference of bead 1 - bead 2, while the dotted line represents the Phase difference of bead 2 - bead 3. The spring origins between neighbouring beads have a distance between them of $d = 1.3$ and the springs have natural length of $l = 0.5$

Studying a comparison of the results for the Stokeslets and Blakelets for $\alpha = \pi/2$ we can notice two main differences. The first of these is the rate at which the pairs beads settle at a fixed point to reach their final phase difference. The Stokeslets in Panel (c) are shown to reach a steady state much faster than the Blakelets in Panel (d). This shows that a boundary increases the amount of time for the pairs of beads to settle at their desired phase difference. The second difference to note is that the Blakelets have larger difference between the phase differences of each neighbouring pair.

We now consider the effect of the angle α of the bead and spring trajectory for three beads. These results are shown in Figure 3.19 where we plot the end phase difference between the two neighbouring pairs of beads for varying angle α for both Stokeslets and Blakelets. For the Stokeslet case in Panel (a), we note that as in the case of two beads the angle α of the beads trajectory does not have an effect on the final Phase difference that the pairs of beads settle towards.

Looking at the results for the Blakelets in Panel (b) we see that each pair of beads is affected qualitatively in the same way. They increase slowly towards a peak shortly before

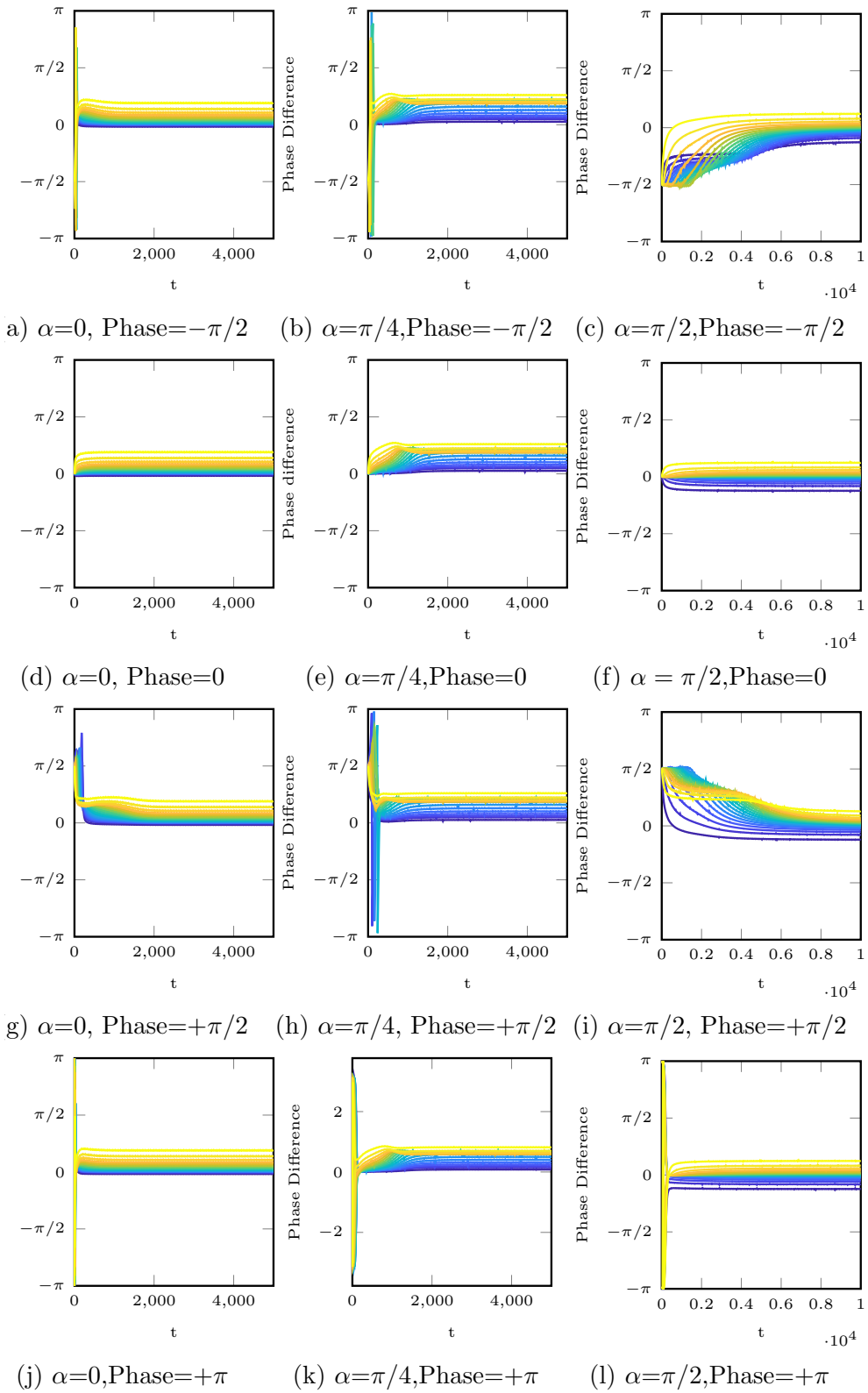
$\alpha = 2\pi/5$ and then rapidly decrease. We also note that if we take the average of the final phase difference over the two pairs, this results in very similar values to that of two bead case as shown in Figure 3.15. Therefore we see that for three beads in our bead and spring model, the two neighbouring pairs of beads have different phase differences to each other but these phase differences average to approximately the settled phase difference for two beads in our bead and spring model.

3.2.3 Bead and Spring Model For Twenty Cilia

We now consider a model consisting of twenty beads each representing a single cilium. As for the previous models we arrange these beads in a line equidistant from each other. For all of our twenty bead models, we use natural spring lengths of $l = 0.5$ and distance between the spring origins of $d = 1.3$. This helps us to study how larger groups of cilia are able to coordinate with each other. We again study the model both with a planar boundary (using Blakelets) and without a boundary (using Stokeslets). As with the case of fewer beads we test how the synchronisation changes related to a number of different factors.

As with two and three beads, we first consider the effect of the initial phase difference between the beads. We do this for three different orientations of $\alpha = 0$, $\alpha = \pi/4$ and $\alpha = \pi/2$. We plot the phase difference over time for twenty beads beating above a planar wall (modelled as Blakelets) starting at different initial phase differences in Figure 3.20. Here we show twelve plots with each row of plots showing a different initial phase difference and each column showing the different orientations α.

Studying the graphs for $\alpha = 0$ in Panels (a), (d), (g) and (j), we see some similarities to the results which we found for two and three beads. We see that the initial phase difference has a very minimal effect on the final state that the system settles at. As with the case of three beads we notice that this final steady state is centred approximately around the result for the two bead case. However unlike for three beads the stable steady state of the system is given by a steepening travelling wave. This wave is such that the



a) α=0, Phase=$-\pi/2$ (b) α=$\pi/4$,Phase=$-\pi/2$ (c) α=$\pi/2$,Phase=$-\pi/2$

(d) α=0, Phase=0 (e) α=$\pi/4$,Phase=0 (f) $\alpha = \pi/2$,Phase=0

g) α=0, Phase=$+\pi/2$ (h) α=$\pi/4$, Phase=$+\pi/2$ (i) α=$\pi/2$, Phase=$+\pi/2$

(j) α=0,Phase=$+\pi$ (k) α=$\pi/4$,Phase=$+\pi$ (l) α=$\pi/2$,Phase=$+\pi$

Figure 3.20: Phase difference over time between twenty neighbouring beads as part of the bead and spring model for beads near a wall modelled by Blakelets. The graphs are coloured using a parula colour map starting at the first pair of beads with the results in blue moving along to the final pair of beads with the results in yellow. This is done for different initial phase differences as well as different orientation angles of $\alpha = 0$, $\alpha = \pi/4$ and $\alpha = \pi/2$ as well as $d = 1.3$.

phase difference between neighbouring beads is steadily increasing as we move towards the right of the system of beads. This produces a travelling wave that appears to steepen as it moves towards the right hand side. This is much closer to the metachronal wave that we would expect, furthering our theory that the spread around the two bead case is caused by the effect of the position of the end points of the line and imbalance of cilia either side of the pair. Another difference to the results of two or three beads is that we find some notable difference in the way the beads approach the final steady state depending on the initial phase difference.

The largest difference in how the beads arrive at the steady state for $\alpha = 0$ is seen in Panel (g) for an initial phase of $\pi/2$. Here we see a quick slight increase in the phase between many of the neighbouring pairs of cilia before they eventually decrease towards the final steady state. This could suggest a potential bistability with the system tending towards another steady state before finally going towards the final steady state to match the other starting phase differences between neighbouring beads.

For $\alpha = \pi/4$ in Panels (b), (e), (h) and (k), we see similar behaviour to that of $\alpha = 0$. We again see that the initial phase difference has a very minimal effect on the final phase difference between neighbouring beads that the system tends towards. This is also equivalent to what we see in the case of two and three beads. Again the main changes are seen for an initial phase $= \pm\pi/2$, in Panels (b) and (h), in which the phase difference starts by rapidly varying before settling into its final state.

For beads organised to beat perpendicular to the direction of the wave between them at $\alpha = \pi/2$ in Panels (c), (f), (i) and (l), we see some differences to the previous cases. We initially note that for this orientation, the initial phase appears to have a slightly larger effect. The final phase difference is still consistent across all phases, though $\alpha = \pi/2$ in Panel (i) provides a much larger difference in how the systems arrive at this steady state.

For the system starting in synchrony (shown in Panel (f)) or asynchrony (shown in Panel (l)) (Phase$= 0$ or Phase$= \pi$), we see that as in the previous cases, the system tends towards the steady state fairly quickly with the system going straight towards the steady

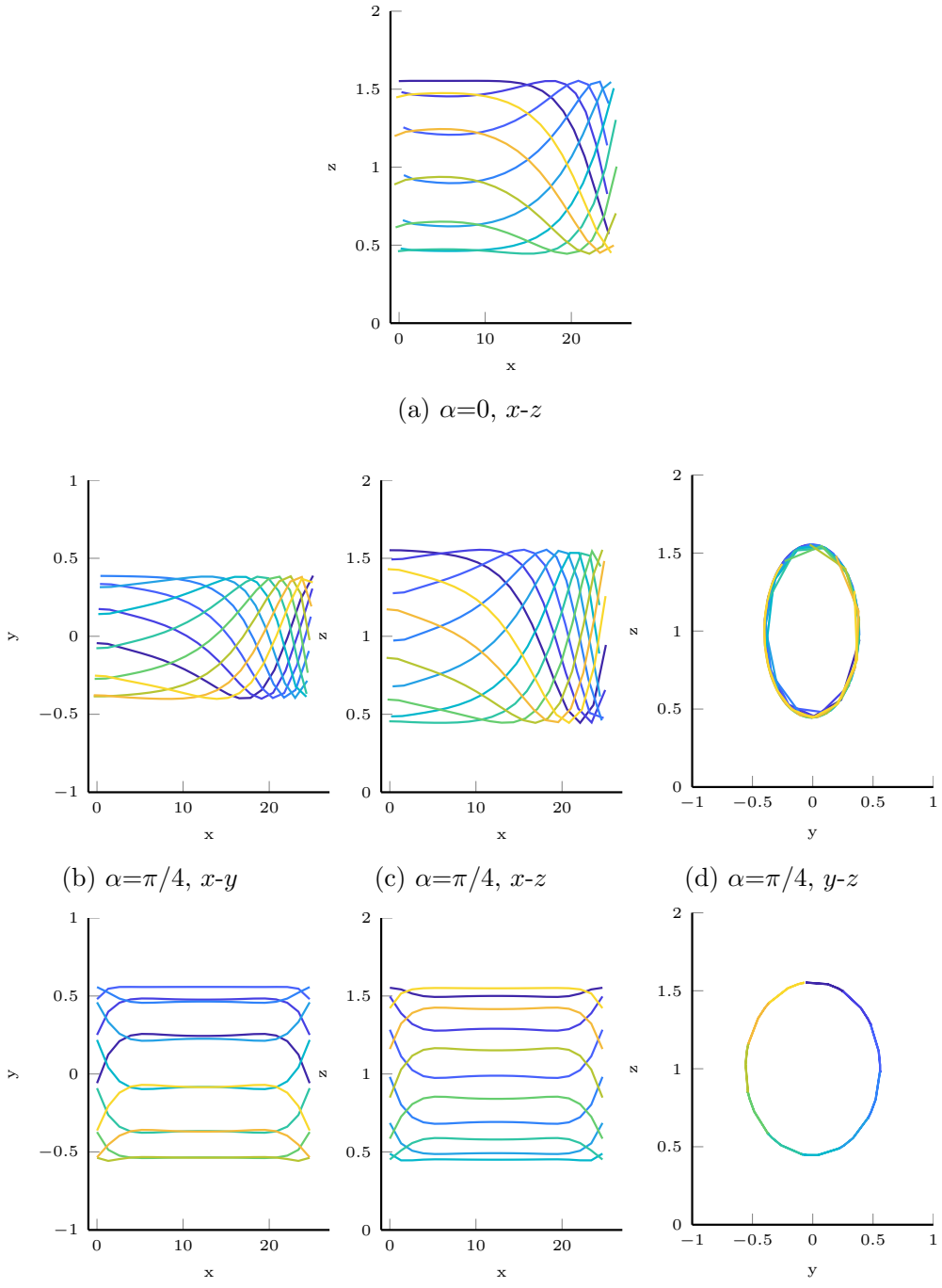
state in both cases. However, we notice that this changes for the initial Phase= $\pm\pi/2$ (shown in Panels (c) and (i)). Here we note that the system initially starts to settle into different states, of the same sign of the initial phase difference, before eventually settling into the steady state of the other cases for $\alpha = \pi/2$. This suggests that these may be another steady state for these systems.

To obtain a more intuitive understanding on how the system synchronises, we wish to study how the wave produced by the beads looks once the system has settled into its final steady state. We make a wave from the system by making a line connecting all of the beads and following how this moves over time as inspired by the spherical envelope description of metachronal waves by Blake (1971b). This is shown for each of the orientations α, over one period in Figure 3.21. This figure shows us the waveform produced by connecting a line through all of the beads over the full beat once they have reached a steady state.

For $\alpha = 0$, we show the wave in the x-z plane in Panel (a) since for this case, all of the bead's movement is in this plane. Here we note that the left half of the wave stays fairly consistently straight throughout the full motion of the wave as it moves up and down. Considering the full wave, we see that it moves in an almost whip-like motion.

Looking at $\alpha = \pi/4$, we first note that the motion is no longer entirely within the x-z plane. Therefore the beads will produce a 3-D wave. We show this in Panels (b)-(d) of Figure 3.21 giving the wave in the x-y, x-z and y-z planes. Studying Panels (b) and (c), we see that the wave has a similar shape to the case of $\alpha = 0$ particularly for the x-z plane. However instead of being a planar beat moving up and down, we see that it produces a rotating slightly helical wave.

The wave form produced for $\alpha = \pi/2$ is shown in Panels (e)-(g) of Figure 3.21. Here we see that the wave keeps the same shape through out its full period. That is, it keeps a straight shape throughout the middle of the wave with both ends being tilted down in the same direction. This then moves in a circular motion producing a circular wave. A possible explanation for this is that by symmetry the beads want to tend towards a synchronous beat which is seen for the cilia in the middle of the line. However, there are



(a) α=0, x-z

(b) α=$\pi/4$, x-y

(c) α=$\pi/4$, x-z

(d) α=$\pi/4$, y-z

(e) α=$\pi/2$, x-y

(f) α=$\pi/2$, x-z

(g) α=$\pi/2$, y-z

Figure 3.21: Figure showing the wave form of the bead and spring model for 20 beads. The colours of the plot represent the time which is increasing as we move through the parula colour map from blue to yellow. This is done in the x-z plane for three orientations of $\alpha = 0$, and the x-y, x-z and y-z planes for $\alpha = \pi/4$ and $\alpha = \pi/2$.

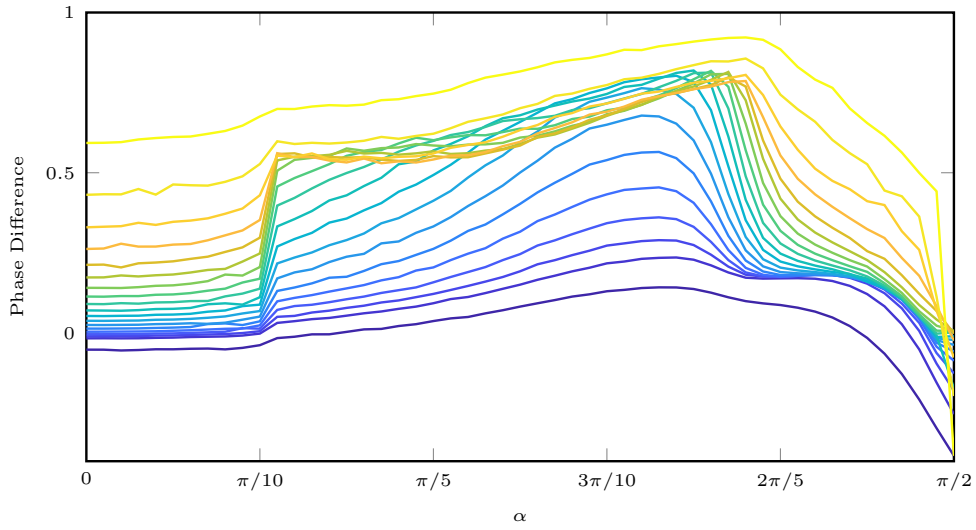


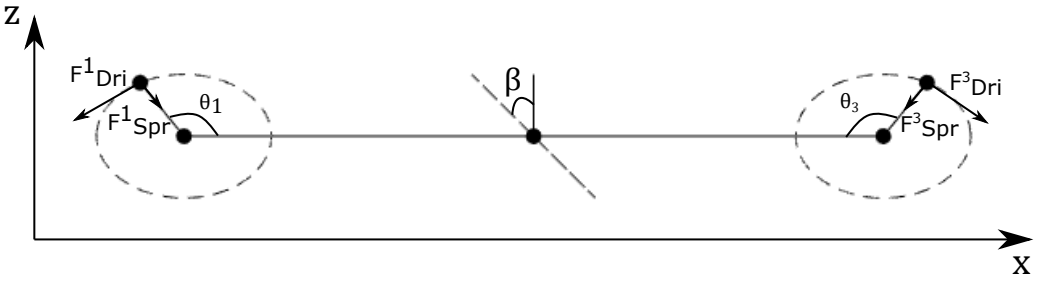
Figure 3.22: End Phase Difference over twenty beads in a bead spring model as we vary the orientation angle α. The graphs are coloured using a parula colour map starting at the first pair of beads with the results in blue to the final pair of beads with the results in yellow.

end effects on the cilia close to either end of the line which prevent them from staying synchronous with the rest of the cilia.

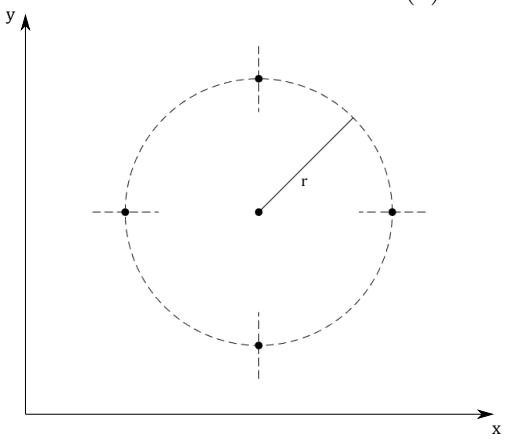
We now take a more in depth look on the effect of the angle α on the final phase difference that the system tends to. This is shown in Figure 3.22 in which we plot the end phase difference reached between neighbouring beads after a long time over the angle of orientation, α. Studying the figure we note that the phase difference for each pair of beads has some qualitative similarities to the two or three bead cases. That is that they increase up to a peak phase difference before quickly decreasing. We also see that, as in the case of three beads, this is mostly centred around the two bead case.

Studying the peak of the graphs, we note that as we move along the pairs to the right, the peak of the Phase difference occurs for increasing angle α. We also note that it does not increase steadily to this peak. Instead, it remains fairly constant until a sharp increase at approximately $\alpha = \pi/10$. However, it is unclear as to why this sharp increase occurs. It then steadily increases towards its peak.

With our models for twenty beads we again see results that are somewhat spread



(a) Side View



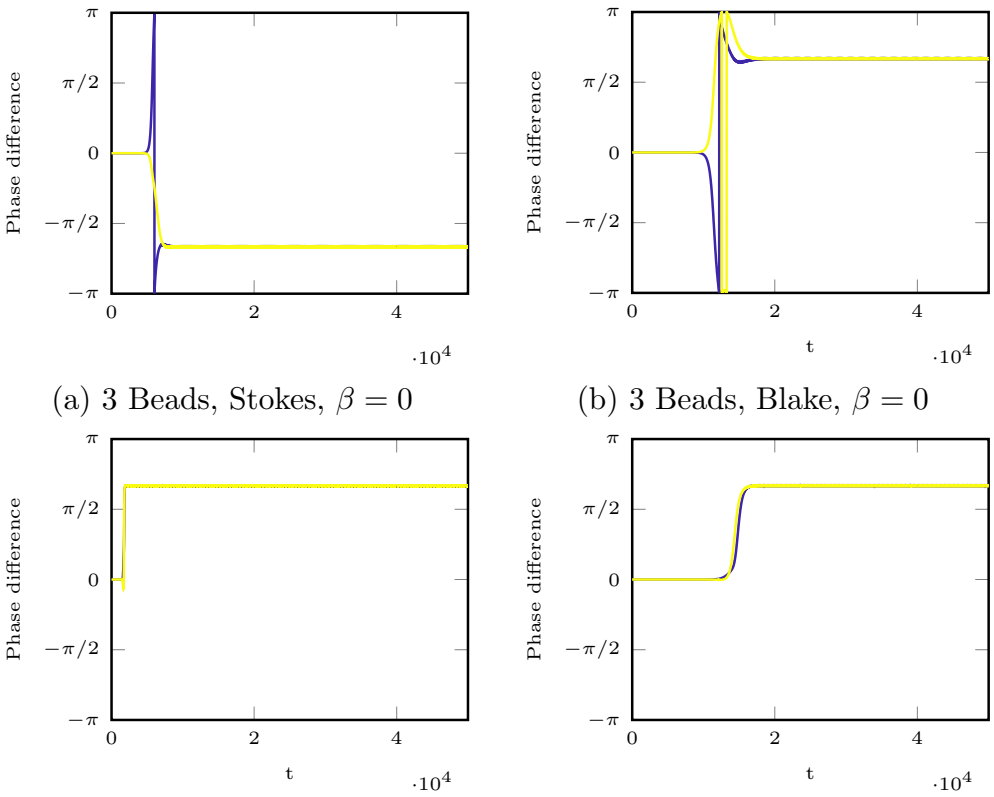
(b) Top Down View

Figure 3.23: Schematic showing the setup and variables for our bead and spring model around a circle with the beads beating out from the centre of the circle. Panel (a) shows a side on view while Panel (b) shows a top down view. In Panel (a), we show the phase difference of the beads denoted by θ_i, as well as the Forces acting on the beads as $\boldsymbol{F^i_{Dri}}$ and $\boldsymbol{F^i_{Spr}}$. We also show the orientation angle of the trajectory β measured from the z direction. In Panel (b), we show the radius of the circle the beads are arranged in denoted by r.

around the results for the two bead case. As previously discussed for the 3 bead case, we predict that this occurs due to an imbalance in the cilia either side of the pair. We now go on to modelling the flagella beating positioned around a circle. In this geometry, we expect that we may be able to obtain a synchronous or metachronal wave as a steady state. That is because we no longer have a start and end point for the group of cilia so we do not see this imbalance that we saw for cilia in a line.

3.2.4 Bead and Spring Model Around a Circle

Our earlier studies on the bead and spring model consider the beads arranged in a straight line. However, for real microswimmers, their flagella would often be placed over a sphere



(a) 3 Beads, Stokes, $\beta = 0$

(b) 3 Beads, Blake, $\beta = 0$

(c) 3 Beads, Stokes, $\beta = \pi/4$

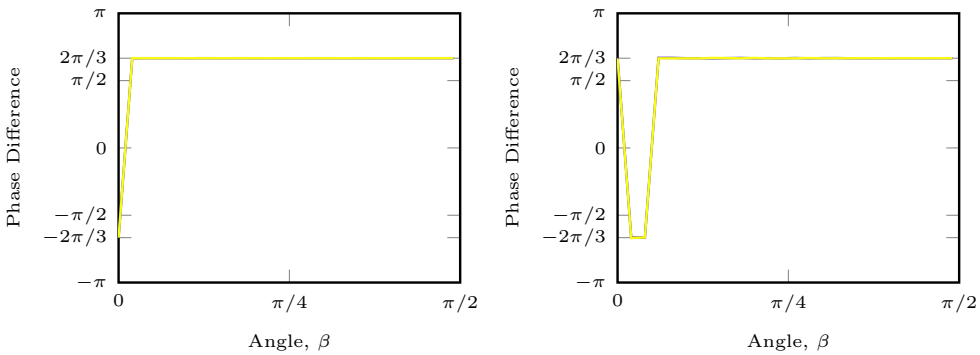
(d) 3 Beads, Blake, $\beta = \pi/4$

Figure 3.24: Phase difference over time between three neighbouring beads arranged equidistantly around a circle of radius $r = 5$ as part of the bead and spring model for both Stokeslets and Blakelets with $\beta = 0$ and $\beta = \pi/4$. The springs here have natural length $l = 0.5$.

such as is seen on *Paramecium* (Machemer, 1972) or around a circle such as on *Didinium* (Small et al., 1971). Therefore, we test our bead and spring model to study how they synchronise with each other when positioned around a circle. We present a schematic for how we set up the beads in the model and the variables that we use in Figure 3.23.

We initially consider the model around a circle of radius $r = 5$ for three beads considering the effects of both Stokeslets and Blakelets. Results for the change in phase difference between the neighbouring beads over time with $\beta = 0$ and $\beta = \pi/4$ is given in Figure 3.24 for both Stokeslets and Blakelets.

Studying the plots in Figure 3.24 we see fairly similar behaviour in each case. In all cases the system starts by remaining at a phase difference of zero implying that the beads beating synchronously is a meta-stable steady state. We also then in each case see the



(a) Stokeslet (b) Blakelet

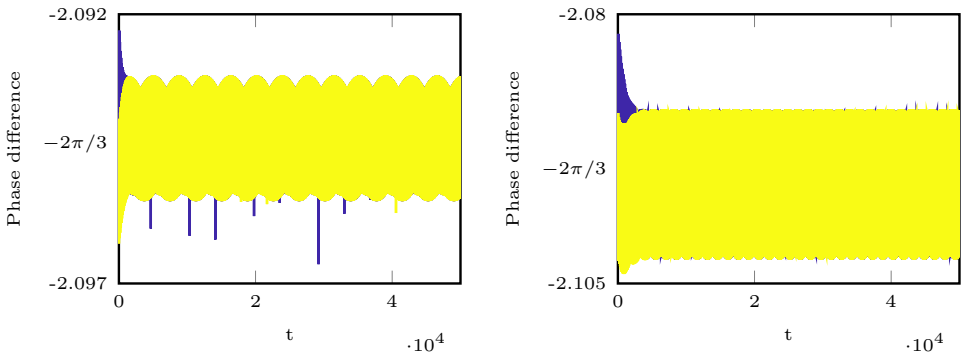
Figure 3.25: End Phase difference over three beads arranged around a circle of radius $r = 5$ of a bead and spring model over the angle β.

system move towards a metachronal wave. This metachronal wave has a phase difference of $2\pi/3$ in 3 of the cases or $-2\pi/3$ for $\beta = 0$ with the beads modelled as Stokeslets. Therefore we have stable fixed points with a wave number of 1 or -1. Comparing the Stokeslet and Blakelet cases, we note that the presence of a wall appears to keep the system in the synchronous steady state with a phase difference of 0 for a much longer time-frame before moving away.

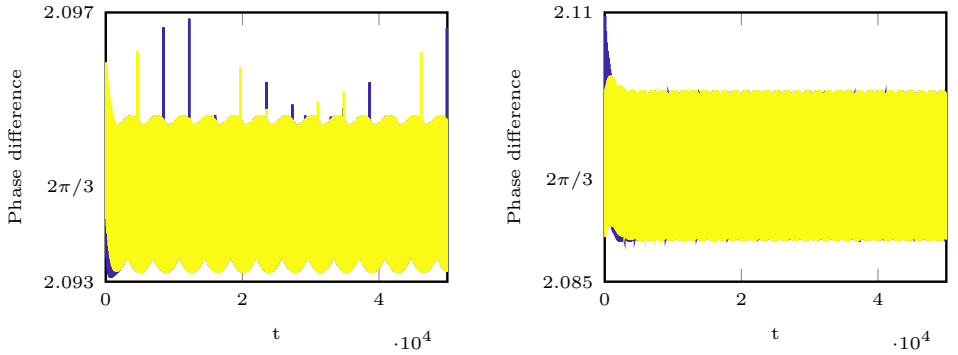
We next consider how varying the angle β affects the stable steady steady state that the system moves to for both Stokeslets and Blakelets. This is shown in Figure 3.25 in which we show the end phase difference reached by the system after a long time over the angle β. Here we see that for for all angles in both Stokeslets and Blakelets the system tends towards a metachronal wave with a phase difference of $\pm 2\pi/3$.

In Figure 3.25, we note that in the case of both Stokeslets and Blakelets there does not appear to be a pattern to explain whether the steady state the system tends to is a symplectic (positive) or antiplectic (negative) metachronal wave. Therefore, we suggest the hypothesis that both $\pm 2\pi/3$ are steady states of system for all angles β.

To test this hypothesis, we consider the case of $\beta = 0$. We then see how the system behaves when starting at a phase difference of $\pm 2\pi/3$ for both Stokeslets and Blakelets. The phase difference over time starting at these initial phase differences are shown in Figure 3.26. Here we see that for each case the system oscillates around the initial phase

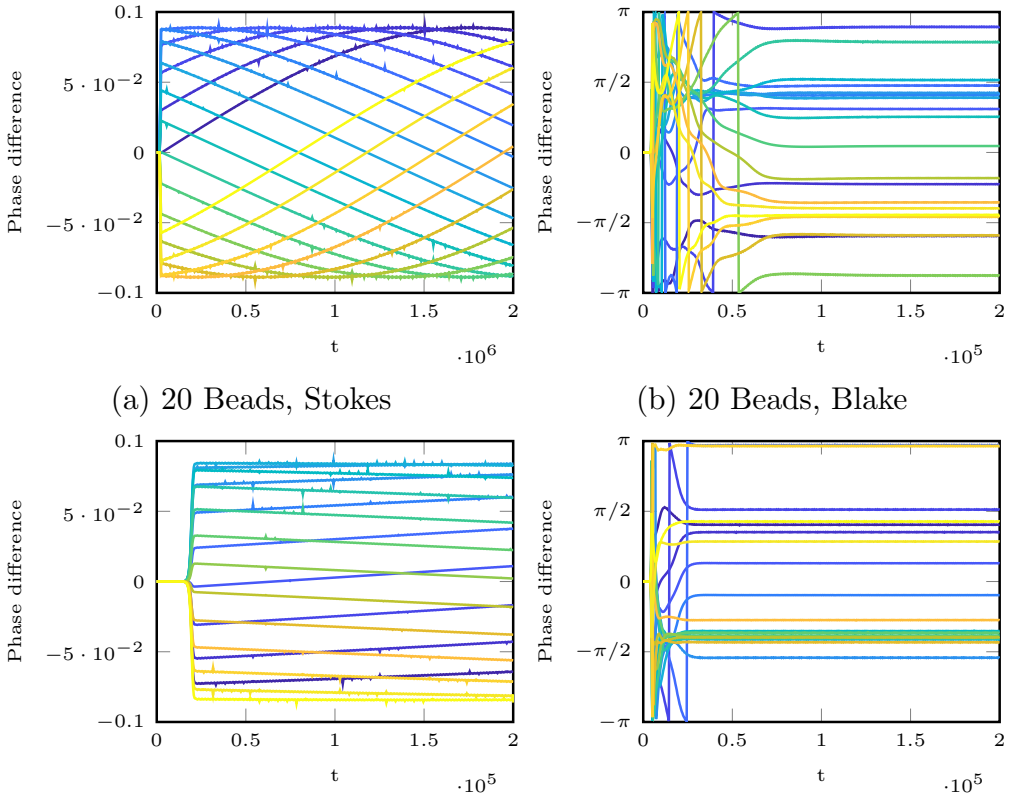


(a) Stokes, Phase=$-2\pi/3$ (b) Blake, Phase=$-2\pi/3$



(c) Stokes, Phase=$2\pi/3$ (d) Blake, Phase=$2\pi/3$

Figure 3.26: Figure showing steady states for 3 Beads in a circle of radius $r = 5$ for $\beta = 0$. We show the phase difference over time for an initial Phase Difference of $\pm 2\pi/3$ for both Stokeslets and Blakelets where we see that these are stable fixed points.



(a) 20 Beads, Stokes

(b) 20 Beads, Blake

(c) 21 Beads, Stokes

(d) 21 Beads Blake

Figure 3.27: Phase difference over time between twenty (Panels (a) and (b)) and twenty one (Panels (c) and (d)) neighbouring beads arranged in a circle of radius $r = 8$ as part of the bead and spring model for both Stokeslets and Blakelets with $\beta = 0$. The springs have natural length of $l = 0.5$. We note that Panel (a) for twenty beads modelled with Stokeslets is plotted over a much longer time frame than the other panels.

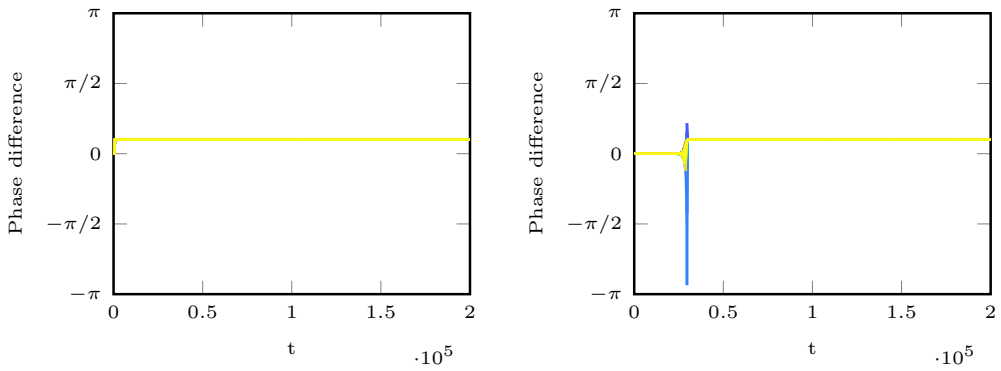
difference of $\pm 2\pi/3$ remaining very close to these points. Therefore, we can say that for $\beta = 0$ the system with both Blakelets and Stokeslets is bistable with two stable fixed points giving a metachronal wave with a wave number of ± 1 as well as a metastable fixed point at a phase difference of zero for synchronous beating.

We next wish to consider how an increased number of beads around the circle affects the behaviour of the system. Therefore, we now study the model with twenty and twenty one beads around a circle. We test these amounts of beads to study the effect of a larger number of beads as well as studying if having an even or odd number of beads has an effect on the behaviour of the system. For $\beta = 0$ the beads beat away from the centre of the circle. The phase difference between neighbouring beads over time for this case are shown

in Figure 3.27 with an initial phase difference of 0 for both Stokeslets and Blakelets. We can initially note that there is a meta-stable fixed point at a phase difference of 0 between the beads as in the case of three beads. The system is shown to stay at this point for a long time until it is moved far enough away due to numerical noise. This is the case for both twenty and twenty one beads those is not as clear to see on in Panel (a) due to the longer time frame that is plotted for in Panel (a).

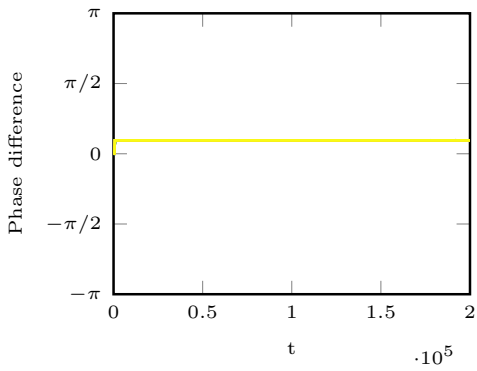
We compare twenty and twenty one beads to study if there is any influence on how the system behaves due to containing an odd or even number of beads. Studying the plots we find that the number of beads being odd or even does not appear to be a significant factor in the systems behaviour. The perceived slight difference in the plots in Panels (a) and (c) is due to the larger time scale that is plotted Panel (a) to understand the effects over a long time. There is however, a significant effect produced by including a wall modelling the beads using Blakelets. Without a wall, the phase difference of neighbouring beads remains small, changing in a wavelike pattern between a phase difference of ± 0.1. This wavelike pattern is happening over a very long timeframe, though it appears clear that this periodic wavelike change in the phase difference between flagella is stable. This is a very interesting and unexpected result for which we are currently unable to explain why this might occur. However, when introducing a wall, the behaviour of the beads appears to be fairly chaotic with a large seemingly almost random array of phase differences between neighbouring beads.

Next, we consider the system of twenty and twenty one beads around a circle of radius $r = 8$ with an angle $\beta = \pi/4$. We show the phase difference over time for this case for both Stokeslets and Blakelets in Figure 3.28. With a non-zero angle the system is found to reach a stable steady state. For each example of 20 and 21 beads with both Stokeslets and Blakelets this steady state is found to be a positive metachronal wave. For twenty beads this metachronal wave has a phase difference between the beads of $2\pi/20$ and they have a phase difference of $2\pi/21$ for the system with twenty one beads. Therefore in both cases we find that a metachronal wave with a wave number of 1 is a stable steady state.

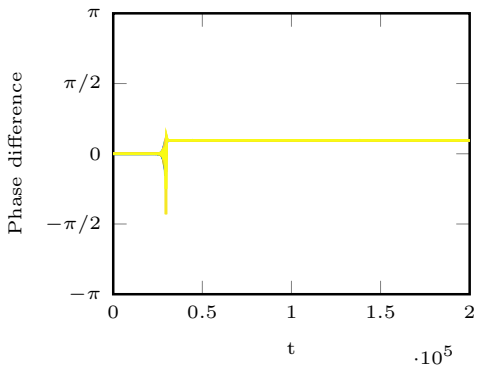


(a) 20 Beads, Stokes

(b) 20 Beads, Blake

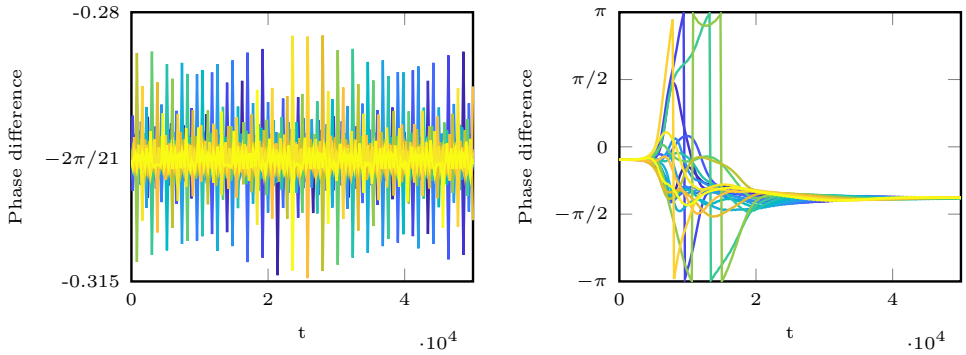


(c) 21 Beads, Stokes

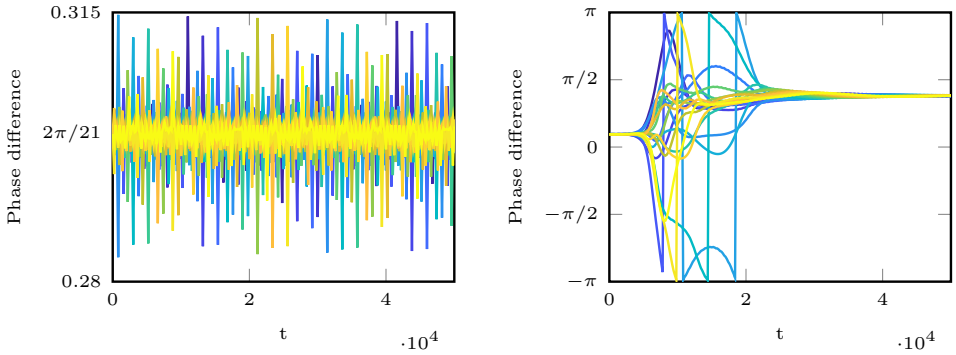


(d) 21 Beads Blake

Figure 3.28: Phase difference over time between twenty (Panels (a) and (b)) and twenty one (Panels (c) and (d)) neighbouring beads arranged in a circle of radius $r = 8$ as part of the bead and spring model for both Stokeslets and Blakelets with $\beta = \pi/4$.



(a) Stokes, Phase=$-2\pi/21$ (b) Blake, Phase=$-2\pi/21$



(c) Stokes, Phase=$2\pi/21$ (d) Blake, Phase=$2\pi/21$

Figure 3.29: Figure showing steady states for 21 Beads in a circle of radius $r = 8$ for $\beta = 0$. This shows the phase difference over time for Phase Difference of $\pm 2\pi/21$ for both Stokeslets and Blakelets.

As with the three bead case, we find that a phase difference of 0 is metastable fixed point but only in the case of Blakelets.

Studying our earlier results for beads around a circle, we can notice some similar behaviour between each of our models. The beads being arranged in a circle appears to make a metachronal wave a stable fixed point. In each of the cases studied so far, where we have a metachronal wave, it has had a metachronal wave number of ± 1. However, with our initial study of twenty and twenty one beads around a circle with $\beta = 0$ we were unable to find a stable fixed point when starting with synchronous beads with an initial phase difference of 0. We now wish to use our knowledge found from the other cases to try and find a stable fixed point.

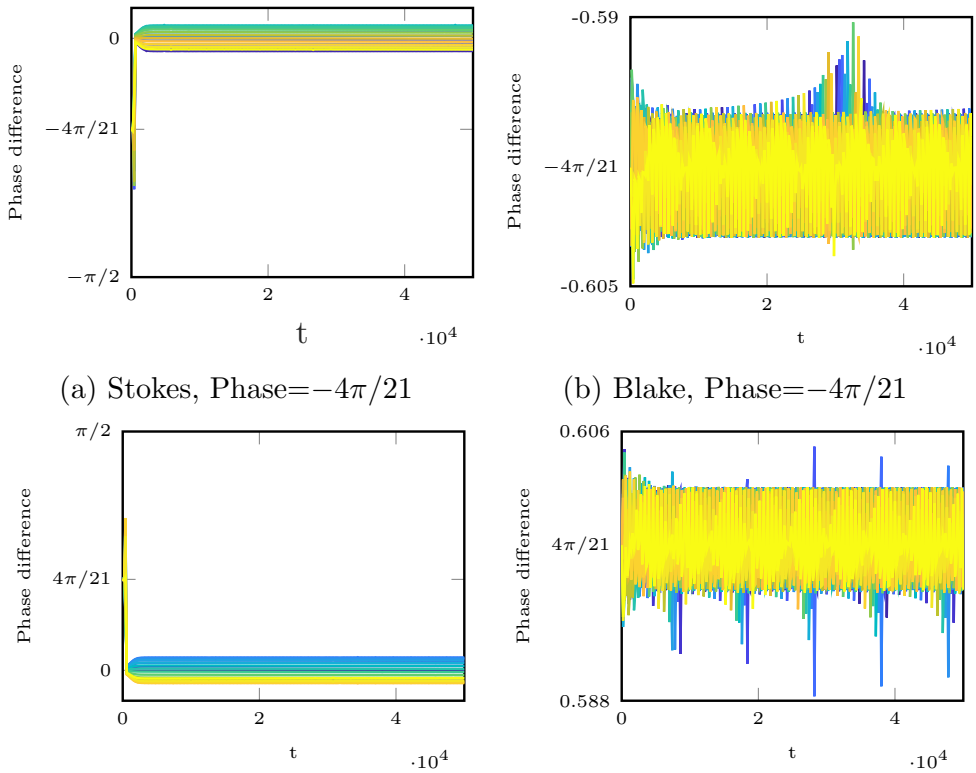
We look at simulations to try and find stable fixed points for twenty one beads with similar behaviour being found for twenty beads. We show these results in Figure 3.29. In

this figure, we test the the twenty one bead case by starting the system in a metachronal wave with an initial phase difference of $\pm 2\pi/21$ between each neighbouring pair of beads giving a metachronal number of ± 1. We study these results for both Stokeslets and Blakelets.

For Stokeslets we see results that we would expect with both phase differences of $\pm 2\pi/21$ being found to be stable fixed points. However it is clear from Figure 3.27 that these are very weakly stable for $\beta = 0$. This could be because at $\beta = 0$ the beads are unable to push each other along effectively making it struggle to quickly reach a stable steady state. We can also note that generally the system appears to prefer moving towards a symplectic metachronal wave compared to an antiplectic wave. This implies that in general the symplectic wave is more strongly stable with a wider basin of attraction.

In the case of Blakelets for twenty one beads around a circle for $\beta = 0$, we find a surprising result. Here the presence of a wall has made the metachronal wave with a wave number of one no longer a stable steady state. Instead we find that the system goes towards a different metachronal wave that has a wave number of greater magnitude. This metachronal wave has a phase difference between the cilia of approximately $\pm 8\pi/21$ or a wave number of ± 4 These results are also found to be similar for twenty beads. However, for twenty beads modelled as Blakelets, the fixed point is found to be more weakly stable only reaching it when starting closer to it.

We also study if larger integer wave numbers give stable steady states. We show results of the phase difference over time for an initial phase difference of $\pm 4\pi/21$ in Figure 3.30. Here we find that the Blakelet case with a wall present shows that a metachronal wave number of ± 2 is a stable steady state. We also find that this is true for larger integer wave numbers. However, for the Stokeslets case, integer metachronal wave numbers greater than one are found to be unstable. The system goes to the same state as when starting with a phase difference of 0.



(a) Stokes, Phase=$-4\pi/21$

(b) Blake, Phase=$-4\pi/21$

(c) Stokes, Phase=$4\pi/21$

(d) Blake, Phase=$4\pi/21$

Figure 3.30: Figure showing steady states for 21 Beads in a circle of radius $r = 8$ for $\beta = 0$. This shows the phase difference over time for an initial Phase Difference of $\pm 4\pi/21$ for both Stokeslets and Blakelets.

3.3 Summary

In this chapter we have taken an in depth study into the metachronal wave. We first considered the efficiency of various types of metachronal wave. Here the optimal phase difference producing the largest flux was found for an antiplectic metachronal wave. Other interesting results that we found as part of this study is that the metachronal wave produces its own pumping effect. In studying the flux produced when $\alpha = \pi/2$ and the cilia are beating perpendicular to the metachronal wave direction, the flux perpendicular to the wave direction was not found to be zero, showing that the metachronal wave has an effect on the flux produced. We also found when studying single regularised force models that these results matched qualitatively very well with our full cilium models.

Since our results for the prescribed force models do not fully match with what is seen in nature for metachronal waves, we took a further look into how cilia synchronise with each other to form into a metachronal wave using a bead and spring model. For the cilia arranged in a line we found that when increasing the distance between cilia, there was an optimal distance of approximately $d = 3$. When studying more than two beads arranged in a line, we found that the results were centred around the results of the two bead case. We suspect that this is related to position of the end points of the line of cilia. This is somewhat seen as we increase the number of cilia where we saw a steepening travelling wave emerge for the results of twenty beads in a line. It could be interesting to take this study further to model at what point this transition to a travelling wave occurs.

We found that to form into a metachronal wave for our model, the beads had to be arranged around a circle rather than next to each other in a line. For beads arranged in a circle it was found that both symplectic and antiplectic waves were stable fixed points. However, when starting at a fully synchronous beat, the beads most commonly reached the symplectic steady state suggesting that it is more strongly stable. Hence this could be a reason why metachronal waves in nature are most often found to be symplectic. We also found that the system of beads around a circle can struggle to reach this metachronal steady state when $\beta = 0$. This result can often be seen in nature in which their flagella are

often tilted by a certain amount such as in many of the Volvocine Green algae or Didinium. An interesting result was found here with twenty and twenty one beads around a circle when $\beta = 0$. This was that we found a steady state where the phase difference between neighbouring cilia varied in wavelike pattern between a phase difference of ± 0.1.

We next go on to study the swimming behaviour of various biological microswimmers many of which are often found to have a metachronal wave over their flagella when swimming. We do this first for prescribed kinematics with a full cilium model in Chapter 4, and then with a simplified bead-spring fluid structure interaction model in Chapter 5, comparing the results.

CHAPTER 4

THE ALGAL COLONY SUITE

4.1 Motile Green Algae

An algal colony is an organism that is made up of a group of algal cells. In this section, we are interested in a particular group of algal colonies known as Volvocine green algae that derive from *Chlamydomonas*. This ranges from the single celled *Chlamydomonas* to the multicellular *Volvox* with thousands of cells (Coleman, 2012). The group also contains colony sizes in between this made up of a few cells.

This range of colony sizes makes the Volvocine green algae model organisms for studying the transition to multicellularity. One feature that makes them useful for studying multicellularity, is the distinction of cell types. Most of the Volvocine algae have one type of cell, except for *Volvox* which contains two distinct types of cell (Goldstein, 2015). These are somatic and germ cells with the colony containing a much higher number of somatic cells. Germ cells are those that are focused on reproduction, and somatic cells are the rest that build up the organism but they do not aid in reproduction. Therefore we can use this group of algae to study when multicellular colonies start requiring cells with different functions and why this might be.

A large amount of the work on the swimming of Volvocine Green algae has focused on studying either the smallest organism, *Chlamydomonas*, or the largest organism, *Volvox*. For *Chlamydomonas*, its swimming behaviour has been extensively studied in both ex-

periments and mathematical models. *Chlamydomonas* is therefore often used as a model organism for swimming at the microscale (Goldstein, 2015). One area of interest for *Chlamydomonas* is how it detects and moves towards light as part of phototaxis (Arrieta et al., 2017). For its ability to move towards light, many people have studied how it is able to steer (Leptos et al., 2018). For example, for phototaxis, Leptos et al. (2018) consider the process of how *Chlamydomonas* uses its eyespot to detect the light and then how the flagella beat changes to steer it towards this light. Other papers consider how the swimmer can steer more generally. For example, Stocker and Durham (2009) considers *Chlamydomonas* using an antiphase beat to orient itself in a eukaryotic run and tumble fashion. A more in depth look at the swimming behaviour of *Chlamydomonas* with different beating patterns including antiphase has also been considered (Leptos et al., 2013).

Another large area of research into *Chlamydomonas* considers it as part of suspensions rather than the individual swimmer. For example, O'Malley and Bees (2012) looks at the orientation of groups *Chalmydomonas* cells in shear flows considering gravitaxis and gyrotaxis (how the cells reorient from the viscous and gravitational torques). *Chlamydomonas* experiences negative gravitaxis meaning the cells typically swim upwards against gravity.

As with *Chlamydomonas*, a lot of work has been done on steering in *Volvox* such as in part of phototaxis (Solari et al., 2011). Some of this work has investigated how the cells of *Volvox* communicate with each other to organise the flagella beat in order to steer. This organisation between the flagella is also observed and studied during its regular beating in which the beating flagella often form a metachronal wave (Brumley et al., 2015). It has also been studied as to how the *Volvox* flagella produce this metachronal wave hydrodynamically (Brumley et al., 2015). Due to this metachronal wave, models of the swimming of *Volvox*, often use a squirmer model (Pedley et al., 2016).

In this chapter, we model the swimming behaviour of some of the Volvocine green algae. Their swimming behaviour will be compared for different swimming gaits as well as comparing different swimmers to each other. Using the level set method as introduced

in Section 2.3 (In particular we use the multicellular version in equation (2.33)), we will model the complex geometry of the swimmers body and model the waveform using one of the two previously discussed flagella waveform models as given in Section 2.4. The swimming behaviour is then calculated using the Nearest Neighbour method as is presented in Section 2.2. The work in this chapter is in progress to be prepared to be submitted to a peer reviewed journal.

To implement our model, we have developed the Algal Colony Suite. This is an app that is capable of simply modelling a swimmer using the level set method and previously discussed waveform models. It is then able to calculate the swimming behaviour using the Nearest Neighbour method.

This app is designed to be used by experimental biologists that will not necessarily have a lot of mathematical or coding experience. They would use images of the swimmer they wish to model and analyse them to recreate the swimmer as accurately as possible. This would enable them to efficiently use mathematical modelling and experimental methods alongside each other to further their research. We have used this app in creating the models for Volvocine green algae shown in Figure 1.7. These are *Chlamydomonas*, *Tetrabaena*, *Gonium*, *Pandorina*, *Eudorina* and *Pleodorina* that are discussed in the Volvocine green algae results section. More details on this app will be discussed in the next section.

4.2 The Algal Colony Suite

To simply build swimmers and use the Nearest Neighbour method to calculate their swimming behaviour, we develop the Algal Colony Suite. This is an easy to use app, in which you can build a swimmer made up of ellipsoidal cells and calculate its swimming behaviour with Nearest Neighbour method. This can enable people from a wide range of scientific backgrounds to make simulations of the swimming of various microswimmers.

We show the title page that appears when opening the app in Figure 4.1. The app has been used to build all of the level set discretisations of the Algal Colony Swimmers

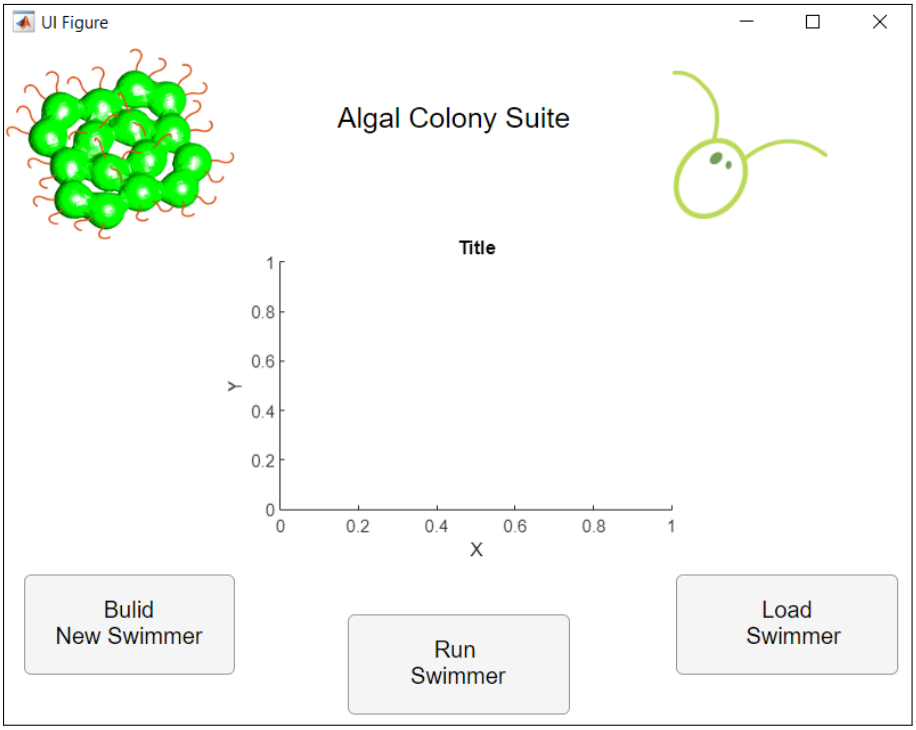


Figure 4.1: Screenshot showing the title page for the app titled algal colony suite. The three buttons allow you to build a swimmer model up in the app, load a saved model and run the currently loaded swimmer to find its swimming behaviour.

used for the results of this thesis. These are able to be loaded into the app using the 'Load Swimmer' button and the smaller swimmers are able to be run through the code to find their swimming behaviour by clicking on the 'Run Swimmer' button. For the larger swimmers, the app can output a file describing the swimmer model which can then be sent to a High Performance Computing (HPC) cluster to run the model through the code. For our larger swimmers, we sent them to the HPC cluster Bluebear.

As well as these prebuilt swimmers, the app also allows the user to create their own models of microswimmers. For this, they open the 'Build New Swimmer' section from the title page to be able to create the geometry of their swimmer. The first step to creating their swimmer is to build its body. We present a screenshot of the section of the app used to build the bodies of the swimmers in Figure 4.2. The body is built by defining each cell individually. For each cell, define the centre and the size of each semiaxes for the ellipsoidal cell. For ellipsoidal cells, they can also define the cells planar rotation angle.

In describing the body of the swimmer, we can also take advantage of reflective or

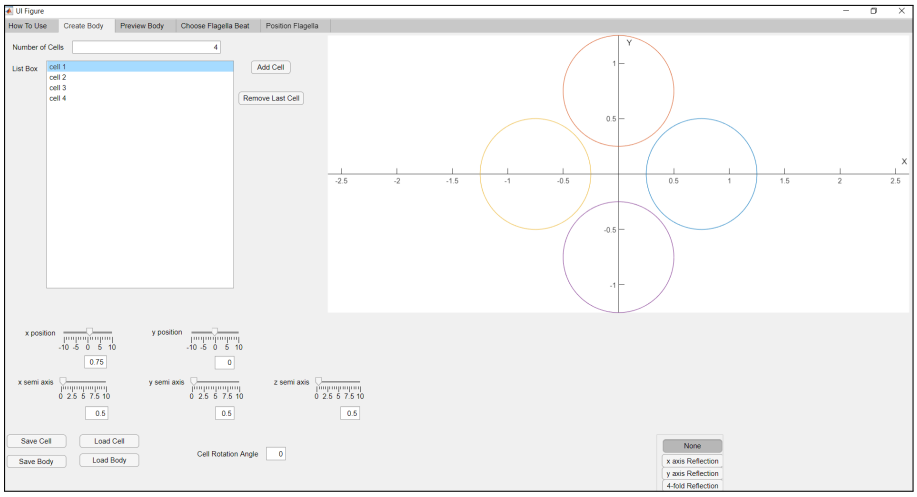


Figure 4.2: Screenshot showing the section of the app for creating the body of the swimmer. The sliders allow you to control the size and position of the cells. The buttons in the bottom right allow you to add the reflections of the currently created cells. This includes the reflection in the x axis, reflection in the y axis and a 4 fold reflection.

rotational symmetry that the swimmer may have. We can use this symmetry to only have to define the dimensions of a few of the cells. We can then reflect or rotate these cells to find the variables to describe the cells in the rest of the body. This enables us to build swimmers that contain symmetries faster. To discretise the body of the swimmer, we use the level set method as described previously.

The next step is to create and position the flagella on the body of the swimmer. We show the page of the app used to position the flagella in Figure 4.3. For the flagella, the user will first choose the flagellar waveform that they will use for the flagella of their swimmer. Finally, once the flagellar waveform has been defined, we then position the flagella on the cell. For this, the user can choose which cell the flagella is on, its orientation (such as whether it is 'Cis' or 'Trans') and define the position of the flagella on the cell in polar coordinates localised to the cell. To allow for nonsynchronous flagella, such as for the metachronal wave that we will model for *Gonium* and *Pleodorina*, you can also define at which point the flagella will start its beat. Once the swimmer has been created, it can then be saved and run through the code to obtain information about its swimming behaviour.

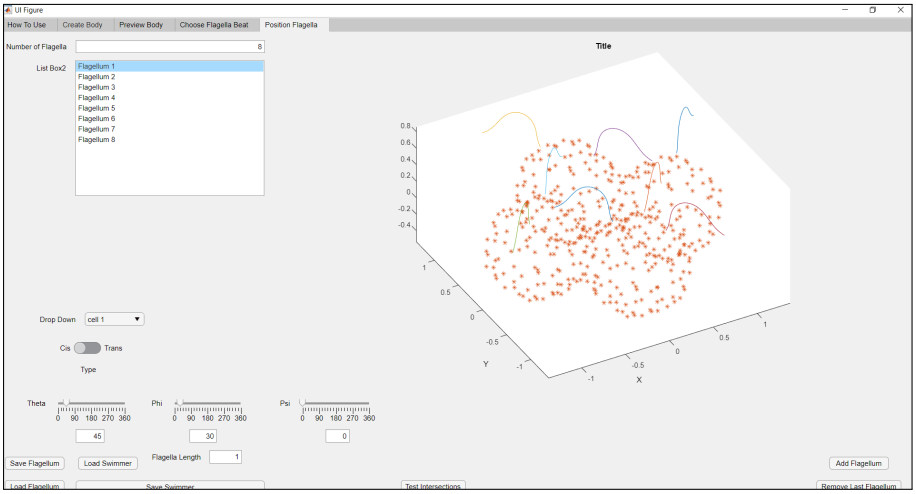


Figure 4.3: Screenshot showing the section of the app for positioning the flagella on the body. The sliders position the flagella on the cell using localised polar coordinates.

4.3 Convergence

To ensure that the methods used for modelling the swimming of algal colonies are valid, we need to consider the convergence of the methods used. We test these methods for the convergence of a swimming *Chlamydomonas* cell. Since this is smallest of the Volvocine green algae and is similar to the cells of the larger colonies, we assume that if our method converges for *Chlamydomonas* then it will converge for all of the Volvocine green algae, provided we maintain the same resolution for each cell.

For testing the convergence we considered the nondimensional total displacement in the z direction (the direction of most of its movement) over one flagella beat. We tested the convergence of this value for an increasingly fine set of points. The number of points modelling the swimmer was increased in two different ways. The first of these was increasing the number of quadrature points on the flagella keeping the number of force and quadrature points on the body constant. We do this for both models of the flagella waveform. The next considered increasing the number of quadrature points of the body of the swimmer.

In Figure 4.4, we see the convergence testing results for an increasing number of quadrature points on the cilia with the waveform taken from Gallagher and Smith (2018) where we plot the z displacement over the number quadrature points on the cilia for 20,

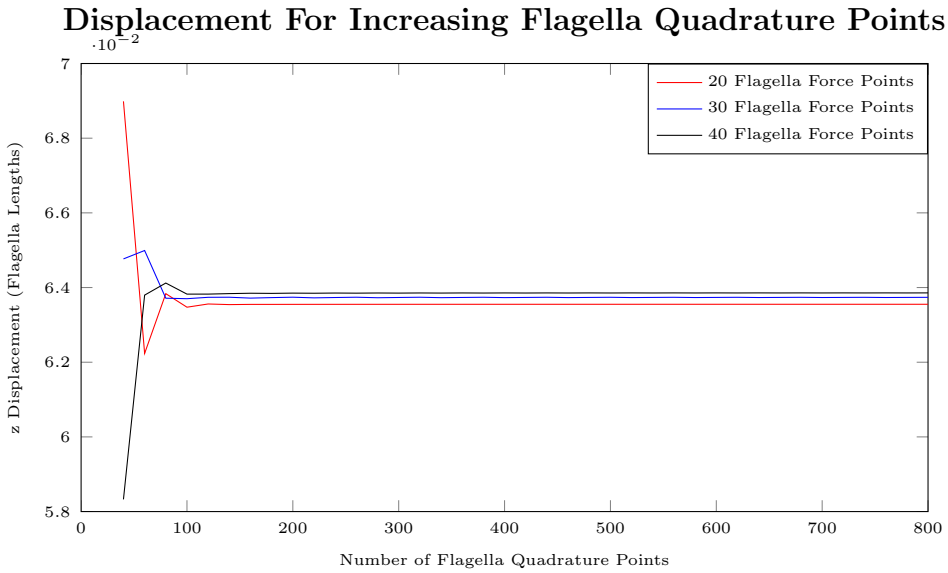


Figure 4.4: Figure showing how the displacement by *Chlamydomonas* changes for an increasing number of quadrature points on the flagella with the waveform given in equation (2.35) taken from Gallagher and Smith (2018). This is shown for three set values of the number of Force points. Red - 20 Force points, Blue - 30 Force Points and Black - 40 Force Points.

30 and 40 force points on the cilia. We can see that the displacement of the centre of the cell body after one flagella beat by *Chlamydomonas* becomes closer to each other as the number of quadrature points on the flagella increases for each number of force points. We can also see that the displacement tends to approximately the same value for each set of force points as the number of quadrature points increases. This suggests a convergence of the swimming for an increasing number of quadrature points on the flagella. We can also see that there is very little change in the result for the displacement of *Chlamydomonas* when comparing for 20, 30 and 40 force points on the flagella. Due to this minimal difference, we will use 20 force points and 200 quadrature points on the flagella in our analysis of the Volvocine green algae, since this will result in far fewer degrees of freedom when considering *Pleodorina*, which has 128 flagella.

To look in more detail about how this converges we look at the percentage change between the displacement from the current number of the quadrature points on the flagella and that obtained from doubling it. Considering the data shown in Figure 4.4, for 40 force points, the percentage change in displacement from doubling a small amount of quadrature

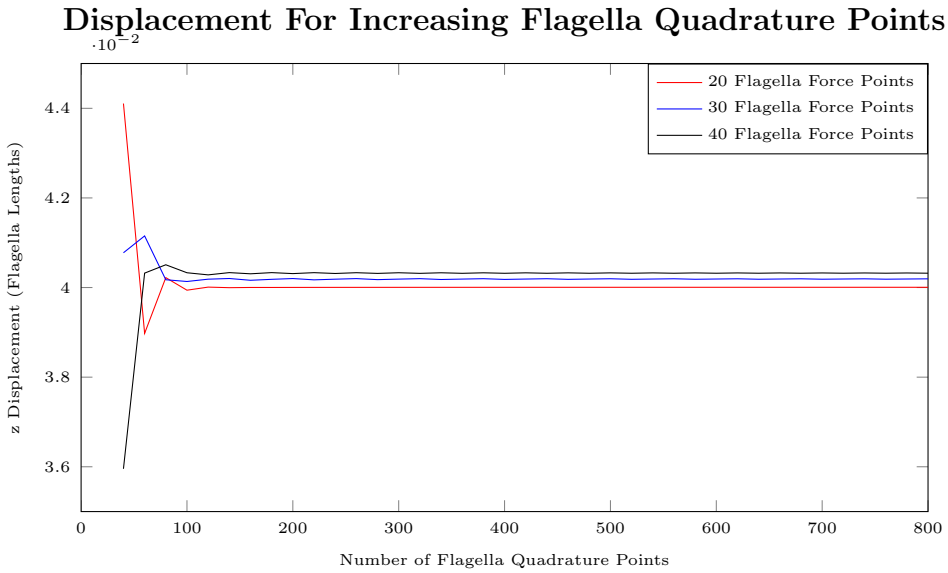


Figure 4.5: Figure showing how the displacement by *Chlamydomonas* changes for an increasing number of quadrature points on the flagella with the waveform given in equation (2.36) which was calculated by fitting to an experimental waveform. This is shown for three set values of the number of Force points. Red - 20 Force points, Blue - 30 Force Points and Black - 40 Force Points.

points representing the flagella from 80 to 160 is found to be approximately -0.4259% to 4 decimal places. For a large number of quadrature points doubling from 320 to 640, this percentage change decreases to approximately 0.0029% to 4 decimal places. The percentage change in doubling the number of points is small and decreases as the number of points increases which suggests that the method converges for an increasing number of quadrature points on the flagella.

We also wish to test the convergence for the flagella waveform that we have modelled from experimental results of a *Volvox* flagellum with the waveform given in equation (2.36). As with the other model of the flagella waveform we consider an increasing number of quadrature points on the flagella for three values for the number of Force points (20, 30 and 40). The results for this can be seen in Figure 4.5 again showing the z displacement over the number of quadrature points on the flagella. With all three numbers of force points the graphs show convergence to approximately the same value. Therefore, as with the other waveform, we can take the number of force points on the flagella as 20 with 200 quadrature points when we calculate the swimming behaviour for the Volvocine green

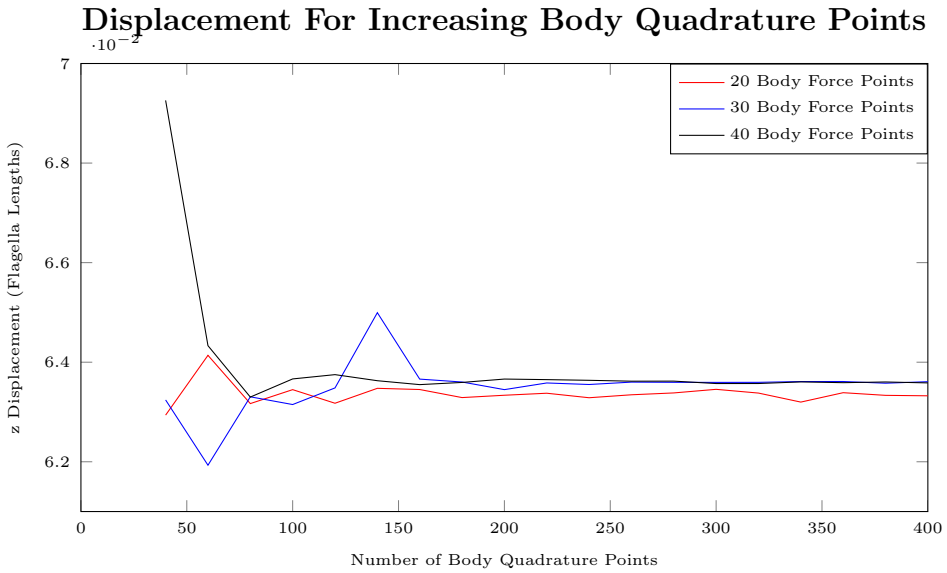


Figure 4.6: Figure showing how the displacement by *Chlamydomonas* changes for an increasing number of Quadrature points on the body of the swimmer for three set values of the number of Force points. Red - 20 Force points, Blue - 30 Force Points and Black - 40 Force Points.

algae.

As with the other flagellar waveform, we will look at the percentage change between the displacement from the current number of the quadrature points on the flagella and that obtained from doubling it. Again we consider the data for 40 Force points on the flagella. From the data in Figure 4.5, we find that the percentage change in displacement from doubling a small amount of quadrature points representing the flagella from 80 to 160 is found to be approximately -0.4974% to 4 decimal places. For doubling a large number of quadrature points doubling from 320 to 640, this percentage change decreases to approximately 0.0070% to 4 decimal places. The percentage change in doubling the number of points is small and decreases as the number of points increases which suggests that the method converges for an increasing number of flagella points. For the remainder of the convergence tests we will be using the other flagellar waveform taken from Gallagher and Smith (2018).

The next test of convergence to consider is whether the method converges for an increasing number of Quadrature points for the body of the swimmer. We can see the

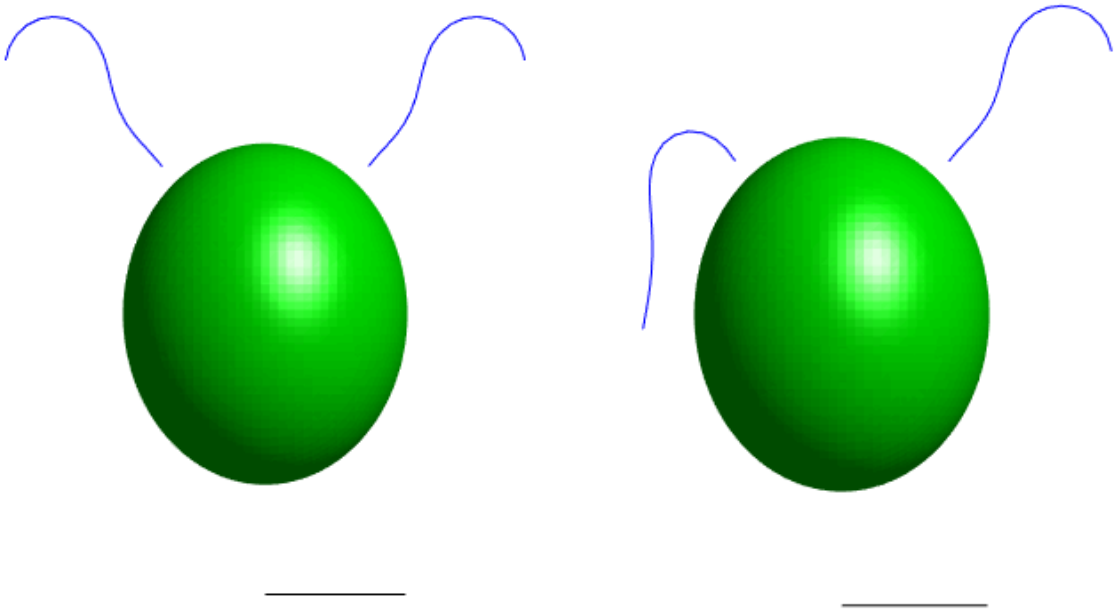
convergence results for this test in Figure 4.6, plotting the z displacement over the number of quadrature points on the body for three values of the number of Force points (20, 30 and 40). For testing the convergence for points on the body of *Chlamydomonas*, we have modelled the flagella using 40 force points and 400 quadrature points. In the Figure, we can see that for all three values of Force points on the body, that it begins to converge.

As with the number of flagella points, we wish to verify the convergence in more detail by looking at the percentage change between the displacement from the current number of the Quadrature points on the body and that obtained from doubling it. We consider the data shown in Figure 4.6 for 40 Force points and first look at the percentage change for a small number of quadrature points. We can see that doubling the number of Quadrature points from 40 to 80 gives an approximate percentage change of 8.6043% to 4 decimal places. For a large number of Quadrature points doubling from 160 to 320, this percentage change becomes approximately 0.0350% to 4 decimal places. Again this suggests that the method converges for an increasing number of quadrature points for the body of the swimmer. For our analysis of the Volvocine green algae we will be using 40 force points and 160 quadrature points.

4.4 Volvocine Green Algae Results

4.4.1 Chlamydomonas

The first swimmer we model is *Chlamydomonas reinhardtii*. This is the smallest of the Volvocine green algae with one cell and two flagella that beat in a breaststroke like motion. The cell body of *Chlamydomonas* is approximated by a prolate spheroid which we model with a vertical diameter of $12\mu m$ and a horizontal diameter of $10\mu m$ as in Gallagher and Smith (2018). *Chlamydomonas* also has two equal length flagella with a length $10-12\mu m$ and a frequency $\sim 60Hz$ (Goldstein, 2015). We study and compare two versions of this swimmer, one with a synchronised beat as shown in Figure 4.7a and the other with an



(a) Synchronous beat (b) Asynchronous beat.

Figure 4.7: Figure showing the level set surface of *Chlamydomonas* with a synchronous (a), and asynchronous (b) beat used in the Nearest neighbour method. The scale bar has length $5\mu m$.

asynchronous beat as shown in Figure 4.7b. For our model we show the displacement over one beat for flagella of length $10, 11$, and $12\mu m$ as shown in Panel (a) of Figure 4.8. We also model the flagella beat of *Chlamydomonas* using the waveform given in Gallagher and Smith (2018) which we presented in equation (2.35).

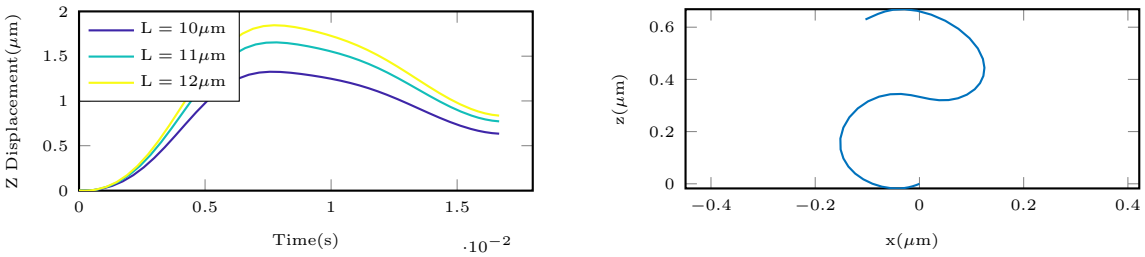
We now use the Nearest Neighbour method to calculate the swimming behaviour of our *Chlamydomonas* model for both a synchronous and an asynchronous beat. The trajectory over one beat for both of these cases is shown in Figure 4.8. We can calculate the speed from this figure by taking the distance moved after one beat and dividing it by the time taken for one beat. For the synchronous beat we find that it has a straight line velocity ranging between $38.0 - 54.7\mu m/s$ for flagella with length from $10 - 12\mu m$, with the middle point of $11\mu m$ giving a straight line velocity of $46.3\mu m/s$ as found from analysing Figure 4.8. This range contains the experimentally found velocity of *Chlamydomonas* given by $41\mu m/s$ (Chen et al., 2017). We also see here that the velocity increases non-linearly in

relation to the flagella length.

For the asynchronous beat, we just consider the flagella length of $11\mu m$ in the middle of our range. For this, we see a snaking trajectory allowing the swimmer to turn and cover a larger distance. The total distance travelled after 1 full beat is lower than that of the synchronous beating *Chlamydomonas* as would be expected. However, it is interesting to note that this distance travelled is reasonably similar to the synchronous case. That is approximately $0.77\mu m$ for the synchronous beating case with $11\mu m$ flagella compared to approximately $0.64\mu m$ for the asynchronous beat. This is possibly seen due to the lack of backwards motion during the recovery stroke portion of the flagella beat. This allows it to still travel a similar straight line distance while producing more lateral movement. A benefit of this would be for steering *Chlamydomonas*. Using an asynchronous beat could aid the swimmer in steering, for example, towards a light source for photosynthesis. A discussion on asynchronous beating in a particular mutant of *Chlamydomonas* is discussed by Leptos et al. (2013). Here they discuss a mutant which jumps between synchronous and asynchronous beating. However, the asynchronous beat is found to have a slightly different waveform to the synchronous beat as well as a higher frequency reaching approximately $82 \pm 4Hz$. Asynchronous beating is also found in regular *Chlamydomonas* swimming by Polin et al. (2009). Here they find that *Chlamydomonas* stochastically switches between synchronous and asynchronous beating. This causes the swimmer to perform an almost run and tumble style swimming with the synchronous beating causing sharp turns in its swimming trajectory.

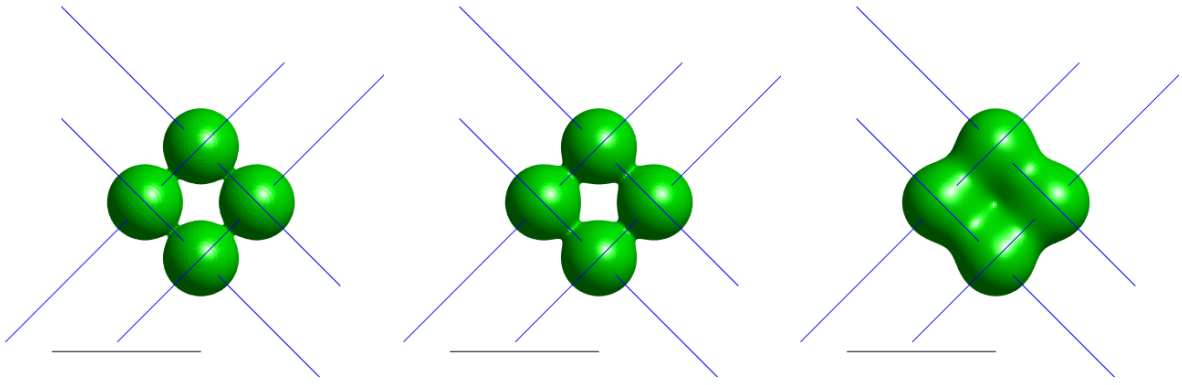
4.4.2 Tetrabaena

The next swimmer we will model is *Tetrabaena*. We show our discretisation for *Tetrabaena* with different amounts of mucilage in Figure 4.9. *Tetrabaena* has four cells which we model as each being the same size as a *Chlamydomonas* cell (Arakaki et al., 2013). For the flagella, we are unable to find experimental data on their length and frequency. However, we know this data for *Chlamydomonas* and *Gonium* which are the organisms that are



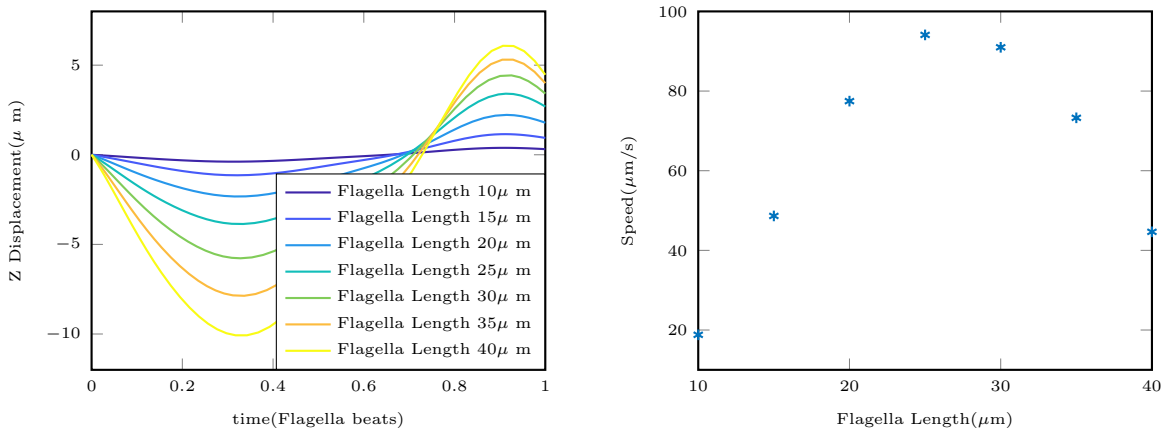
(a) Synchronous Beat (b) Asynchronous Beat

Figure 4.8: Swimming behaviour of *Chlamydomonas* over 1 beat. (a) shows the z displacement over time for a synchronous beating *Chlamydomonas* with Flagella from $10-12\mu m$ and (b) shows the trajectory of *Chlamydomonas* over one beat with an asynchronous beat with a length of $11\mu m$.



(a) Low Mucilage (b) Medium mucilage. (c) High mucilage.

Figure 4.9: Figure showing the level set surface of *Tetrabaena* with a (a) low , (b) medium and (c) high amount of mucilage used in the Nearest neighbour method. The scale bar has length $20\mu m$.



(a) Z trajectories over one beat

(b) Dimensional Speed vs Flagella Length

Figure 4.10: Figure showing the displacement and speed of *Tetrabaena* for flagella length of $10-40\mu m$. Panel (a) shows the z displacement of *Tetrabaena* for these flagella lengths and Panel (b) shows the speed of *Tetrabaena* with flagella of length $10-40\mu m$ and frequency linearly decreasing from 60 to 10 from small to large flagella starting with $60Hz$ for $10\mu m$ flagella to $10Hz$ for $40\mu m$ flagella.

closest in size to *Tetrabaena*. Respectively these have length $10-12\mu m$ and $40\mu m$ and they have frequency of $60Hz$ and $10Hz$. For *Chlamydomonas* these values were taken from Goldstein (2015) and for Gonium they were taken from de Maleprade et al. (2019). Since *Tetrabaena* falls between these two in size we investigate the effect of varying flagella on the swimming behaviour choosing different flagella lengths from $10-40\mu m$. For longer flagella to have the same energy expenditure as shorter flagella while beating, they would require a lower frequency or a different waveform. This is because the energy expenditure is proportional to both the length and frequency of the flagella. Therefore, we vary the frequency of our flagella decreasing from $60Hz$ to $10Hz$ as the flagella size increases. To model the flagella we use our model that was fitted to data given in equation (2.36). We use this model for the all the flagella of the remaining swimmers that we model in this chapter.

In Figure 4.10a, we show the z displacement over one beat for *Tetrabaena* for flagella of length $10-40\mu m$ in $5\mu m$ intervals. We see that this is a qualitatively similar shape for all the flagella lengths. However, the displacement is seen to flatten as flagella length is decreased as would be expected. We then show the calculated straight line velocity for the

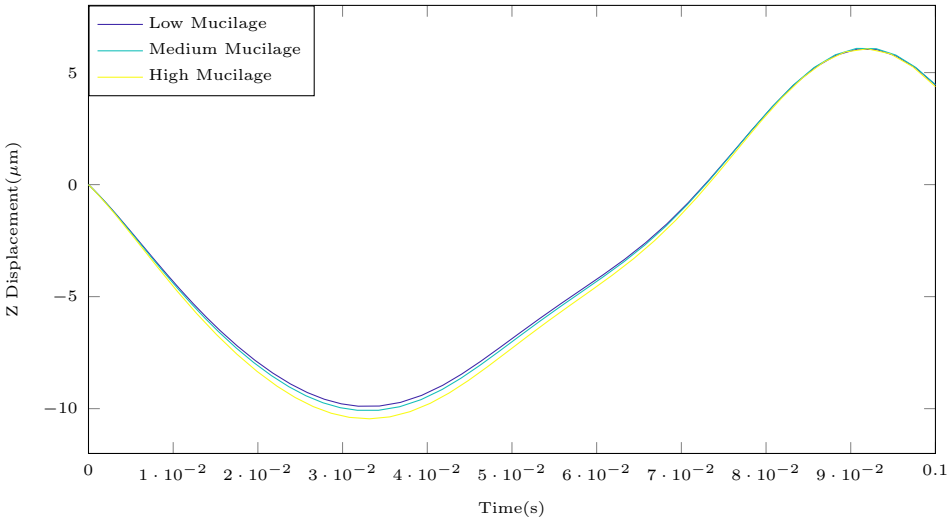
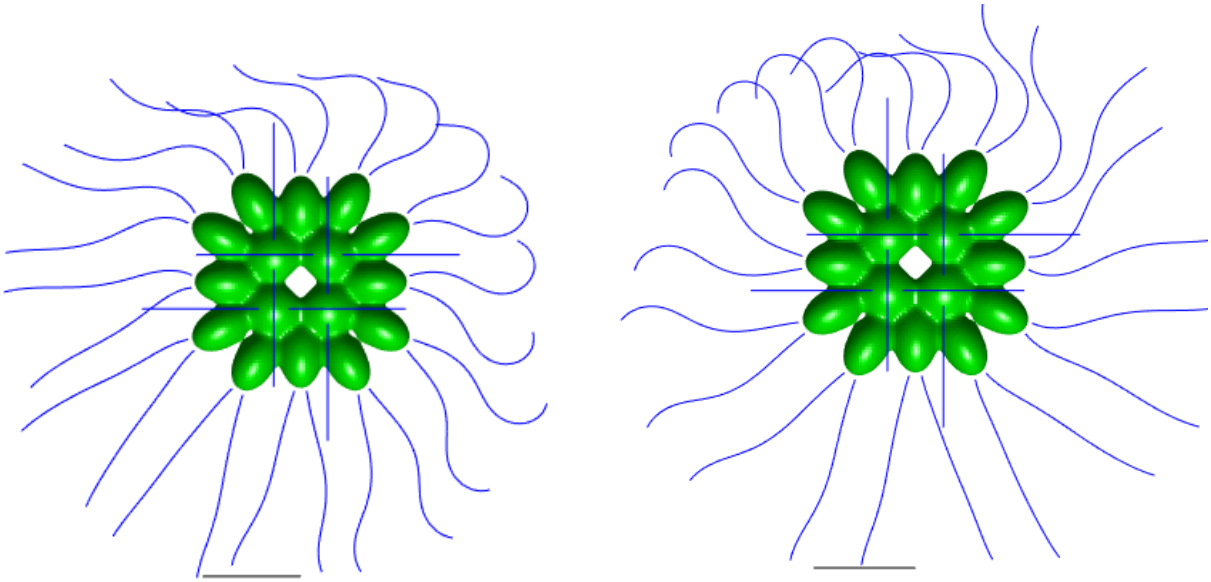


Figure 4.11: Figure showing a comparison of the swimming behaviour for *Tetrabaena* with different levels of mucilage displaying the z displacement for the swimmers. We can see that there is very minimal difference between these results.

swimmer in Figure 4.10b. To calculate the dimensional speed, we require the frequency of the flagella. For this, we take the frequency as linearly decreasing as the flagella length increases. We start with a frequency of $60Hz$ for flagella of length $10\mu m$ and go to a frequency of $10Hz$ for flagella of length $40\mu m$. We do this, since to have the same energy expenditure when beating, a longer flagella would require a lower frequency or a modified wave form. We see that the fastest *Tetrabaena* is given by a flagella length of $25\mu m$ which is calculated with a frequency of $35Hz$.

For the *Tetrabaena* with the largest flagella of length $40\mu m$, we also test the effect of different levels of mucilage between the cells, for which the swimmers are shown in Figure 4.9. We show how we vary this level of mucilage in Section 2.3. We compare the swimming behaviour for these different levels of mucilage in Figure 4.11. Here we see that the level of mucilage between the cells has a very minimal effect. The total z displacement is found to be very similar after one beat for all three levels of mucilage.



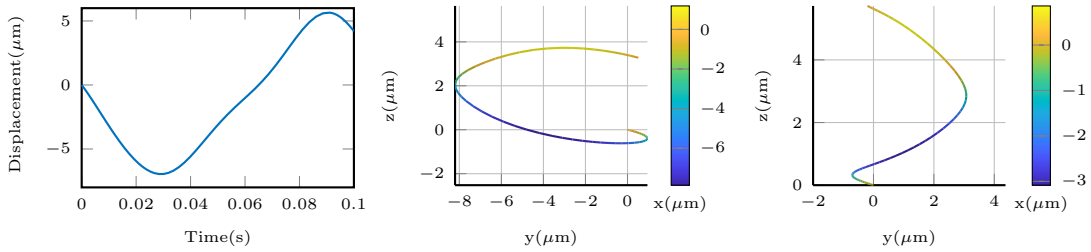
(a) Symplectic Wave (b) Antiplectic Wave

Figure 4.12: Figure showing the level set surface of *Gonium* with a metachronal wave along the peripheral flagellum used in the Nearest neighbour method. Panel (a) shows a symplectic wave and Panel (b) shows an antiplectic wave. The scale bar has length $20\mu m$.

4.4.3 Gonium

We now investigate the 16 celled swimmer *Gonium*. This is the largest of the Volvocine Green algae that is not arranged spherically. To model the swimmer, we take the cells to be similar to that of *Chlamydomonas*. We model the flagella with a length of $40\mu m$ and a frequency of $10Hz$ (de Maleprade et al., 2019). We model the swimming behaviour for *Gonium* with synchronous beat as well as with a symplectic and antiplectic metachronal wave around the peripheral cells. We present the level set surface for *Gonium* with both a symplectic and antiplectic metachronal wave around the peripheral cells in Figure 4.12.

In Figure 4.13 we show the displacement over one beat for *Gonium*. In Panel (a), we show the z displacement for *Gonium* with a synchronous beat and in Panels (b) and (c), we show the 3D trajectory for *Gonium* with a symplectic and antiplectic metachronal wave respectively. We find that for the synchronous beat shown in Figure 4.13a, the z displacement is qualitatively similar to that of *Tetrabaena*. Numerically, we find that the synchronous beat gives a straight line velocity of $\sim 42\mu m/s$. This matches well with the experimentally observed velocity of $40\mu m/s$ (de Maleprade et al., 2019). In Panels



(a) Synchronous Beat (b) Symplectic Beat (c) Antiplectic Beat

Figure 4.13: Figure showing the displacement of *Gonium* over one beat. Our model for *Gonium* has flagella with a length of $40\mu m$ and a frequency of $10Hz$. Panel (a) shows the z displacement from a synchronous beat. Panels (b) and (c) show the 3D trajectory for *Gonium* with a symplectic and antiplectic metachronal wave respectively where the x component of the trajectory is shown by the colour.

(b) and (c) of the figure, we show the trajectories for *Gonium* with a metachronal wave. Here, we see Gonium swimming with a Helical path. The antiplectic beat is seen to have a higher straight line velocity while the symplectic beat moves with a much wider helical path.

Experimentally, *Gonium* is found to swim with a helical path with a pitch angle of approximately 30 ± 13 (de Maleprade et al., 2019), which would qualitatively match with our calculated trajectory for the metachronal waves. In contrast to this, the synchronous model is unable to produce a helical path. de Maleprade et al. (2019) suggest that the helical path could be due to a slight inbalance of force over the peripheral flagella. This would mean that some flagella would exert more force than others to produce this helical path. Here we find another method that can also produce helical trajectories. We show that they could be produced by utilising out of phase flagella. Both of these methods provide a reasonable solution to how helical trajectories could be formed. However, further work will need to be done to extend our results to quantify the helicity of a trajectory for a general metachronal wave or for any specified phase difference. We could then compare to see if we can produce trajectories with similar helicity to those experimentally observed and exactly what phase shift would be required.

We also test the swimming of *Gonium* with a synchronous beat for differing levels of mucilage between the cells. The z displacement for these swimmers is shown in Figure

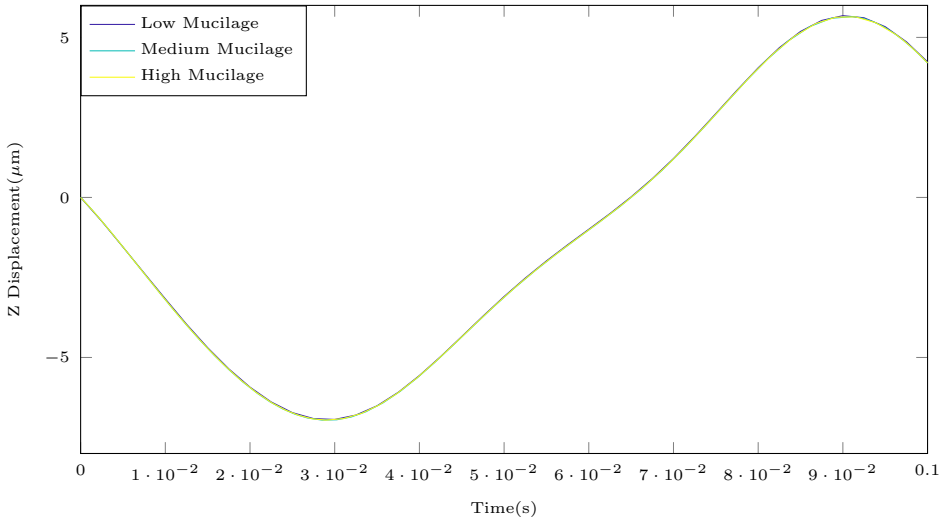


Figure 4.14: Figure showing a comparison of the swimming behaviour for *Gonium* with different levels of mucilage displaying the z displacement for the swimmers. Our model for *Gonium* has flagella with a length of $40\mu m$ and a frequency of $10Hz$. We can see that there is very minimal difference between these results.

4.14. Here we again see that the level of mucilage has very minimal effect on the swimming of *Gonium*. Considering this result and the similar result for *Tetrabaena*, we conclude that the level of mucilage does not appear to have a significant effect on the swimming behaviour for the Volvocine Green Algae.

4.4.4 Pandorina

We next consider the 16 celled *Pandorina*. *Pandorina* is the first and smallest spherical colony that we study. It is found to have an average radius of $\sim 15\mu m$ (Höhn and Hallmann, 2016). However, relatively little work has been done on *Pandorina*, and we are therefore unable to find details of flagellar dimensions, beat frequency or swimming speed. Since it is a spherical Volvocine swimmer, as a base case we model it using the flagella of Volvox. These have length of $20\mu m$ (Pedley et al., 2016) with a frequency of $25Hz$ (Solari et al., 2011). As is seen in *Volvox*, we also introduce a 15 degree tilt in the flagella. This produces a clockwise rotation which occurs in all known species of Volvocine green algae (Goldstein, 2015), apart from some mutants. Also, for the body of this swimmer, as well as the remaining spherical swimmers, we no longer model the individual cells and we use

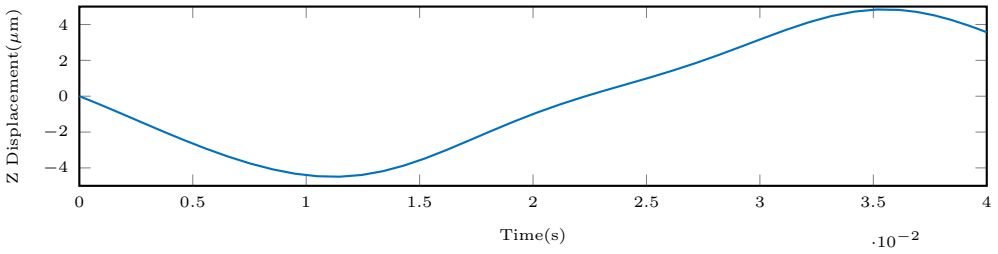


Figure 4.15: Figure showing the displacement of *Pandorina* over one beat. Our model for *Pandorina* is spherical swimmer with radius $\sim 15\mu m$ has flagella with a length of $20\mu m$ and a frequency of $25Hz$. We show the z displacement from a synchronous beat.

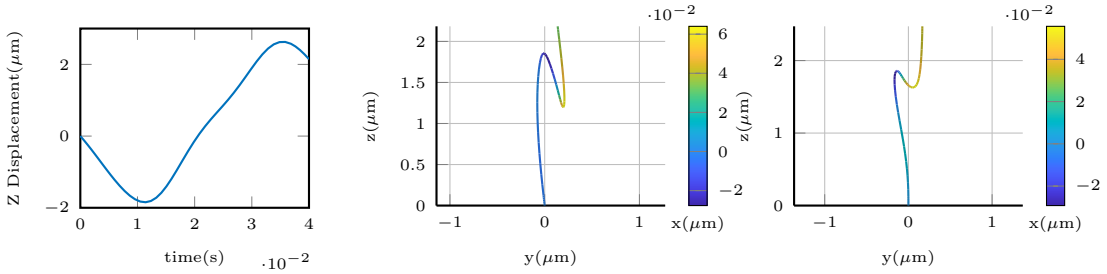
a single sphere to model the body of the entire colony.

The displacement over one beat for *Pandorina* is shown in Figure 4.15. We find that z displacement for a synchronous beat is qualitatively similar to that of *Gonium* and *Tetrabaena*. However, *Pandorina* is calculated to be much faster with a dimensional straight line velocity of $\sim 89.2\mu m/s$. This is expected due to the raft arrangement of *Gonium* and the placement of its flagella. In particular, it can be seen that the flagella of the peripheral cells of *Gonium* are mostly contributing to the rotation of the swimmer rather than the forward movement. For *Pandorina* however, all the flagella are beating in the same direction with their main contribution to forward motion. As well as this, we would also expect the spherical arrangement of cells in *Pandorina* to produce less drag than the raft arrangement of cells present in *Gonium*.

4.4.5 Eudorina

The next swimmer we consider is the 32 celled *Eudorina*. As with *Pandorina* we model the colony using *Volvox* flagella since *Eudorina* is also a spherical colony of the Volvocine green algae. These are $20\mu m$ with a frequency of $25Hz$. As with *Pandorina*, *Eudorina* is also a spherical colony with an average radius of $\sim 50\mu m$ (Höhn and Hallmann, 2016). Therefore, we model it as a sphere with 32 pairs of flagella around it to represent each cell distributed to be evenly spaced around the body. For both *Pandorina* and *Eudorina* the position of the flagella are placed approximately by eye.

We show the displacement for *Eudorina* with different beats in Figure 4.16. In Panel



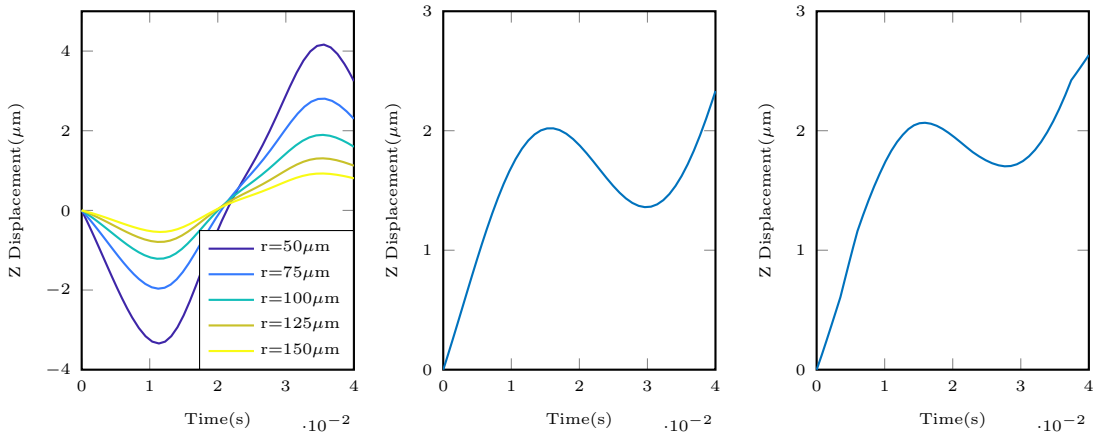
(a) Synchronous Beat (b) Symplectic Beat (c) Antiplectic Beat

Figure 4.16: Figure showing the displacement of *Eudorina* over one beat. Our model for *Eudorina* is spherical swimmer with radius $\sim 50\mu m$ has flagella with a length of $20\mu m$ and a frequency of $25Hz$. Panel (a) shows the z displacement from a synchronous beat. Panels (b) and (c) show the 3D trajectory for *Eudorina* with a symplectic and antiplectic metachronal wave respectively where the x component of the trajectory is shown by the colour.

(a), we show z displacement over one beat for the flagella beating synchronously and in Panels (b) and (c), we plot the 3D trajectory for *Eudorina* with a symplectic and antiplectic metachronal wave respectively. The z displacement for the synchronous beat as shown in Panel (a), is qualitatively similar to the displacement of the synchronous beats of *Tetrabaena*, *Gonium* and *Pandorina*. For the symplectic and antiplectic beats, there is a larger variation in the x and y directions than for the synchronous beat. However, unlike for *Gonium*, the metachronal wave for *Eudorina* does not result in a helical trajectory. This can be seen since the trajectories for *Eudorina* seen in Panels (b) and (c) of Figure 4.16 differ from the helical trajectories shown for *Gonium* in Panels (b) and (c) of Figure 4.13.

4.4.6 Pleodorina

The final algal colony that we model is the 64 celled *Pleodorina*. This will be the largest algal colony that we consider herein, since we do not model *Volvox* that can have thousands of cells. We once again model the flagella as the same as *Volvox* flagella. *Pleodorina* typically consists of 64 or 128 cells and have colony sizes ranging from $100 - 300\mu m$ in diameter with an average radius of $\sim 75\mu m$ (Höhn and Hallmann, 2016). We therefore model this array of sizes in $50\mu m$ intervals.



(a) Synchronous (b) Symplectic, $r = 75\mu m$ (c) Antiplectic, $r = 75\mu m$

Figure 4.17: Figures showing the z displacement for *Pleodorina* over one beat. Panel (a) shows the displacement for a single beat with different colony radii. Panel (b) and (c) show the z displacement for a *Pleodorina* with a colony radius of $75\mu m$, with a Symplectic and antiplectic beat respectively. For all Panels the flagella have length $20\mu m$ and frequency of $25Hz$.

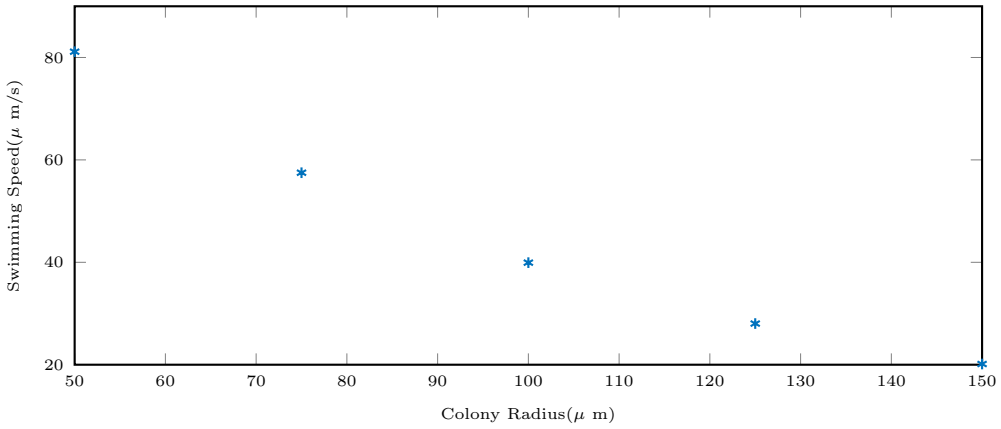


Figure 4.18: Figure Showing the model straight line speed of *Pleodorina* for different colony radii from $50\mu m - 150\mu m$.

In Figure 4.17, we show the z trajectory for *Pleodorina* modelled at different sizes from $r = 50\mu m$ to $r = 150\mu m$ for the synchronous beat in Panel (a) and with a metchronal wave in Panels (b) and (c) that is symplectic and antiplectic respectively.. We see that it is qualitatively similar to that of the previous swimmers from *Tetrabaena* to *Eudorina*. We also see as expected that the trajectory flattens as the radius of the colony increases. For a colony radius of $75\mu m$ we calculate a straight line velocity for the colony of $\sim 57.5\mu m/s$. This matches reasonably well with results from Solari et al. (2006) for *Pleodorina* with a $71\mu m$ radius which gives an upward velocity of $56\mu m/s$. We show the model swimming speed for each radius for synchronous beating in Figure 4.18. The speed is shown to decrease as the radius increases. However, it should be noted that the larger colony sizes of *Pleodorina* would likely be 128 celled colonies and would therefore have a higher velocity than is predicted here.

For Figure 4.18, we consider whether this figure matches with what we would expect. To do this we will analyse the forces for a colony of specific radius. We have

$$F_{\text{sphere}} + F_{\text{cilia}} = 0,$$

where we assume F_{cilia} is constant and we have $F_{\text{sphere}} = 6\pi\mu U r$ from Stokes law where r is the radius of the *Pleodorina* colony. From this we can clearly see that we have

$$U = \frac{-F_{\text{cilia}}}{6\pi\mu r} \implies U \sim \frac{1}{r}.$$

We note that if we take the assumption of $U \to \infty$ as $r \to 0$, then we attempt to fit the function

$$\tilde{U} = \frac{A}{B + \tilde{r}}.$$

However this function does not provide a good fit to the data. This implies that the hydrodynamic interactions between flagella or the interaction between the flagella and the surface of the colony have an effect on the swimming of *Pleodorina* particularly for

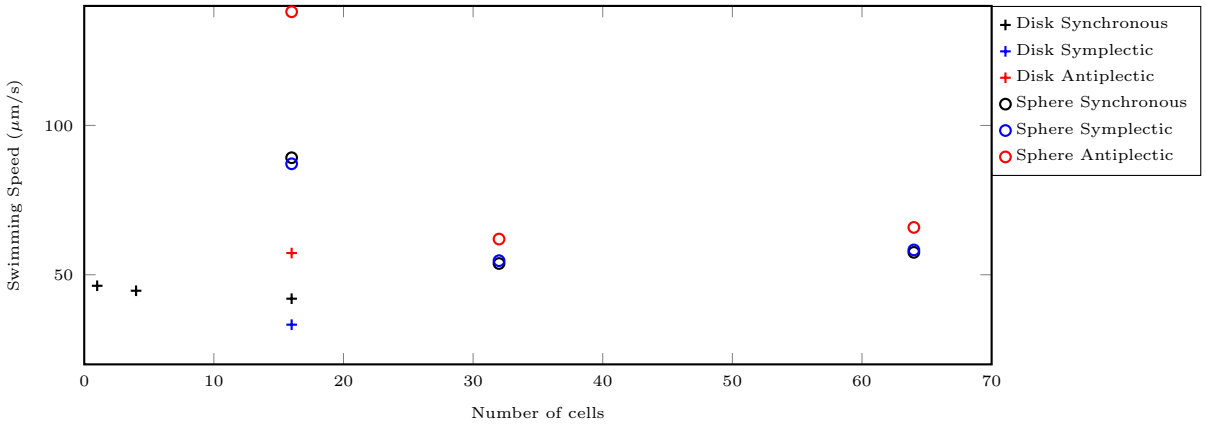


Figure 4.19: Figure showing the model velocities for Volvocine green algae showing the model results for Synchronous beating as well as for a metachronal wave of a nondimensional wave number of 1 and -1 where applicable.

smaller colonies.

4.4.7 Volvocine Discussion

We compare the results of swimming speed for the Volvocine green algae in Figure 4.19 in which we plot the swimming speeds of the different swimmers against each other for synchronous and metachronal beats. We also collate the details of the our models for the Volvocine green algae including experimental swimming speeds where possible in Table 4.1. Here we see a few trends common amongst all the swimmers. One of these is that, where applicable, an antiplectic metachronal wave produces the fastest swimming speed while a symplectic wave produces the slowest swimming speed. We also see a general decrease in swimming speed as the colony size or number of the cells of the swimmer increases. This then jumps up as we move to the smallest spherical swimmer (*Pandorina*), and again decreases as the number of cells or radius of the colony increases.

However, we should also note that our model is unable to deal with collisions between flagella. Therefore, we have to be careful when placing flagella that they will not cross either the body or each other. This is particularly notable in the smaller spherical swimmers such as *Pandorina* as the flagella would be closer together so more likely to intersect. We place the flagella to avoid this, however this could have an impact on their modelled

Swimmer	Colony size (Cells)	Flagella length (μm)	Flagella Frequency (Hz)	Experimental Swim Speed ($\mu m/s$)	Numerical Swim Speed ($\mu m/s$)
Chlamydomonas	1	10-12	60	41	46.3
Tetrabaena	4	40	10	Unknown	44.7
Gonium	16	40	10	40	42.0
Pandorina	16 (spherical)	20	25	Unknown	89.2
Eudorina	32 (spherical)	20	25	Unknown	53.8
Pleodorina	64 (spherical)	20	25	56	57.5

Table 4.1: Table collating the model details for the Volvocine green algae. Where Experimental swim speed is written as unknown, it was unable to be found. For the flagella of the spherical swimmers, we assume their beating to be the same as the beating of *Volvox* flagella. We take their length to be $20\mu m$ (Pedley et al., 2016), and their frequency to be $25Hz$ (Solari et al., 2011)

swimming behaviour.

4.5 Didinium nasutum

The level set method which we use to model the bodies of our swimmers is a very powerful tool. It can be used to model a large variety of complex shaped swimmers. Here, we will further demonstrate this ability by using it to model the swimmer, *Didinium*. This is an unusually shaped swimmer for which little to no mathematical models have been constructed.

Didinium is a single celled swimming protozoan. They are found to have an average length of $127\mu m$ (with a range of $93 - 154\mu m$) with an average maximum radius of $40\mu m$ (with a range of $57 - 95\mu m$) (Pernberg and Machemer, 1995). It has an egg like shape with a long thin nose that is used for feeding called the proboscis protruding out of the front of the swimmer as shown in Figure 4.20a taken from Antipa (1968). This proboscis is typically used for attaching on to its prey, *Paramecium*, to consume it. The interaction between *Didinium* and *Paramecium* is largely studied through predator-prey

models (Luckinbill, 1973; Harrison, 1995).

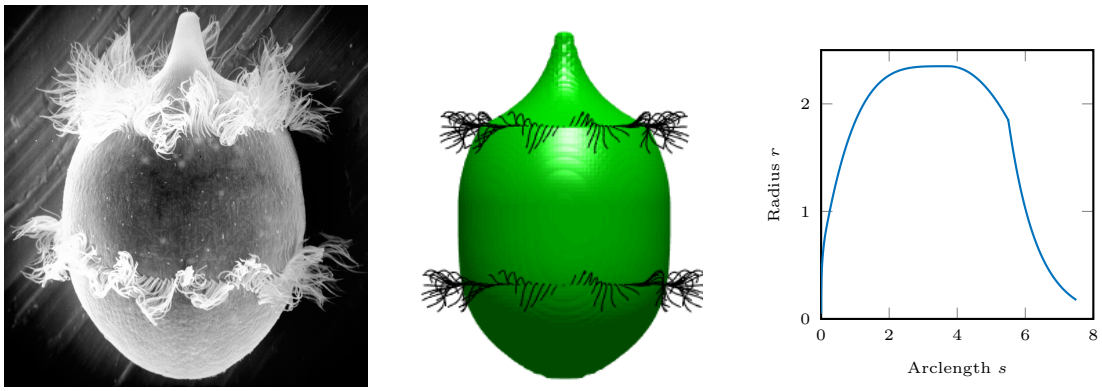
To swim, it uses approximately 3000 beating flagella to move forwards and backwards along right handed helical paths (Pernberg and Machemer, 1995). These flagella are contained in two bands of cilia called cilliary girdles and have length $17\mu m$. These are located at the top of the swimmer just before the proboscis and around two thirds of the way down the swimmer. When moving forwards the flagella are oriented with a 18 degree tilt and a frequency of approximately $15Hz$, and they reorient themselves when swimming backwards with a 24 degree tilt and a frequency of $26Hz$ (Pernberg and Machemer, 1995). We model the flagella using the fitted waveform modelled from a *Volvox* flagellum given in equation (2.36). However, to model the body we need to extend our level set approach.

We use a similar method of level sets as with the Volvocine Green Algae to discretise the body of *Didinium*. To model this swimmer we wish to build a surface that is extruded out from a given centre line with a desired radius. For this, we will again make use of the Gaussian function. However, instead of summing the Gaussian functions with each Gaussian representing a single cell, we take the integral of the Gaussian along the centre line. This is then given by

$$f_{CL} = \int_0^L \exp\left(\frac{-r(s)^2}{B_1}\right) ds, \tag{4.1}$$

where $r(s)$ is the radius at the point on the centre line given by arc length s and L is the size of the centre line. The radius used is shown in Panel (c) of Figure 4.20. Here we also show the swimmer discretisation produced by the level set method in Panel (b) and can compare to the experimental image of *Didinium* in Panel (a).

We then model the swimming of *Didinium* using the Nearest Neighbour Regularised Stokelet method with both a synchronous beat and a metachronal wave for both a dexioplectic and laeoplectic wave. These are metachronal waves in which the direction of the metachronal wave is perpendicular to the direction of the flagella beat. If the effective stroke of the flagella to the right of the metchronal wave direction then it is dexioplectic



(a) Experimental (b) Level Set Model (c) Radius

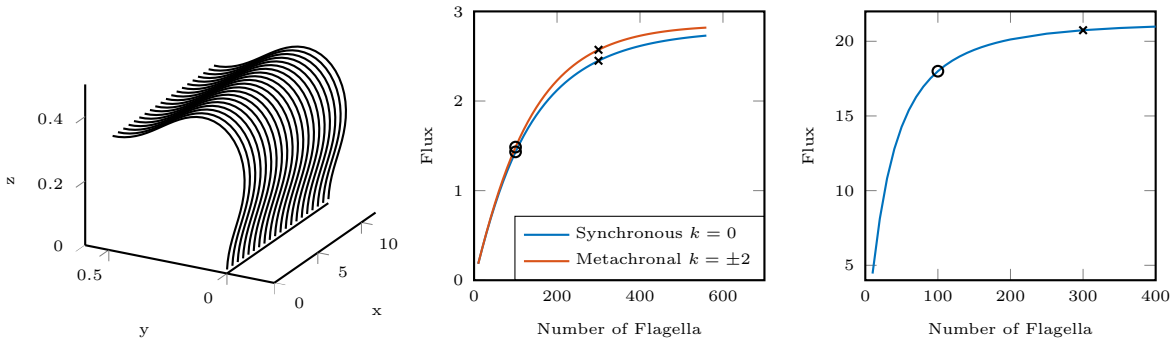
Figure 4.20: Figure showing the Discretisation of *Didinium*. Panel (a) shows an experimental image of *Didinium* (Antipa, 1968), Panel (b) shows our model for the discretisation of *Didinium* using level sets and Panel (c) shows the radius r, of the swimmer at the point on the centre line given by arclength s. The values for the arclength and radius are nondimensional with respect to the flagella length.

and it is laeoplectic if the effective stroke is to the left of the metachronal wave direction. For the waveform, we use the *Volvox* waveform as given in equation (2.36).

4.5.1 Convergence

Didinium has a total of approximately 3000 flagella. However, computational limits would make modelling a *Didinium* with 3000 flagella unfeasable. We therefore performed a convergence study, investigating how the flux increases with the number of flagella. We perform this convergence study for flagella placed on a line to reduce the computational complexity that would occur for considering flagella on the body of *Didinium* allowing us to consider a larger number of flagella in our convergence study

We show an analogue to this convergence in Figure 4.21. In this figure we consider a line of flagella beating synchronously perpendicular to the line. This line has the length of the circumference of *Didinium* at the location of the top ciliary girdle as shown in Panel (a) of the figure. To find the convergence we calculate the $y-$component of the flux



(a) Flagella (b) Single Point Covergence (c) Full Flagella Covergence

Figure 4.21: Figure showing the flux produced by flagella over a line in x direction of the length of the circumference of *Didinium* at the ciliary girdle location. We show the convergence of the y component of the flux for increasing number of flagella beating in the y direction. Panel (a) displays how the flagella are arranged and Panels (b) and (c) shows the convergence results. Panel (b) gives the results for flagella represented as a single point for both synchronous($k = 0$) and metachronal($k = \pm 2$) beating and Panel (c) shows the convergence using full discretised flagella. On Panels (b) and (c) we show the number of flagella for which most of our results are taken with an o symbol. We also show the number of flagella used for our results with a higher number of flagella.

produced by the flagella given by

$$Q = \sum_{1}^{N} \int_{0}^{2\pi} \int_{0}^{1} F_y(s,t) z(s) ds dt, \tag{4.2}$$

where $z(s,t)$ is the height of the flagella above the boundary at arclength s and time t and $F_y(s,t)$ is the y component of the force at that point. We show the calculated value of this flux in Panels (b) and (c) with Panel (b) showing the results from modelling the flagella as a single point and Panel (c) showing the convergence results for full flagella.

We also run the single point flagella analysis for a metachronal wave number of 2 and -2. Modelling the flagella as a single point allows us to run convergence results faster allowing us to obtain convergence data for additional cases (such as for metachronal waves) more easily. We can then use the full flagella convergence for the synchronous case to consider how much faster full flagella converge compared to single points.

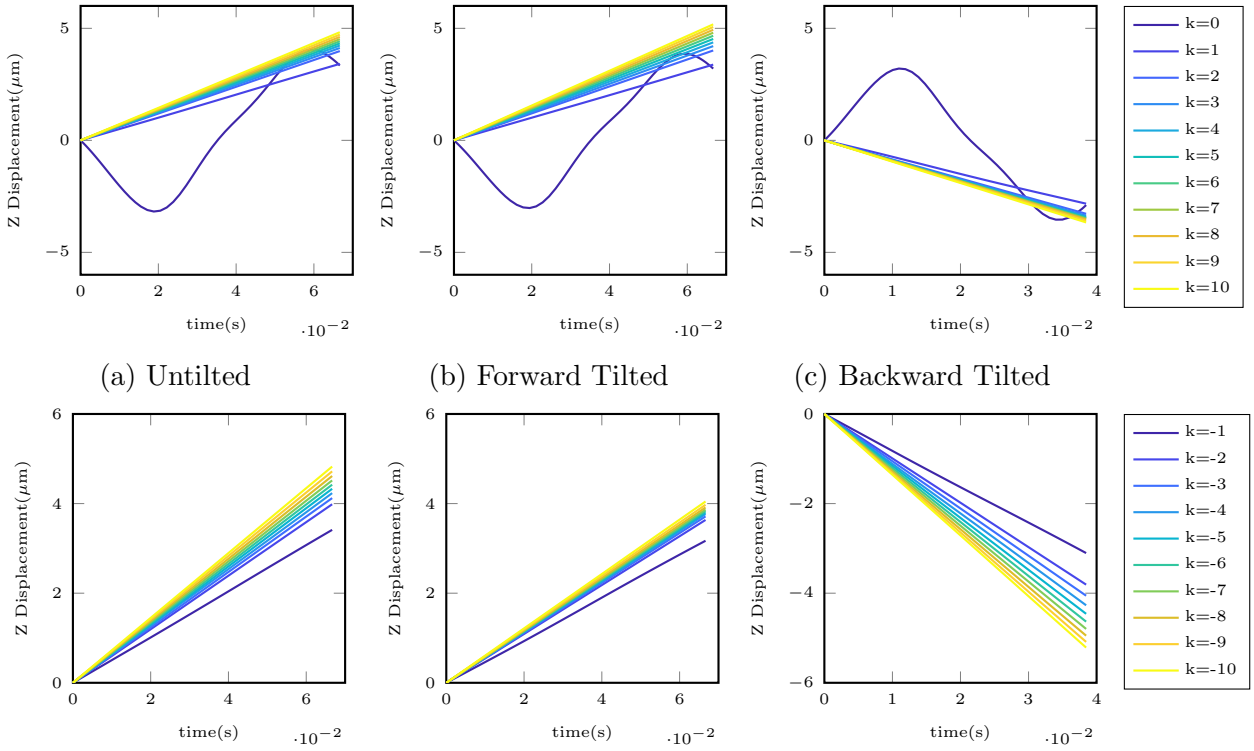
As expected, we find that as we increase the number of flagella the calculated flux begins to converge in each of the cases. We see that for the metachronal wave, its direction

to the left or right does not change the value of the flux in the y-direction. This would be expected since the direction of the metchronal wave is perpendicular to the beating of the flagella. For tilted flagella, we would expect to see a difference between the two directions of metachronal wave. The metchronal wave can also be seen to converge at a very similar rate to the synchronous flagella. We also find that the calculation with full flagella starts to converge must faster than with single points. This is to be expected since the convergence would be caused through hydrodynamic interactions between the flagella. These are clearly stronger between full flagella than between single points. In Panel (c), we find that our value of 100 flagella per ciliary girdle is at a point that is starting to converge making it a reasonable point to take our results from. However, our value of 100 flagella per band is still at a point on the convergence graph in Panel (b) (for single points representing flagella) with a sharp incline. Therefore, we will also consider some of our results for 300 flagella per ciliary girdle or a total of 600 flagella. We do this for the two of our cases that are most similar to a real *Didinium*. That is for metachronal wave with wave number $k = 10$ moving both forwards with tilted flagella and backwards with tilted flagella.

We keep the main bulk of our results with a total of 200 flagella since this is sufficient to obtain reliable qualitative results and trends of the swimming behaviour.

4.5.2 Swimming Behaviour

We now investigate the model swimming behaviour of *Didinium* using the Nearest Neighbour method. We first consider the z-trajectory of swimming *Didinium* for various metachronal waves, with wave numbers given by integers from $\pm 1 - 10$. The metachronal waves that we test will go in both directions and we will also model the case of synchronous beating. We denote dexioplectic metachronal waves moving to the right with positive wave numbers and laeoplectic metachronal waves moving to the left with negative wave numbers. We do this for flagella pointing straight down with no tilt as well as the flagella tilted by 18 degrees to the left of straight down for forward swimming. We



(a) Untilted (b) Forward Tilted (c) Backward Tilted

(d) Untilted (e) Forward Tilted (f) Backward Tilted

Figure 4.22: Figure showing the z displacement of our model *Didinium* for different flagella orientations and Metachronal waves over one beat. In all cases the flagella have length of $17\mu m$. The top row displays results for both a synchronous beat shown by $k = 0$ and a metachronal wave moving to the right (dexioplectic) shown for positive k and the bottom row shows results for a metachronal wave moving to the left (laeoplectic) shown for negative k. Panels (a) and (d) show the results for a forward swimming *Didinium* with flagella pointing straight down with a frequency of $15Hz$. Panels (b) and (e) show the results for a forwards swimming *Didinium* with flagella pointed down and tilted 18 degrees to the left with a frequency of $15Hz$. Panels (c) and (e) present the displacement for a backwards swimming *Didinium* with flagella pointed up and tilted 24 degrees to the right with a frequency of $26Hz$.

also model the swimming with the flagella pointed up tilted 24 degrees (Pernberg and Machemer, 1995). For the forward swimming we use a frequency of $15Hz$ and we use a frequency of $26Hz$ for the backwards swimming (Pernberg and Machemer, 1995). For the flagella beat, we use the *Volvox* beat as used for the Volvocine Green algae.

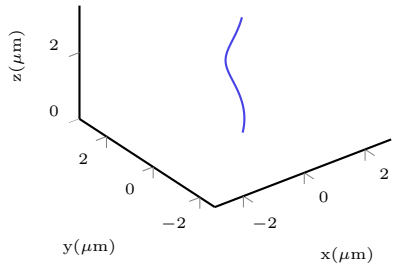
We present the results for z displacement of *Didinium* in Figure 4.22. The top row displays the results for a metachronal wave moving to the right (dexioplectic) as well as the synchronous beat, and the bottom row shows the trajectory for a metachronal wave moving to the left (laeoplectic). Qualitatively, the synchronous beating is similar

to that of the Volvocine green algae with the swimmer moving forward (or backwards for the backwards swimming case) during the effective stroke and in the other direction during the recovery stroke as would be expected. The metachronal beat for all wave numbers and flagella orientations removes the reverse swimming from the recovery stroke and the swimmer moves constantly forwards (or constantly backwards for the backwards swimming *Didinium*) in the z direction.

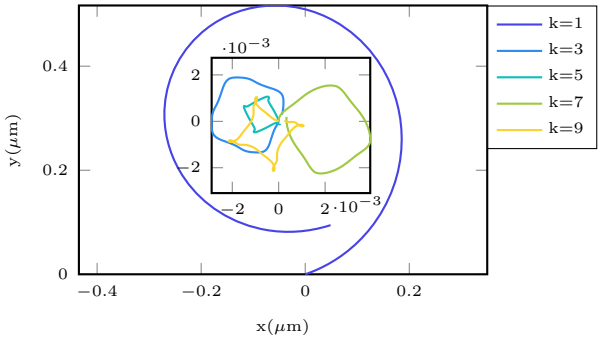
Comparing the two forward swimming cases, we see that for synchronous beating, the swimming *Didinium* with flagella tilted slightly down moves slightly faster than the swimming *Didinium* with tilted flagella. This is to be expected as a part of the force produced by the tilted flagella will go into rotating the swimmer. However, this is not found to be the case for all of the metachronal waves. For the dexioplectic metachronal wave with the highest wave number that we consider of 10, The forward swimming of the *Didinium* with the tilted flagella is found to be faster than the swimming of the *Didinium* with untilted flagella. This is also the direction of Metachronal wave that *Didinium* was found to have when swimming forwards. When looking at the metachronal wave in the other direction however, we see that the swimmer with tilted flagella remains slower than the untilted flagella for all wavenumbers.

We then look at the lateral movement of forward swimming *Didinium* with flagella pointing straight down. We show the $x-y$ trajectories for odd wavenumbers in Figure 4.23. The *Didinium* with metachronal waves of an even wavenumber have negligible movement in the $x-y$ direction most likely due to numerical error. Therefore, they are not included in Figure 4.23. For the odd wave numbers, we again see mostly movement in the z direction, however while the $x-y$ movement is small, it is not negligible. For all the odd wavenumbers, we see a slight helical trajectory. Swapping the direction of the metachronal wave is shown to cause the $x-y$ trajectory to be reflected in the $x-$axis.

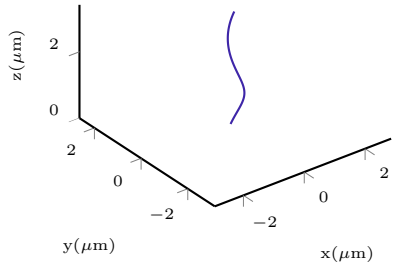
The results that we have discussed are for 200 flagella. We wish to test these results for a total of 600 flagella with 300 flagella per ciliary girdle. This will allow us to show how the swimming behaviour is affected by increasing the number of flagella. We will



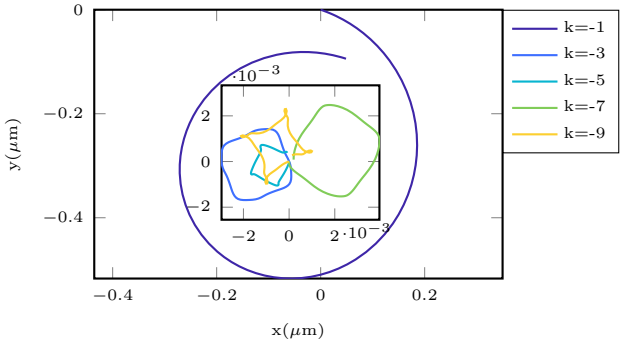
(a) Wave Number=1 3D Trajectory



(b) Odd Wave Number x-y trajectories

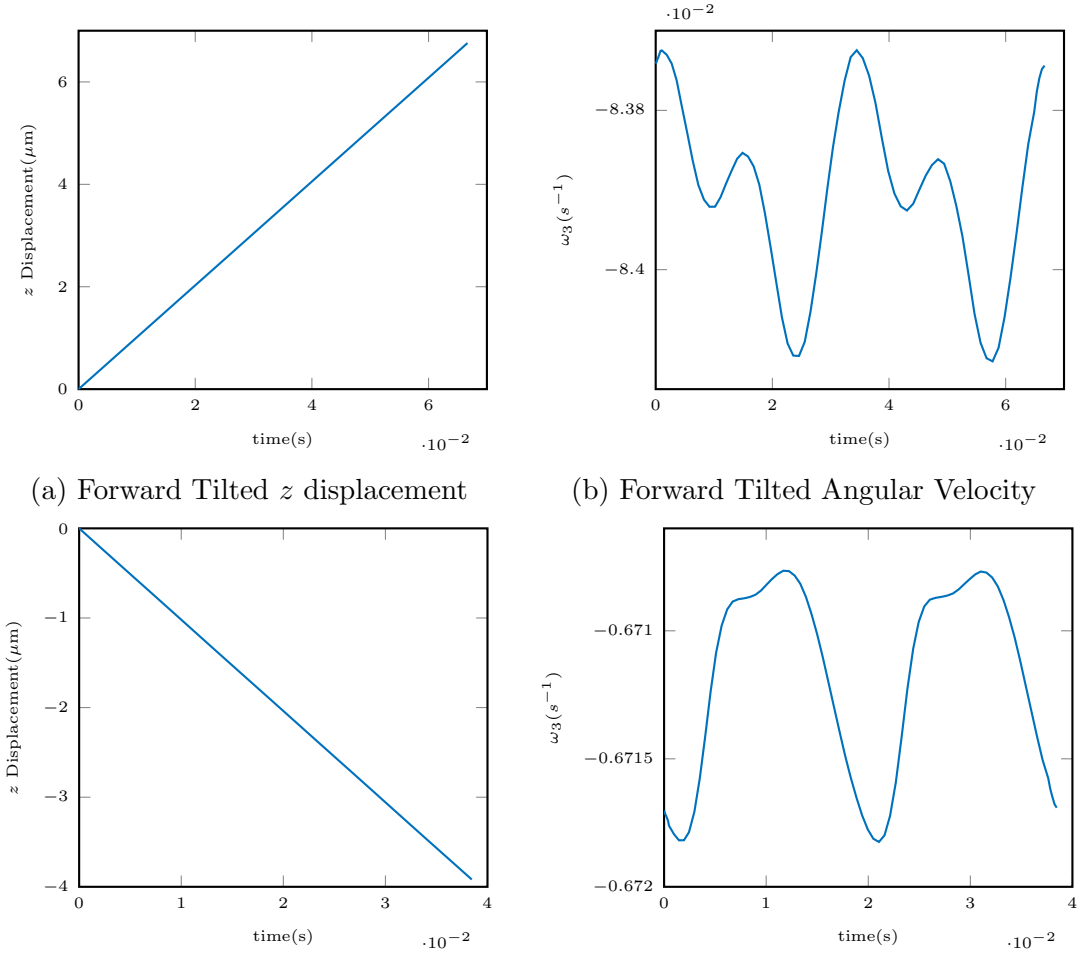


(c) Wave Number=-1 3D Trajectory



(d) Odd Wave Number x-y trajectories

Figure 4.23: Figure showing the 3D (left) and $x-y$ (right) trajectories for forward swimming *Didinium* with no tilt. Panels (a) and (c) show the 3D trajectory for a metachronal wave number of ± 1 for a metachronal wave to the right (a) and left (c). Panels (b) and (d) show the $x-y$ trajectories for the odd wave number metachronal waves. $k = \pm 3, \pm 5, \pm 7, \pm 9$ are shown in the axes in the centre of the panel since they are much smaller than the $k = \pm 1$ case and would not show up otherwise.



(a) Forward Tilted z displacement

(b) Forward Tilted Angular Velocity

(c) Backward Tilted z displacement

(d) Backward Tilted Angular Velocity

Figure 4.24: Figure showing the swimming behaviour of Didinium swimming forwards (top) and backwards (bottom) with tilted flagella. Results are calculated for a Didinium with a total of 600 flagella or 300 flagella per ciliary girdle beating with a Metachronal wave of wavenumber $k = 10$. Panels (a) and (c) show the z displacement and Panels (b) and (d) show the ω_3 component of the angular velocity.

show that the qualitative behaviour is not affected by increasing the number of flagella and it is only affected quantitatively.

In Figure 4.24, we show the swimming behaviour for *Didinium* with a total of 600 flagella and a wavelength of $k = 10$ for forwards and backwards swimming case, both with tilted flagella, plotting results for the z displacement and angular velocity. As in the case with 200 flagella, the main motion is in the z-direction moving forwards or backwards at a constant speed. In Panels (b) and (d) of Figure 4.24, we show the angular velocity. Here we see an almost constant angular velocity with very slight variations.

4.6 Summary

In this chapter we have introduced the Algal Colony Suite. This is an easy to use app that makes use of our level set method to produce models of multicellular swimmers. We then presented how this can be used by producing models and studying the the swimming behaviours for multiple different swimmers of the Volvocine green algae. We also presented how our level set method can be used to study other swimmers with complex shapes with *Didinium*. In the next chapter, we will look at bringing the previous chapter and this one together. We will look to extend our bead and spring model from Chapter 3 to model a full swimmer.

CHAPTER 5

BEAD AND SPRING MODELS OF MICROSWIMMERS

5.1 Model Overview

In the previous chapters we have studied how large groups of cilia synchronise with each other to form metachronal waves and other beating patterns as well as studying the swimming behaviour for many different swimmers such as the Volvocine green algae. We now wish to combine these two studies by modelling how multiple cilia synchronise while over the body of a swimmer. We do this by considering bead spring networks to model full swimmers.

For our swimmer we model the flagella in a similar way as in Chapter 3 in which we have a single bead attached to a spring driven by a driving force to give the beat of our flagella. We then attach a bead to the other end of this spring so that we can connect the flagella to the body using more springs. This allows for a simple way of ensuring that the flagella remain close to the body of bead and spring swimmer and that the flagella move along with the body. To build the body of the swimmer, we use our Level set method to find points in which to place beads over the surface of the body and then fully connect all of these beads using springs. Modelling the body using bead and springs may also allow for future work that builds on this model for studying swimmers with some elasticity regarding its body shape, though this is not studied in this thesis. Modelling the entire

swimmer using bead and springs also helps to more intuitively understand how to extend the force balance for the model used in Section 3.2. A simple example of how this will work is shown in our *Chlamydomonas* model as shown in Figure 5.1.

We now consider the force balance on each of the beads. For a bead i, the force balance is given by

$$\sum_{j=1}^{N_{Spr}^{i}} \boldsymbol{F}_{\boldsymbol{Spr}}^{\boldsymbol{i,j}} + \boldsymbol{F}_{\boldsymbol{Dri}}^{\boldsymbol{i}} + \boldsymbol{F}_{\boldsymbol{Drag}}^{\boldsymbol{i}} = \boldsymbol{0}. \tag{5.1}$$

Here $\boldsymbol{F}_{\boldsymbol{Spr}}^{\boldsymbol{i,j}}$ represents the spring force for spring j acting on bead i. The spring force is given using Hooke's law as presented in Chapter 3 and summed over the springs attached to bead i where N_{Spr}^{i} is the number of springs attached to bead i. We also note that the driving force, $\boldsymbol{F}_{\boldsymbol{Dri}}^{\boldsymbol{i}}$ is 0 if bead i is not a flagella bead. We also note that the drag force $\boldsymbol{F}_{\boldsymbol{Drag}}^{\boldsymbol{i}}$ has both local and non-local components for the force from itself as well as all the other beads. Using Regularised Stokeslets to represent the beads, the velocity of bead i is then given by

$$\boldsymbol{u}(\boldsymbol{x_i}) = \dot{\boldsymbol{x}}_{\boldsymbol{i}} = -\sum_{k=1}^{N_{Bead}} S^{\epsilon}(\boldsymbol{x_i}, \boldsymbol{x_k}) \boldsymbol{F}_{\boldsymbol{Drag}}^{\boldsymbol{i}}, \tag{5.2}$$

where we sum over k from 1 to the number of beads.

5.2 Bead and Spring Model of Chlamydomonas

We start by considering the simplest swimmer that we modelled in the previous chapter, *Chlamydomonas*. To model the swimmer, we wish to create a bead and spring network for the full body of *Chlamydomonas* with all the beads on the body connected. After placing the beads for the cilia in the desired location, we connect it to the body by connecting the stationary cilia bead to the closest beads on the body via springs. The bead and spring structure for this model is shown in Figure 5.1.

We now study how the phase difference between the flagella of *Chlamydomonas* varies over time. *Chlamydomonas* is typically found to swim with with their flagella beating

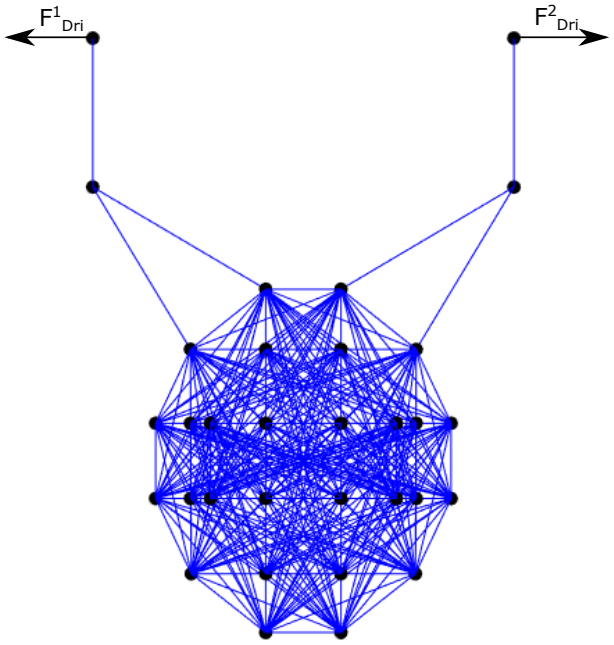
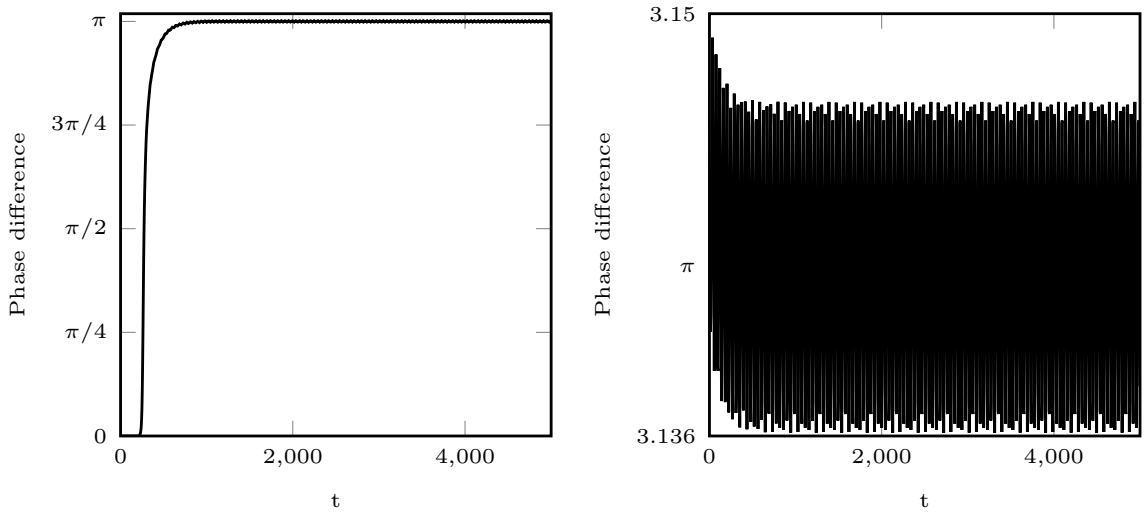
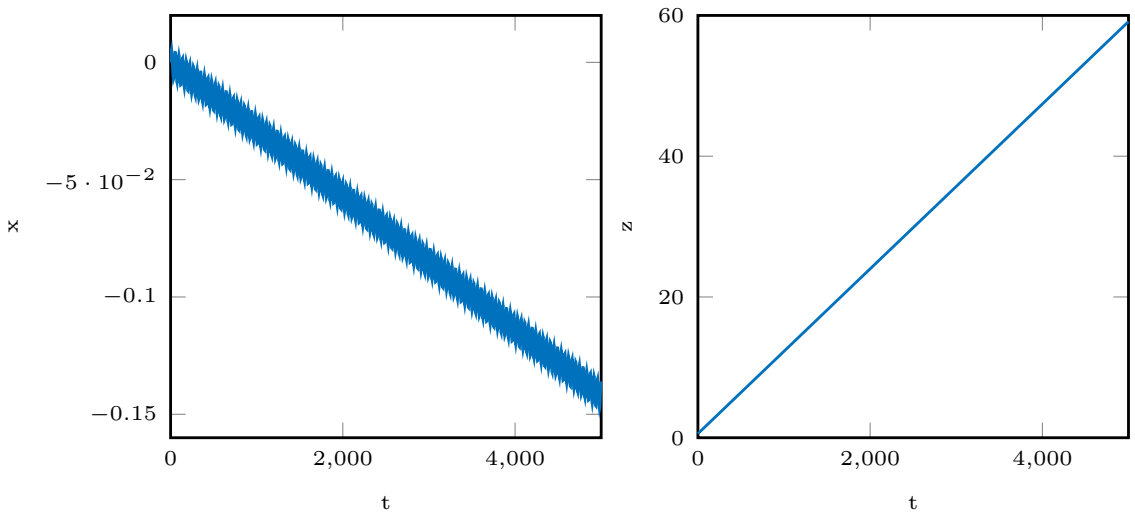


Figure 5.1: We show our Bead and Spring model for *Chlamydomonas*. We find the positions of the beads on the body using the Level set method with each bead in the body connected to all other beads on the body using springs.



(a) Initial Phase = 0 (b) Initial Phase = $\pm\pi$

Figure 5.2: Phase difference over time between the flagella beads of our *Chlamydomonas* bead and spring model with multiple beads to represent the full body. We show results for an initial phase difference of 0 and $\pm\pi$ using Stokeslets.



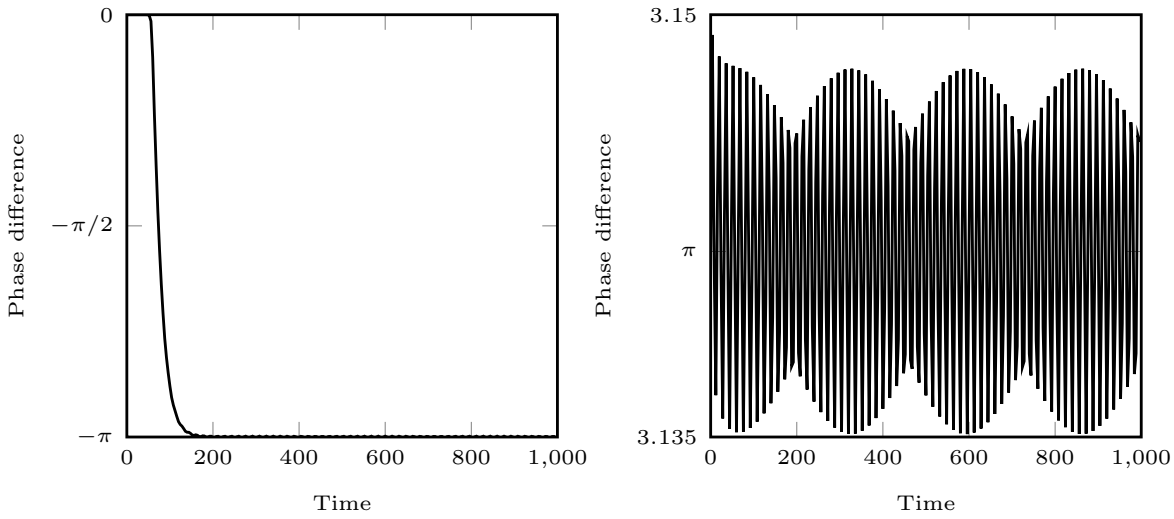
(a) x Displacement (b) z Displacement

Figure 5.3: Figure showing the displacement of our bead and spring model for *Chlamydomonas* with an initial phase difference of π. Panel (a) shows the x displacement and Panel (b) shows the z displacement

either synchronous with each other, giving a phase difference of 0 between the flagella, or asynchronous, giving a phase difference of $\pm\pi$ between the two flagella. Therefore we study *Chlamydomonas* with an initial phase difference of both 0 and $\pm\pi$ as in our previous studies of *Chlamydomonas* in Chapter 4.

How phase difference varies over time for our model is shown in Figure 5.2 for Stokeslets for an initial phase difference of both 0 and $\pm\pi$. Studying an initial phase difference of π, we find that the phase difference of the system stays at π oscillating around this point. This shows that asynchronous beating is a stable fixed point. For an initial phase difference of 0, we find that it stays at its initial phase difference for a short time. However, after a short time staying at 0 it quickly moves to a different stable fixed point of π, again giving the asynchronous case as a stable fixed point. The asynchronous case is occasionally seen in swimming *Chlamydomonas* in nature though is usually used as part of steering.

We show the x and z displacement over time for our bead and spring model of *Chlamydomonas* with an initial phase difference of π in Figure 5.3. Here we see that with the asynchronous beat the swimmer moves forward at a constant rate. This differs from the



(a) Initial Phase = 0 (b) Initial Phase = $\pm\pi$

Figure 5.4: Phase difference over time between 2 beads over a boundary beating in opposite directions like *Chlamydomonas* flagella. The spring centres of the beads are placed a distance $d = 1.3$ apart.

synchronous beat studied in Chapter 4 which moves back and forth due to its effective recovery stroke. Studying Panel (a) of Figure 5.3, we see that the swimmer rocks back and forth while drifting to one side.

For the full bead and spring model of *Chlamydomonas*, we found one fixed point of asynchronous beating. We would initially expect that for two flagella beating in this way, we would have two fixed points of fully synchronous or fully asynchronous. We therefore test two flagella beating away from each other above a boundary using a bead and spring model with no body as in Chapter 3 to see if this can recover the synchronous beating as a stable fixed point.

We show results of the phase difference over time for two beads above a boundary beating in opposite directions to simulate the beating of *Chlamydomonas* in Figure 5.4. We again test for an initial phase difference of 0 and π. We again see that the synchronous case is not a stable fixed point for this system. As with the full body bead and spring model, we find one fixed point around π. This is equivalent to our results for the case with the full body. One small difference that we see, is that the system stays at a synchronous

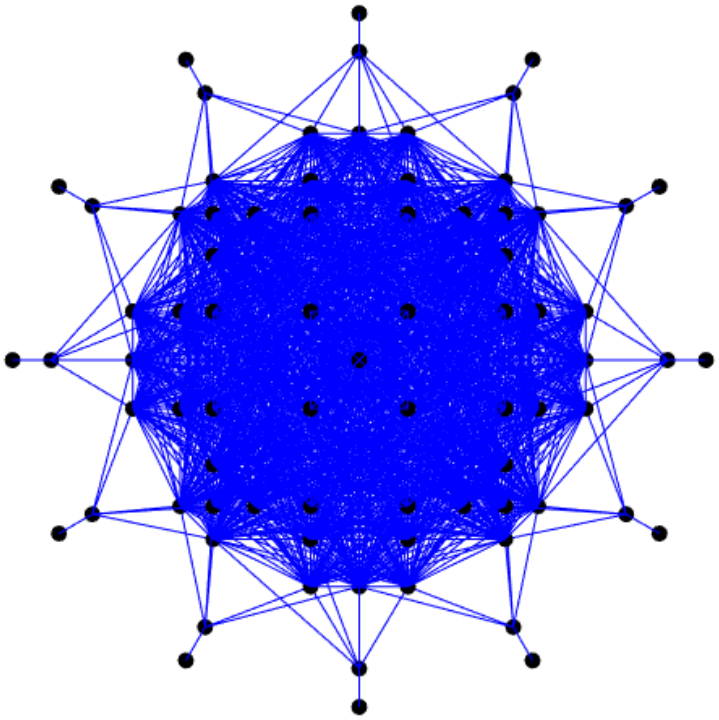


Figure 5.5: We show our Bead and Spring model for our multiciliate swimmer with 12 flagella. We find the positions of the beads on the body using the Level set method with each bead in the body connected to all others beads on the body using springs.

beat for a shorter time when the body is not present. For the synchronous case to be stable, we may need a more detailed model. This model would have more detailed flagella with more than one bead so that drag anisotropy can be considered. Without this drag anisotropy, the force moving the swimmer backwards during the recovery stroke will be very similar to the amount of force produced to move the swimmer forward during the effective stroke. With little differentiation between these two phases of the stroke, the swimmer will struggle to move. Therefore it is likely that we need this for a synchronous beat to be a stable steady state.

5.3 Bead and Spring Model For a Multiciliate Swimmer

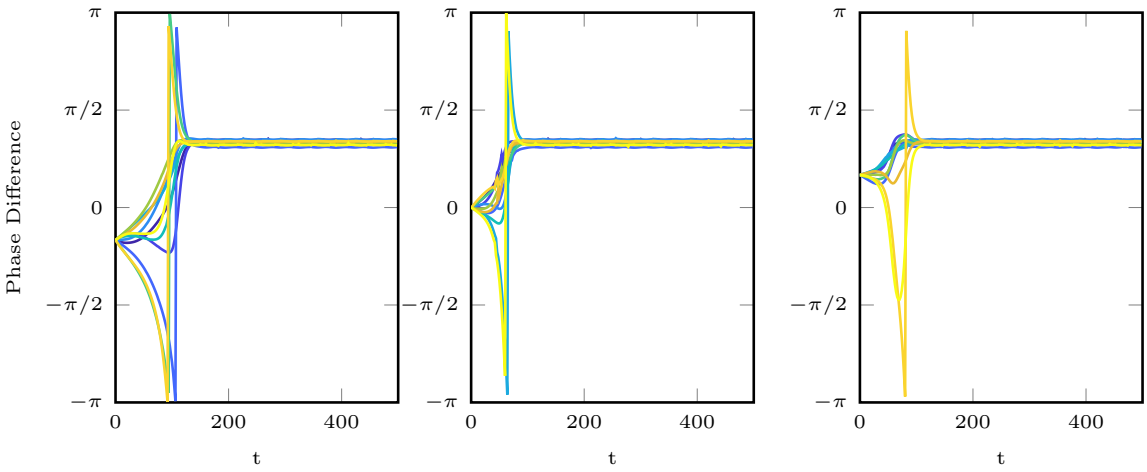
We next wish to use our bead and spring model to study the interaction and synchronisation of flagella for more multiciliate swimmers. This will allow us to see if we can find metachronal waves or other coordinated beat patterns emerging around these multicellular swimmers. Here we will consider a simple multiciliate swimmer consisting of a spherical body with twelve flagella placed around the middle of the swimmer as shown from above in Figure 5.5. This model presents a 3-D version of our study on the Bead and spring model for flagella around a circle in Section 3.2.4.

This model also gives us a simple model in which the synchronisation of the flagella could be seen to be somewhat analogous to the flagella on the peripheral cells of *Gonium*. Since we are considering this swimmer as analogous to the peripheral cells of *Gonium* we point the flagella with a 15 degree tilt down from the $x - y$ plane as is found on the biological swimmer. We can then see how these results compare with our earlier studies on *Gonium*

Due to the similarities between this model and our model of flagella around a circle using the bead and spring method we expect there to be similar results. That is, we expect there to potentially be stable fixed points for integer metachronal wave numbers. Therefore, we will model the phase difference between the flagella for an initial phase difference of 0 giving a synchronous beat, as well as an initial phase difference of $\pm 2\pi/12$ giving a metachronal wave with a metachronal wave number of ± 1.

We show results for the change in phase difference over time between neighbouring flagella beads of spherical multiciliate bead and spring model in Figure 5.6. These results are given for three initial phase differences. That is, a synchronous initial beat with a phase difference of 0 and two metachronal beats, both symplectic and antiplectic with wave numbers of ± 1.

For each of the starting phase differences we see very similar results. An interesting thing to notice, is that unlike in the Stokeslets case for bead and spring flagella around



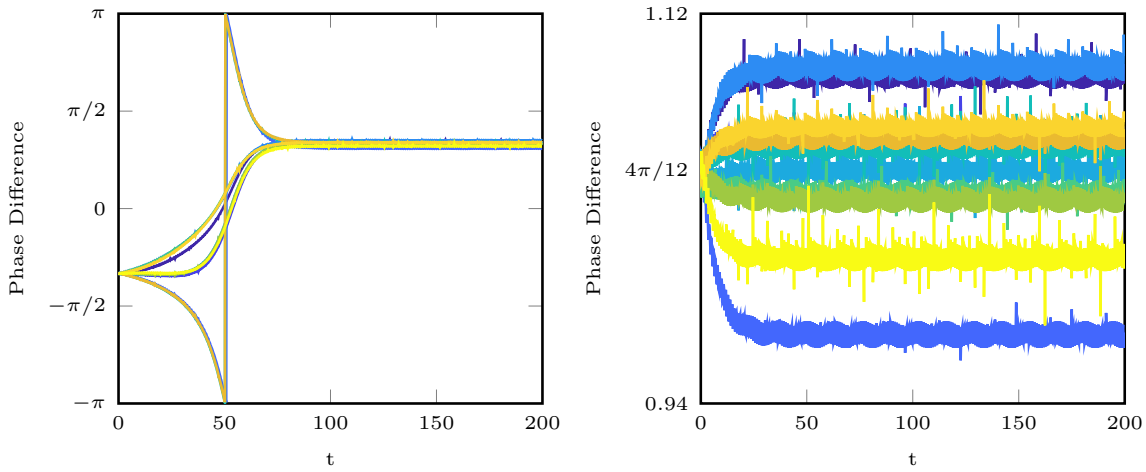
(a) Phase $= -2\pi/12$ (b) Phase $= 0$ (c) Phase $= 2\pi/12$

Figure 5.6: Phase difference over time between the neighbouring flagella beads of our Spherical multiciliate bead and spring model with 12 flagella and multiple beads to represent the full body. We show results for an initial phase difference of 0 and $\pm 2\pi/12$ using Stokeslets.

a circle, as studied in Chapter 3, we find the wave numbers of ± 1 are not stable steady states. We also find no metastability of the synchronous case which was found for some of the cases around a circle. In each case the system synchronises towards the same steady state. That is, neighbouring flagella with a phase difference around $4\pi/12$. This gives something very close to a symplectic metachronal wave with a wave number of 2.

When studying the steady state, we note that it is not an exact metachronal wave. While very close together and centred on a phase difference of $4\pi/12$, the phase differences between the flagella are not all the same. This could be due to noise in the system. It could also be due to the interaction of the flagella combined with the rotation of the body. These combined could make the exact metachronal wave difficult to achieve while the system attempts to get close to it.

We now consider our multiciliate spherical swimmer starting with a metachronal wave with a larger integer wave number as well as negative integer wave numbers to see if we can find an antiplectic steady state. This will allow us to test if we can find other steady states as well as look closer at the steady state that is already found that is close to a



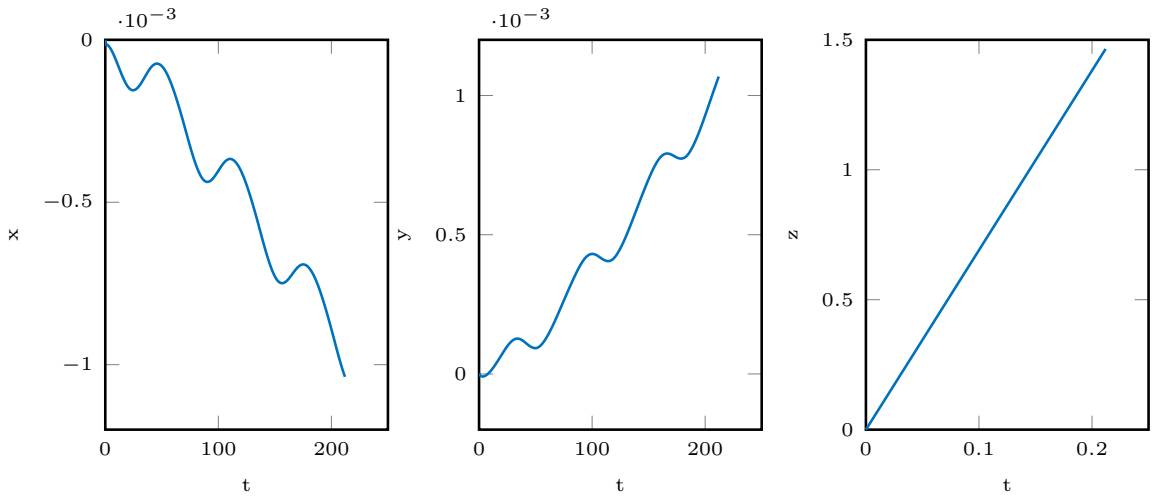
(a) Phase $= -4\pi/12$ (b) Phase $= 4\pi/12$

Figure 5.7: Phase difference over time between the neighbouring flagella beads of our spherical multiciliate bead and spring model with 12 flagella and multiple beads to represent the full body. We show results for an initial phase difference of $\pm 4\pi/12$ using Stokeslets.

metachronal wave with wave number 2.

We show the change in phase difference over time for initial phase differences of $\pm 4\pi/12$ in Figure 5.7. Here we find the same stable steady state as found previously being close to a metachronal wave with wave number 2. We also tested this for a starting metachronal waves with greater wave numbers of ± 3 and ± 4. Here, we again found the same stable steady state so these results are not shown. Therefore, we suggest that our stable steady state may be the only stable steady state of the system and we are unable to find an antiplectic metachronal wave or something that is close to it as a stable steady state.

In Figure 5.8, we plot the displacement of our spherical multiciliate swimmer for an initial phase difference of $4\pi/12$. Here we see that it steadily moves forward in the z direction as we would expect, although quite slowly since it does not have central flagella to drive the forward movement like in *Gonium*. We see that the x and y displacements are very similar with one being close to a reflection of the other. This produces a slightly diagonal trajectory with some occasional tilting back and forth of the body likely caused by its rotation.



(a) x Displacement (b) y Displacement (c) z Displacement

Figure 5.8: Figure showing the displacement of our bead and spring model for our spherical multiciliate swimmer with an initial phase difference of $4\pi/12$. Panel (a) shows the x displacement and Panel (b) shows the y displacement and Panel (c) shows the z displacement.

Studying Panel (b) of Figure 5.7 for an initial phase difference of $4\pi/12$, we can look at our steady state value more closely. Here we see that the phase differences between the neighbouring flagella remain very close to each other but spread around the phase difference of $4\pi/12$. When comparing to our results for *Gonium* in Chapter 4, this would be unexpected as the greatest swimming speed was found for an antiplectic wave. However, *Gonium* is more often found with a symplectic metachronal wave which these results could help us to understand.

Our study of the metachronal wave in *Gonium* in Chapter 4 also only goes to a metachronal wave of ± 1, so maybe larger wave numbers are required to improve the swimming speed such as is found here. We also note that there are many differences between this model and *Gonium* that could have a large effect on the synchronisation and interaction of flagella. Our model has a largely different shape to *Gonium* and we also halve the number of flagella around the sides. We also note the lack of the central flagella that could also have some effect on how the peripheral flagella synchronise.

When comparing this result to our models of interacting flagella around a circle in

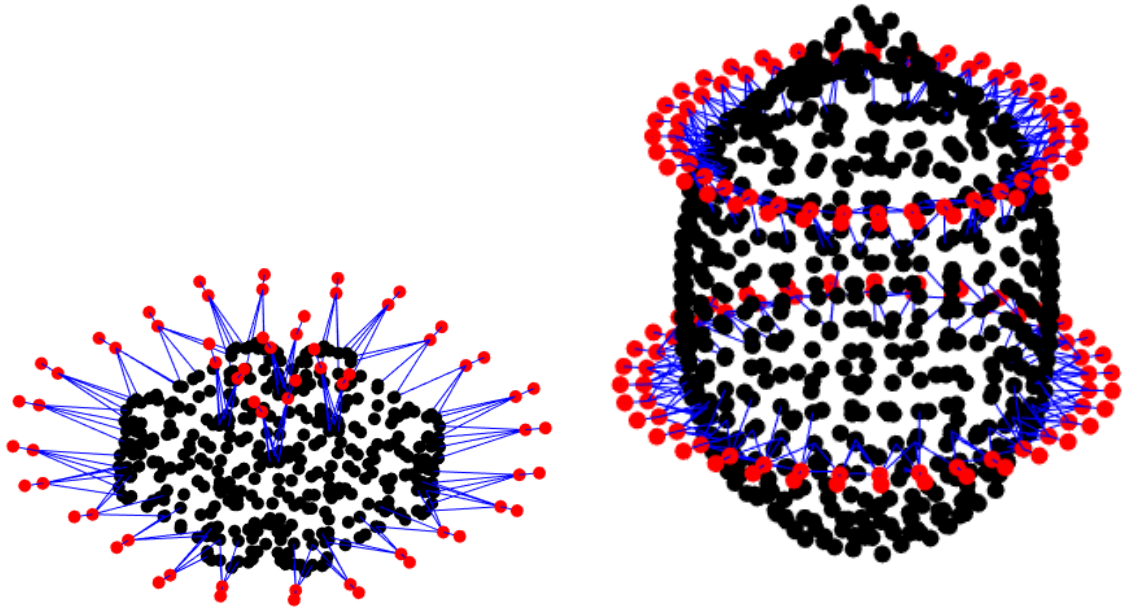
Chapter 3, we notice some interesting differences. The main difference that we find is that for our spherical multiciliate bead and spring swimmer we were unable to find an antiplectic wave as a stable steady state. This is fairly unexpected, as we found when studying the metachronal wave over the swimmer *Gonium* as well as for cilia in isolation with a prescribed beat that an antiplectic metachronal wave was able to give the fastest swimming speed or produce the largest amount of flux.

The antiplectic wave was also found to be a stable fixed point in our study of the bead and spring flagella around a circle, showing that a difference is caused by the presence and rotation of the body. The only stable steady state that we were able to find was a symplectic metachronal wave. This could help us understand why the symplectic metachronal wave is more commonly seen amongst multiciliate microswimmers and ciliary carpets.

5.4 Bead and Spring Models For Complex Shaped Microswimmers

Finally, we consider bead and spring models for some of our more complicated shaped swimmers that we studied earlier in Chapter 4. That is, the sixteen celled Volvocine green algae swimmer, *Gonium*, and the single celled multiciliate protozoan swimmer, *Didinium*. As when studying their swimming behaviour with a prescribed beat in Chapter 4, we model their bodies using the level set method as presented in Section 2.3.

We present our bead and spring models for these swimmers in Figure 5.9. Here we present the flagella related beads in red and the beads for the body in black. We have also omitted from the figure the springs for body that do not connect to any of the flagella related beads for clarity. For the full model, as with our bead and spring models of *Chlamydomonas* and the spherical multiciliate swimmer, each bead on the body would be attached to every other bead on the body via a spring. However, as part of this thesis, we were unable to produce results for these two models to present. This can be expanded on and these results obtained as further work to this thesis.



(a) Gonium (b) Didinium

Figure 5.9: We show our Bead and Spring model for *Gonium* in Panel (a) and *Didinium* in Panel (b). For clarity, the beads related to the body are in black and the beads relating to the flagella are in red. We also omit the springs in the figure that are not attached to any of the flagella related (red) beads to make the figure more clear.

5.5 Summary

In this chapter we expanded our Bead and spring model from Chapter 3 to model the interaction between flagella and their synchronisation as part of a full swimmer. We presented results for both *Chlamydomonas* and a simple example of a spherical multiciliate swimmer. As well as this we presented bead and spring models for the swimmers *Gonium* and *Didinium*, which we initially modelled with a prescribed beat in Chapter 4, for which results can be obtained as further work to this thesis.

For both of our bead and spring swimmers for which we obtained results, we found that the synchronous state was not a fully stable steady state of the system. The asynchronous state which we found to be stable is not often seen in swimming *Chlamydomonas* though was found to be occasionally present in a particular mutant studied by Leptos et al. (2013). For *Chlamydomonas*, this was the case both with the body and for the isolated flagella. We may be able to recover the synchronous case as stable for full bead and spring

flagella to further this work.

For our multiciliate swimmer, we found that there were some differences between this case and the equivalent isolated case of bead and spring flagella around a circle. The main difference being that only one stable fixed point was found for our multiciliate swimmer, which was very close to a symplectic metachronal wave with wave number 2, but not exact. More complex flagella using more beads may also potentially help find more stable fixed points for our multiciliate swimmer such as an antiplectic metachronal wave or an exact metachronal wave rather than close to it. It could also be useful to study our multiciliate swimmer with different numbers of flagella as well as a varying body size. In this Chapter we have studied the synchronisation of flagella over full swimmer models. We now go on to summarise the main results of our thesis and discuss any further work that could be done to extend the scope of this thesis.

CHAPTER 6

CONCLUSIONS AND OUTLOOK

6.1 Summary

The swimming of cells and microorganisms is a widely studied problem producing a large variety of interesting research. In this thesis, we have focused on modelling a particular aspect of microscopic swimming consisting of both multicellular and multiciliate microswimmers. These types of swimmers have not been studied very widely using models with accurate body shapes or fully resolved flagella. One reason for this is that the body of many of these swimmers have complicated geometry. Therefore, previous models often use shapes that are very simplified, such as modelling *Gonium* as a disk (de Maleprade et al., 2019), or have not been studied via Mathematical modelling in regards to their swimming behaviour such as with *Didinium*.

The transition to multicellularity is a widely studied problem within biology. The evolution of swimming behaviour as swimmers become more multicellular can be an interesting part of these studies. As part of this thesis, we wish to present this evolution of the swimming behaviour as the swimmers transition to multicellularity.

For multiciliate swimmers, we wish to understand how coordinated ciliary interaction can help to enhance swimming in microorganisms. We also look to study what the best and most optimal beat formations of flagella are to enhance swimming and if this is present for actual microswimmers in nature.

To solve these problems we first looked at the pumping of cilia over a plane. This was initially done for prescribed beat kinematics using full cilia models. We then looked to simplify our model by modelling the cilia as a single bead moving with both a circular beat and a more accurate beat. Comparing these results to that of the full cilia results, we find that they are qualitatively fairly similar. These similarities gave us the confidence to study a simple fluid structure interaction model for the cilia using a bead and spring model. This allowed us to look at the synchronisation and collective coordination of cilia over both a plane and a circle.

Following this, our next step was to focus on prescribed beat kinematics for complex swimmers and study their swimming behaviour. This was mostly focused on the Volvocine green algal colonies of various sizes as well as a study on the multiciliate protozoan, *Didinium*. Some of these swimmers have complex shaped bodies that are difficult to model. To overcome this problem, we utilised level sets to build the bodies of these swimmers using two different techniques.

The first level set method that we introduced focused on modelling swimmers with ellipsoidal cells such as *Gonium*. This allowed us to build the body of the swimmer by summing the functions of the level sets of Gaussians with each one representing a cell. We also displayed how we could use this method to model different levels of mucilage between the cells. Our other level set method looked at extruding a body out from a centre line. We then found the swimming behaviour for our swimmers utilising a nearest neighbour regularised Stokeslet method. We then packaged this model into the Algal Colony Suite. This is an app which we introduced to allow Biologists to build simple mathematical models to build multicellular swimmers with various potentially complex shaped bodies.

Finally we wished to combine our previous studies to produce a fluid structure interaction model for full multicellular and multiciliate swimmers. We again did this by utilising bead and spring models. This allowed us to study how multiple flagella interact and coordinate with each other to form various beat patterns such as metachronal waves. We could then compare this to what is observed in nature.

In the first part of Chapter 3, we studied the pumping of cilia over a plane with prescribed beat kinematics. In studying the metachronal wave as part of this, we found that the largest flux is typically produced for a slightly antiplectic metachronal wave. This effect on the metachronal wave is weakened as we increase the distance between the cilia. This would be expected since the hydrodynamic interactions between flagella decrease as they get further apart.

We also studied the effect of the angle of the cilia on the flux they produced. We vary the angle from $\alpha = 0$, where the cilia beat parallel to the direction of the metachronal wave, to $\alpha = \pi/2$, where the cilia beat perpendicular to the direction of the metachronal wave. We found an interesting result for $\alpha = \pi/2$. For all flagella beating synchronously, we expect that the flux produced perpendicular to the beat direction would be zero since there is no pumping in that direction which our results agree with. However, we found that when we introduce a metachronal wave in the flagella the flux in that direction is no longer zero. Since we still have no pumping effect in the direction of the metachronal wave, this flux is produced purely by the hydrodynamic interactions between the flagella.

Following this, in the second part of Chapter 3, we studied the interaction and coordination of the cilia using a bead and spring type model. In studying these bead and spring models, we found some unexpected results for the steady states of the system. That is that we were unable to find a metachronal wave with equal phase difference between all cilia when arranging the flagella in a line regardless of the initial state of the flagella. We instead find that the phase difference appears to spread out slightly, centred around the phase difference for two cilia.

We suspect that this is due to the imbalance of cilia either side of the neighbouring pair. Therefore, in this geometry to get a metachronal wave with equal phase difference between all neighbouring pairs of flagella we would require an infinite line of cilia. This would remove any effects of the end points of the line and imbalance of cilia due to the end points no longer being present. This is further implied when looking at twenty beads. Here we again see that the cilia spread around the two bead case. However, the cilia

appear to form into a travelling wave with increasing phase difference with the beads around the centre being very close to a full metachronal wave. This could be because as we increase the number of flagella, the imbalance becomes less pronounced before we get close to the end points of the line. This will likely get closer to a true metachronal wave as the number of cilia increases towards infinity.

To find a bead and spring system that had a stable steady state of a metachronal wave, we had to arrange the beads around a circle. This was then able to produce a true metachronal wave as a steady state. However, this was only very weakly stable if $\beta = 0$ such that the flagella were beating perpendicular to the direction of the metachronal wave. This was more strongly stable for other angles of orientation such as for $\beta = \pi/4$. The stable metachronal waves had integer wave numbers. However these differed slightly depending on if the flagella were over a boundary (modelled using Blakelets) or not. For the flagella beating without a boundary present we found that the stable metachronal wave had a wave number of ± 1. However this wave number was not stable over a boundary where a greater integer value wave number is required.

Following our studies on metachronal waves and the interaction between cilia, we went on to study the behaviour of various multicellular and multiciliate biological microswimmers. In particular focusing on the Volvocine green algae. In studying the Volvocine green algae, we were able compare the swimming behaviour of the different colonies as they increased in size. We were also able to compare the swimmers as they moved from disk shaped colonies to spherical colonies. In general, the spherical colonies were able to move much faster than the disk shaped colonies. This would be required of the larger swimmers due to them having a higher Peclet number. This higher Peclet number means that they rely more on advection to obtain nutrients to feed. We found that our results for swimming speeds were found to be quite accurate when compared to experimental values.

As in Chapter 3, we also study the effects of metachronal waves on the Volvocine swimmers. We again find similar results in that an antiplectic wave is able to produce the

largest swimming speed. For the swimmer *Gonium*, we also found that swimming with a metachronal wave was able to produce a helical trajectory for its swimming as is often seen in nature.

We further present the ability of our level set method in our model of *Didinium*. This is a swimmer for which little work has previously been done on its swimming due to its unusual and complex shape. Here we also find that a metachronal wave can result in a helical trajectory. We found that this was true for metachronal waves with odd integer wave numbers. However, the level of helicity was quite small as it was likely produced due to second order effects related to the metachronal wave.

Following this we wished to study the interaction between flagella and how they synchronise into different beats when part of an actual swimmer. Therefore we extended our bead and spring models of Chapter 3 to build a full bead and spring network to model a swimmer. We used this model to present results of a *Chlamydomonas* swimmer as well as a simple spherical swimmer with flagella placed around it. This allowed us to study the synchronisation of flagella around a sphere. We also presented the basis for models of *Didinium* and *Gonium* which we could study in this way.

The steady states for our bead and spring models were found to be similar for both separate flagella as well as when attached to the body of a swimmer with some small differences. For example the beating of *Chlamydomonas* flagella went to fully asynchronous as a steady state both when over a flat boundary and as part of the full swimmer model. The asynchronous beating is occasionally seen on beating *Chlamydomnas* such as during turning to steer or was occasionally seen to occur in the studying of a mutant form of *Chlamydomonas* (Leptos et al., 2013). However it is surprising that we are unable to obtain the synchronous beat as a stable steady state since this is the most common beat that we see for *Chlamydomonas* in nature. This could be potentially related to the lack of drag anisotropy effects in our bead and spring model. Therefore, for future work to extend this model we could consider full bead and spring flagella that take the the drag anisotropy into account and study the effects this has.

For our spherical multiciliate bead and spring swimmer, we found that it was much less similar to the equivalent separate flagella case of flagella around a circle. This was likely due to the rotation of the swimmer that was not present for the isolated bead and spring flagella around a circle. This rotation would also be a larger effect than the rocking of the body of *Chlamydomonas*, which could potentially be why we saw some change in our spherical multiciliate bead and spring swimmer and not in our bead and spring *Chlamydomonas* model, when compared to their isolated bead and spring flagella counterparts.

6.2 Further Work

We can further the work of thesis is multiple different ways. In our prescribed beat kinematics models in Chapter 3, we predominantly focused on the flux produced from a metachronal wave. However, when studying the coordination of cilia in a line using the bead and spring model, we found that this metachronal wave was not a stable steady state. It would be interesting to study the stable steady states that we did find, such as the steepening travelling wave for twenty cilia in a line, using prescribed beat kinematics. We would be able to study the flux that they produce and how it compares to our results for the flux produced by metachronal wave and the optimal metachronal wave. We can then discuss any differences there may be and why these might occur.

There are also multiple ways in which we can extend our work on the bead and spring model in the second part of Chapter 3. In our models, we found differing results for flagella dependant on if they were arranged in a line or a circle. We could further this work by considering other arrangements of flagella and studying how they interact with each other. One possible arrangement that may be worth studying with a bead and spring model would be the flagella arranged in a lattice formation. This would help more accurately represent some examples of large groups of cilia present in non-swimming examples or on swimmers such as paramecium.

For the cilia arranged in a line we can potentially further our study into this. For twenty beads arranged in a line we found that a travelling wave emerged. However this was not the case for only three beads. It would be interesting to study intermediate numbers of beads to find where and how this change towards a travelling wave takes place.

It may also be interesting to study the beating of flagella around an ellipse and compare how this differs to flagella positioned around a circle. We predict that these results could show behaviour somewhere in between those found around a circle and for a line depending on the aspect ratio of the ellipse. For an aspect ratio close to 1 we expect very little change from the results for a circle. However, as the ellipse becomes more elongated, we expect that the behaviour may be closer to that of a line for each elongated side of the ellipse. Though it would be interesting to study the hydrodynamic effect that would be had by cilia on one side of ellipse acting on the opposite side of the ellipse.

To further our work on our app, we can add more ways to allow for different types of swimmers to be modelled. The first of these to add to the app would be the level set method for extruding a body out from a centre line as used in our model for *Didinium* allowing a number of different swimmers to be built. The app could also be further expanded with different types of flagella such as a sperm tail or the helical flagella of bacteria. This would allow our app to become more all encompassing in the types of swimmers that it can produce models for. However, a downside is that this generalisation could potentially make the app more confusing to use due to the many additional options. Therefore, some thought would be required to keep the app simple to use.

Our study of the Volvocine green algae, that were modelled using the app that we created could also be looked into further. One example of how we could do this considers the differing level of mucilage between the cells. As part of our model of the Volvocine green algae, we studied how much of an effect this could have on their swimming behaviour. We found that this effect was very minimal. However, our model did not take into account different properties between the cells and the mucilage that may have some

effect on the swimming behaviour. This could be interesting to study as it would allow us to find how different structural properties, such as the amount of mucilage mucilage, can effect its swimming behaviour.

To further this study of the effect of the mucilage, we could find a way to take into account these different physical properties of the mucilage compared to the cell. One way of considering this could maybe be as part of the bead and spring swimmer models as discussed in Chapter 5 using differing spring stiffness over different parts of the swimmer to represent either cell or mucilage.

For the bead and spring swimmer models, the most obvious way in which we can further this is to study the swimming of a wider variety of swimmers. In Chapter 5, we present models for a bead and spring network for the swimmers *Gonium* and *Didinium*. However we were not yet able to obtain results for these. This was because of the complexity and size of models means that they would take too long to run to complete as part of this thesis. Therefore, some initial further work would be to obtain results for these models. Another swimmer that could be interesting to study using our bead and spring models would be *Paramecium*. This would give us an interesting look at the synchronisation of a ciliary carpet when on a swimmer. However, with our current model, this would likely be too large and complex a model to be able to run in a reasonable time. Also due to the proximity that would be required of flagella, there may be some issues with beads getting too close to each other and crossing which could cause problems. Therefore to do this we would need to find a way around these issues.

It may also be useful to extend our study of the spherical multiciliate bead and spring model. One aspect to look further into is the flagella. We could study the effect of different numbers of flagella as well as considering the flagella with different orientations. This could then be related to our study on the effect of the orientation angle for our bead and spring model of isolated flagella around a circle.

We could also study the body of our multiciliate swimmer. For example, we could look at how different shapes and sizes of the body affect how the flagella of the swimmer

synchronise. For this, we could study the effect of different radii of the sphere. As well as this, we could consider the swimmer with an ellipsoidal body testing the effects of different semi-axes of the swimmers body. We could then potentially relate this to our results for some of the Volvocine green algae such as *Pandorina* or *Eudorina* which are occasionally found to be slightly ellipsoidal.

Another way to further our work on the bead and spring model, both as part of swimmers and for separate cilia, would be to improve the model which we use. One method for this would be to consider a more accurate bead and spring representation of the flagella. One way we could do this is by modelling the flagella as a single bead with a more accurate trajectory. This would give a more accurate representation while keeping the model quite simple. However, this would still not take into account the drag anisotropy effect. To further improve our model and incorporate the drag anisotropy we would have to model the flagella with multiple beads.

To do this we would need to place beads across the length of a flagellum. We would then need to find the driving force required at each beat to actively bend the flagellum to create an accurate flagellar beat. One potential way to find this force could be to consider the model of a flagellum with a prescribed beat. We could solve to find the forces that produce this beat along the flagellum. We can then try and fit this to a function which we could then potentially use as our driving force.

An important consideration in improving the beat is to take into account the beat regulation and curvature control of the flagella. To beat the flagellum actively bends over the whole filament. How this bend occurs and evolves is affected by the local curvature of flagellum (Gallagher et al., 2022). As the filament bends, the dynein arms that push the microtubules to cause the beating are able to push more effectively. This is then able to control the beat. It may be useful to incorporate this beat regulation and idea of curvature control into our bead and spring model to produce more realistic beating flagella. For this we could have the driving force acting on the beads relate to the local curvature of flagellum at the points of the beads.

Many of the major results of this thesis focus on metachronal waves. That is studying optimal metachronal waves as well as how these waves are formed. These results could potentially produce some interest for further work. For example, models of metachronal waves that are used in this thesis could potentially be utilised and expanded for modelling metachronal waves within airways. This could potentially help in clinical situations in studying issues where there is something wrong with the coordination of the cilia. Our development of the Algal Colony Suite along with the level set method for building swimmers could also aid biologists in being able to study and understand basic swimming behaviour for many microswimmers that would otherwise be difficult to produce a model of allowing for a greater understanding.

LIST OF REFERENCES

Ainley, J., Durkin, S., Embid, R., Boindala, P., and Cortez, R. (2008). The method of images for regularized stokeslets. *Journal of Computational Physics*, 227(9):4600 – 4616.

Antipa, G. (1968). Didinium nasutum, cell by organism, eukaryotic cell, eukaryotic protist, ciliated protist. cil. dataset. CIL:39251.

Arakaki, Y., Kawai-Toyooka, H., Hamamura, Y., Higashiyama, T., Noga, A., Hirono, M., Olson, B. J. S. C., and Nozaki, H. (2013). The simplest integrated multicellular organism unveiled. *PLOS ONE*, 8(12):1–8.

Arrieta, J., Barreira, A., Chioccioli, M., Polin, M., and Tuval, I. (2017). Phototaxis beyond turning: persistent accumulation and response acclimation of the microalga chlamydomonas reinhardtii. *Scientific Reports*, 7.

Batchelor, G. K. (1970). Slender-body theory for particles of arbitrary cross-section in stokes flow. *Journal of Fluid Mechanics*, 44(3):419–440.

Batchelor, G. K. (2000). *An Introduction to Fluid Dynamics*. Cambridge Mathematical Library. Cambridge University Press.

Berg, H. C. and Brown, D. A. (1972). Chemotaxis in escherichia coli analyzed by three-dimensional tracking. *Nature*, 239:500–4.

Blake, J. R. (1971a). A note on the image system for a stokeslet in a no-slip boundary. *Mathematical Proceedings of the Cambridge Philosophical Society*, 70(2):303–310.

Blake, J. R. (1971b). A spherical envelope approach to ciliary propulsion. *Journal of Fluid Mechanics*, 46(1):199–208.

Brumley, D. R., Polin, M., Pedley, T. J., and Goldstein, R. E. (2015). Metachronal waves in the flagellar beating of ¡i¿volvox¡/i¿ and their hydrodynamic origin. *Journal of The Royal Society Interface*, 12(108):20141358.

Bustamante-Marin, X. M. and Ostrowski, L. E. (2017). Cilia and mucociliary clearance. *Cold Spring Harbor perspectives in biology*, 9.

Chen, X., Zeng, L., Wu, Y., Gao, Y., and Zhao, Y. (2017). Swimming characteristics of gyrotactic microorganisms in low-reynolds-number flow: Chlamydomonas reinhardtii. *Energy, Ecology and Environment*, 2.

Clarke, N. S. (1972). The force distribution on a slender twisted particle in a stokes flow. *Journal of Fluid Mechanics*, 52(4):781–793.

Coleman, A. W. (2012). A comparative analysis of the volvocaceae (chlorophyta). *Journal of Phycology*, 48(3):491–513.

Cortez, R. (2001). The method of regularized stokeslets. *SIAM J. Sci. Comput.*, 23(4):1204–1225.

Cortez, R. (2018). Regularized stokeslet segments. *Journal of Computational Physics*, 375:783 – 796.

Cortez, R., Fauci, L., and Medovikov, A. (2005). The method of regularized stokeslets in three dimensions: Analysis, validation, and application to helical swimming. *Physics of Fluids*, 17.

Dasgupta, A. and Amack, J. D. (2016). Cilia in vertebrate left–right patterning. *Philosophical Transactions of the Royal Society B: Biological Sciences*, 371(1710):20150410.

Dauparas, J. and Lauga, E. (2018). Leading-order stokes flows near a corner. *IMA Journal of Applied Mathematics*, 83(4):590–633.

de Maleprade, H., Moisy, F., Ishikawa, T., and Goldstein, R. E. (2019). Motility and phototaxis of gonium, the simplest differentiated colonial alga. *bioRxiv*.

Du, J., Keener, J. P., Guy, R. D., and Fogelson, A. L. (2012). Low-reynolds-number swimming in viscous two-phase fluids. *Phys. Rev. E*, 85:036304.

Dunkel, J., Heidenreich, S., Drescher, K., Wensink, R., Bär, M., and Goldstein, R. (2013). Fluid dynamics of bacterial turbulence. *Physical review letters*, 110:228102.

Elgeti, J. and Gompper, G. (2013). Emergence of metachronal waves in cilia arrays. *Proceedings of the National Academy of Sciences*, 110(12):4470–4475.

Fulford, G. and Blake, J. (1983). Slender body theory in mucociliary transport.

Gallagher, M. T., Kirkman-Brown, J. C., and Smith, D. J. (2022). Axonemal regulation by curvature explains sperm flagellar waveform modulation.

Gallagher, M. T. and Smith, D. J. (2018). Meshfree and efficient modeling of swimming cells. *Phys. Rev. Fluids*, 3:053101.

Gillies, E. A., Cannon, R. M., Green, R. B., and Pacey, A. A. (2009). Hydrodynamic propulsion of human sperm. *Journal of Fluid Mechanics*, 625:445–474.

Goldstein, R. E. (2015). Green algae as model organisms for biological fluid dynamics. *Annual Review of Fluid Mechanics*, 47(1):343–375.

Gray, J. and Hancock, G. J. (1955). The propulsion of sea-urchin spermatozoa. *Journal of Experimental Biology*, 32(4):802–814.

Gueron, S. and Levit-Gurevich, K. (2001). A three-dimensional model for ciliary motion based on the internal 9 + 2 structure. *Proceedings of the Royal Society of London. Series B: Biological Sciences*, 268(1467):599–607.

Gueron, S., Levit-Gurevich, K., Liron, N., and Blum, J. J. (1997). Cilia internal mechanism and metachronal coordination as the result of hydrodynamical coupling. *Proceedings of the National Academy of Sciences of the United States of America*.

Hancock, G. J. (1953). The self-propulsion of microscopic organisms through liquids. *Proceedings of the Royal Society of London. Series A. Mathematical and Physical Sciences*, 217(1128):96–121.

Hansen, C. H., Endres, R. G., and Wingreen, N. S. (2008). Chemotaxis in escherichia coli: A molecular model for robust precise adaptation. *PLOS Computational Biology*, 4(1):1–1.

Harrison, G. W. (1995). Comparing predator-prey models to luckinbill's experiment with didinium and paramecium. *Ecology*, 76(2):357–374.

Hewitt, D. R. and Balmforth, N. J. (2017). Taylor's swimming sheet in a yield-stress fluid. *Journal of Fluid Mechanics*, 828:33–56.

Higdon, J. J. L. (1979). The hydrodynamics of flagellar propulsion: helical waves. *Journal of Fluid Mechanics*, 94(2):331–351.

Höhn, S. and Hallmann, A. (2016). Distinct shape-shifting regimes of bowl-shaped cell sheets – embryonic inversion in the multicellular green alga pleodorina. *BMC Developmental Biology*, 16.

Ishimoto, K. and Gaffney, E. A. (2013). Squirmer dynamics near a boundary. *Phys. Rev. E*, 88:062702.

Ishimoto, K. and Gaffney, E. A. (2018). Hydrodynamic clustering of human sperm in viscoelastic fluids. *Scientific Reports*, 8.

Jing, J. C., Chen, J. J., Chou, L., Wong, B. J. F., and Chen, Z. (2017). Visualization and detection of ciliary beating pattern and frequency in the upper airway using phase resolved doppler optical coherence tomography. *Scientific Reports*, 7.

Johnson, R. and J Brokaw, C. (1979). Flagellar hydrodynamics. a comparison between resistive-force theory and slender-body theory. *Biophysical journal*, 25:113–27.

Keaveny, E. E. and Brown, A. E. X. (2017). Predicting path from undulations for c. elegans using linear and nonlinear resistive force theory. *Physical Biology*, 14.

Kinosita, Y., Uchida, N., Nakane, D., and Nishizaka, T. (2016). Direct observation of rotation and steps of the archaellum in the swimming halophilic archaeon halobacterium salinarum. *Nature Microbiology*, 1.

Kirkman-Brown, J. C. and Smith, D. J. (2011). Sperm motility: is viscosity fundamental to progress? *Molecular Human Reproduction*, 17(8):539–544.

Koens, L. and Lauga, E. (2018). The boundary integral formulation of stokes flows includes slender-body theory. *Journal of Fluid Mechanics*, 850:R1.

Kong, M., Wu, Y., Li, G., and Larson, R. G. (2015). A bead-spring model for running and tumbling of flagellated swimmers: detailed predictions compared to experimental data for e. coli. *Soft Matter*, 11:1572–1581.

Lauga, E. and Eloy, C. (2013). Shape of optimal active flagella. *Journal of Fluid Mechanics*, 730:R1.

Lauga, E. and Goldstein, R. (2012). Dance of the microswimmers. *Physics Today*, 65:30–.

Lauga, E. and Powers, T. R. (2009). The hydrodynamics of swimming microorganisms. *Reports on Progress in Physics*, 72(9):096601.

Leeuwenhoek, A. V. (1677). Observations, communicated to the publisher by mr. antony van leewenhoeck, in a dutch letter of the 9th octob. 1676. here english'd: concerning little animals by him observed in rain-well-sea- and snow water; as also in water wherein pepper had lain infused. *Philosophical Transactions of the Royal Society of London*, 12(133):821–831.

Leptos, K. C., Chioccioli, M., Furlan, S., Pesci, A. I., and Goldstein, R. E. (2018). An adaptive flagellar photoresponse determines the dynamics of accurate phototactic steering in chlamydomonas. *eLife*.

Leptos, K. C., Wan, K. Y., Polin, M., Tuval, I., Pesci, A. I., and Goldstein, R. E. (2013). Antiphase synchronization in a flagellar-dominance mutant of chlamydomonas. *Phys. Rev. Lett.*, 111:158101.

Lighthill, J. (1976). Flagellar hydrodynamics. *SIAM Review*, 18(2):161–230.

Lighthill, M. J. (1952). On the squirming motion of nearly spherical deformable bodies through liquids at very small reynolds numbers. *Communications on Pure and Applied Mathematics*, 5(2):109–118.

Liron, N. and Mochon, S. (1976). Stokes flow for a stokeslet between two parallel flat plates. *Journal of Engineering Mathematics*, 10:287–303.

Liron, N. and Shahar, R. (1978). Stokes flow due to a stokeslet in a pipe. *Journal of Fluid Mechanics*, 86(4):727–744.

Llopis, I. and Pagonabarraga, I. (2010). Hydrodynamic interactions in squirmer motion: Swimming with a neighbour and close to a wall. *Journal of Non-Newtonian Fluid Mechanics*, 165(17):946 – 952. Proceedings of the 5th International Workshop on Non-Equilibrium Thermodynamics IWNET 2009.

Luckinbill, L. S. (1973). Coexistence in laboratory populations of paramecium aurelia and its predator didinium nasutum. *Ecology*, 54(6):1320–1327.

Machemer, H. (1972). Ciliary Activity and the Origin of Metachrony in Paramecium: Effects of Increased Viscosity. *Journal of Experimental Biology*, 57(1):239–259.

Milana, E., Zhang, R., Vetrano, M. R., Peerlinck, S., De Volder, M., Onck, P. R., Reynaerts, D., and Gorissen, B. (2020). Metachronal patterns in artificial cilia for low reynolds number fluid propulsion. *Science Advances*, 6(49).

Montenegro-Johnson, T., Michelin, S., and Lauga, E. (2015). A regularised singularity approach to phoretic problems. *The European Physical Journal E*, 38.

Montenegro-Johnson, T. D. (2013). *Microscopic Swimming in Biological Fluids*. PhD thesis, University of Birmingham.

Montenegro-Johnson, T. D. and Lauga, E. (2014). Optimal swimming of a sheet. *Phys. Rev. E*, 89:060701.

Montenegro-Johnson, T. D., Smith, A. A., Smith, D. J., Loghin, D., and Blake, J. R. (2012). Modelling the fluid mechanics of cilia and flagella in reproduction and development. *The European Physical Journal E*, 35.

Montino, A. and DeSimone, A. (2015). Three-sphere low-reynolds-number swimmer with a passive elastic arm. *The European Physical Journal E*, 38.

Mukherjee, S. and Kearns, D. B. (2014). The structure and regulation of flagella in bacillus subtilis. *Annual review of genetics*, 48.

Najafi, A. and Golestanian, R. (2004). Simple swimmer at low reynolds number: Three linked spheres. *Phys. Rev. E*, 69:062901.

Nakamura, S. and Minamino, T. (2019). Flagella-driven motility of bacteria. *Biomolecules*, 9(7):279.

Nelson, B. J., Kaliakatsos, I. K., and Abbott, J. J. (2010). Microrobots for minimally invasive medicine. *Annual Review of Biomedical Engineering*, 12(1):55–85. PMID: 20415589.

Niedermayer, T., Eckhardt, B., and Lenz, P. (2008). Synchronization, phase locking, and metachronal wave formation in ciliary chains. *Chaos: An Interdisciplinary Journal of Nonlinear Science*, 18(3):037128.

O'Malley, S. and Bees, M. A. (2012). The orientation of swimming biflagellates in shear flows. *Bulletin of Mathematical Biology*, 74.

Omori, T. and Ishikawa, T. (2019). Swimming of spermatozoa in a maxwell fluid. *Micromachines*, 10.

Osterman, N. and Vilfan, A. (2011). Finding the ciliary beating pattern with optimal efficiency. *Proceedings of the National Academy of Sciences*, 108(38):15727–15732.

Pande, J., Merchant, L., Harting, J., and Smith, A.-S. (2014). When micro-swimmers get a spring in their stroke. *arXiv*, (arXiv:1411.5723 [cond-mat.soft]):1–4.

Pande, J. and Smith, A.-S. (2013). Optimal shapes of artificial bead-spring micro-carriers at low reynolds numbers.

Pedley, T. J., Brumley, D. R., and Goldstein, R. E. (2016). Squirmers with swirl: a model for volvox swimming. *Journal of Fluid Mechanics*.

Pernberg, J. and Machemer, H. (1995). Voltage-dependence of ciliary activity in the ciliate Didinium nasutum. *Journal of Experimental Biology*, 198(12):2537–2545.

Phan-Thien, N., Tran-Cong, T., and Ramia, M. (1987). A boundary-element analysis of flagellar propulsion. *Journal of Fluid Mechanics*, 184:533–549.

Pickl, K., Pande, J., Köstler, H., Rüde, U., and Smith, A.-S. (2017). Lattice boltzmann simulations of the bead-spring microswimmer with a responsive stroke—from an individual to swarms. *Journal of Physics: Condensed Matter*, 29(12):124001.

Ping, L., Birkenbeil, J., and Monajembashi, S. (2013). Swimming behavior of the monotrichous bacterium Pseudomonas fluorescens SBW25. *FEMS Microbiology Ecology*, 86(1):36–44.

Polin, M., Tuval, I., Drescher, K., Gollub, J. P., and Goldstein, R. E. (2009). Chlamydomonas swims with two gears in a eukaryotic version of run-and-tumble locomotion. *Science*, 325(5939):487–490.

Pozrikidis, C. (1992). *Boundary Integral and Singularity Methods for Linearized Viscous Flow*. Cambridge Texts in Applied Mathematics. Cambridge University Press.

Purcell, E. M. (1976). Life at low reynolds number. *American Journal of Physics*.

Ramirez-San Juan, G. R., Mathijssen, A. J. T. M., He, M., Jan, L., Marshall, W., and Prakash, M. (2020). Multi-scale spatial heterogeneity enhances particle clearance in airway ciliary arrays. *Nature Physics*, 16.

Reynolds, O. (1883). An experimental investigation of the circumstances which determine whether the motion of water shall be direct or sinuous, and of the law of resistance in parallel channels. *Royal Society*, 35.

Riley, E. E. and Lauga, E. (2014). Enhanced active swimming in viscoelastic fluids. *Europhysics Letters*, 108(3):34003.

Riley, E. E. and Lauga, E. (2017). Empirical resistive-force theory for slender biological filaments in shear-thinning fluids. *Phys. Rev. E*, 95:062416.

Rode, S., Elgeti, J., and Gompper, G. (2021). Multi-ciliated microswimmers–metachronal coordination and helical swimming. *The European Physical Journal E*, 44.

Rothschild (1963). Non-random distribution of bull spermatozoa in a drop of sperm suspension. *Nature*, 198.

Sauzade, M., Elfring, G. J., and Lauga, E. (2011). Taylor's swimming sheet: Analysis and improvement of the perturbation series. *Physica D: Nonlinear Phenomena*, 240(20):1567 – 1573. Special Issue: Fluid Dynamics: From Theory to Experiment.

Schuhmacher, J. S., Thormann, K. M., and Bange, G. (2015). How bacteria maintain location and number of flagella? *FEMS Microbiology Reviews*, 39(6):812–822.

Small, E. B., Marszalek, D. S., and Antipa, G. A. (1971). A survey of ciliate surface patterns and organelles as revealed with scanning electron microscopy. *Transactions of the American Microscopical Society*, 90(3):283–294.

Smith, D. J. (2009). A boundary element regularized stokeslet method applied to cilia- and flagella-driven flow. *Proceedings of the Royal Society A: Mathematical, Physical and Engineering Sciences*, 465(2112):3605–3626.

Smith, D. J. (2018). A nearest-neighbour discretisation of the regularized stokeslet boundary integral equation. *Journal of Computational Physics*, 358:88 – 102.

Smith, D. J., Gaffney, E. A., Blake, J. R., and Kirkman-Brown, J. C. (2009). Human sperm accumulation near surfaces: a simulation study. *Journal of Fluid Mechanics*, 621:289–320.

Solari, C., Drescher, K., and Goldstein, R. (2011). The flagellar photoresponse in volvox species (volvocaceae, chlorophyceae). *Journal of Phycology*, 47:580 – 583.

Solari, C., O. Kessler, J., and Goldstein, R. (2007). Motility, mixing, and multicellularity. *Genetic Programming and Evolvable Machines*, 8:115–129.

Solari, C. A., Kessler, J. O., and Michod, R. E. (2006). A hydrodynamics approach to the evolution of multicellularity: Flagellar motility and germ-soma differentiation in volvocalean green algae. *The American Naturalist*, 167(4):537–554. PMID: 16670996.

Stocker, R. and Durham, W. M. (2009). Tumbling for stealth? *Science*, 325(5939):400–402.

Szathmáry, E. and Maynard Smith, J. (1995). The major evolutionary transitions. *Nature*, 374:227–32.

Tabak, A. F. and Yesilyurt, S. (2010). Validated Reduced Order Models for Simulating Trajectories of Bio-Inspired Artificial Micro-Swimmers. ASME 2010 8th International Conference on Nanochannels, Microchannels, and Minichannels: Parts A and B:57–63.

Tamm, S. L. and Horridge, G. A. (1970). The relation between the orientation of the central fibrils and the direction of beat in cilia of opalina. *Proceedings of the Royal Society of London. Series B, Biological Sciences*, 175(1040):219–233.

Taylor, G. (1951). Analysis of the swimming of microscopic organisms. *Proceedings of The Royal Society A: Mathematical, Physical and Engineering Sciences*, 209:447–461.

Taylor, G. (1967). Film notes for low-reynolds number flows. *National Comittee for Fluid Mechanics*.

Velho Rodrigues, M. F., Lisicki, M., and Lauga, E. (2021). The bank of swimming organisms at the micron scale (boso-micro). *PLOS ONE*, 16(6):1–80.

Velicer, G. and Yu, Y.-T. N. (2003). Evolution of novel cooperative swarming in the bacterium myxococcus xanthus. *Nature*, 425:75–8.

Vellai, T. and Vida, G. (1999). The origin of eukaryotes: the difference between prokaryotic and eukaryotic cells. *Proceedings of the Royal Society of London. Series B: Biological Sciences*, 266(1428):1571–1577.

Youngren, G. K. and Acrivos, A. (1975). Stokes flow past a particle of arbitrary shape: a numerical method of solution. *Journal of Fluid Mechanics*, 69(2):377–403.

Zhao, B., Lauga, E., and Koens, L. (2019). Method of regularized stokeslets: Flow analysis and improvement of convergence. *Phys. Rev. Fluids*, 4:084104.

Zick, A. A. and Homsy, G. M. (1982). Stokes flow through periodic arrays of spheres. *Journal of Fluid Mechanics*, 115:13–26.